LANGLEY GRANT
IN-18-CR
102,711
152-P.

NASA Grant NAG 1 - 541

FINAL REPORT

VIBRATIONS AND STRUCTUREBORNE NOISE IN SPACE STATION

R. Vaicaitis, C.S. Lyrintzis and D.A. Bofilios

Department of Civil Engineering and Engineering Mechanics
Institute of Flight Structures
Columbia University
New York, NY 10027

October 9, 1987

(NASA-CR-181381) VIBRATIONS AND STRUCTUREBORNE NOISE IN SPACE STATION Final Report (Columbia Univ.) 152 p Avail: NTIS HC A08/MF A01 CSCL 22B
N87-29590
Unclas
G3/18 0102711

TABLE OF CONTENTS

SECTION PAGE

FOREWORD

This study was performed for NASA Langley Research Center, ANRD by the Department of Civil Engineering and Engineering Mechanics, Institute of Flight Structures, Columbia University under Grant NAG1-541. The NASA Langley technical monitor was Dr. A.C. Powell.

1.0 SUMMARY

Analytical models have been developed to predict vibrations and structureborne noise generation of cylindrical and rectangular acoustic enclosures. These models are then used to determine structural vibration levels and interior noise to random point input forces. The guidelines developed in this study could provide preliminary information on acoustical and vibrational environments in space station habitability modules under orbital operations. The structural models include single wall monocoque shell, double wall shell, stiffened orthotropic shell, descretely stiffened flat panels, and a coupled system composed of a cantilever beam structure and a stiffened sidewall. Aluminum and fiber reinforced composite materials are considered for single and double wall shells. The end caps of the cylindrical enclosures are modeled either as single or double wall circular plates. Sound generation in the interior space is calculated by coupling the structural vibrations to the acoustic field in the enclosure. Modal methods and transfer matrix techniques are used to obtain structural vibrations. Parametric studies are performed to determine the sensitivity of interior noise environment to changes in input, geometric and structural conditions.

2.0 INTRODUCTION

Structural vibrations and noise could play a significant role on the quality of physical environment in space station for prolonged orbital operations. Even though it is not expected that noise will be a major risk factor for physical health, it could be a significant source of annoyance, speech interference and fatique to individuals working under these conditions [1]. Furthermore, excessive vibrations and noise could have an adverse effect on delicate scientific experiments and manufacturing processes that are being proposed under zero gravity conditions [2]. To satisfy the various proposed design objectives, the manned space station will need to perform many mission support functions such as pressurized and unpressurized laboratories, base for attached payloads, communications, command and control support, assembly, deployment and construction, maintenance, servicing, life support systems, etc. Mechanical vibrations resulting from power supply units, life support systems, electrical equipment, control thruster action, etc., could induce unwanted vibrations and noise. The information that is presently available on vibro-acoustic environment for space station operations is very limited. The experience from Skylab [3-7] and other sources [1,2] could serve as a starting point of identifying some of the potential vibration and noise problems in the space station. The structureborne noise induced by mechanical vibrations could be a significant contributor to the noise environment inside the habitability modules. A detailed account of structureborne noise related work was presented in a review article [8]. In general, the generation and transmission of structureborne noise are not well understood and fundamental theoretical and experimental work is needed.

This report presents an analytical study on vibration response and noise generation in cylindrical shells and rectangular enclosures due to mechanical random point loads. The geometry of these structures are taken to be representative of pressurized habitability modules of the space station design. The end caps of the cylindrical shell are modeled as circular plates. Single wall, double wall and stiffened (frames and stringers) shells are taken as different options of the structural model. For the double wall construction the exterior shell could serve as a radiation and/or thermal shield while the interior shell is the main load carrying structure. The space between the two thin shells is assumed to be filled with soft thermal insulating materials. For the low frequency range considered in this study, the stiffened shell is represented by an equivalent orthotropic shell wherein the effect of frames and stringers is smeared into an equivalent skin [9,10]. The rectangular acoustic enclosure model is used to approximate the interior space of the habitability modules and to study structureborne noise generation by vibration of small panels, partitions, stiffened panels and complex structural geometries involving stiffened beams and discretely stiffened panels. The space station artist's concept and a typical habitability module are shown in Figs. 1 and 2. The structural models considered in the present study are presented in Figs. 3-7. The loads are random point forces which can be acting at any arbitrary location on the shell, end plates, panels, stiffeners or the sub-structure as shown in Figs. 6 and 7.

The shell skins are modeled according to thin shell theory [11-16] and the end plates using the theory of thin circular plates [17-24]. For the case of fiber reinforced composite materials, the equations of motion are developed for the cases where a shell is a composite buildup of laminae, which consists of fibers imbedded in a supporting matrix [25-30]. The solution for shell and end plate vibrations are developed utilizing a modal approach [31,32]. Similarly, the acoustic wave equation for the generated interior acoustic pressure due to shell and/or end plate vibrations is solved by the Galerkin-like procedure. Hard walls and absorbent boundary conditions at the interior surface are considered. To determine vibration response and noise transmission for the interconnected structures shown in Fig. 7, a modified transfer matrix procedure was developed [33-35]. In this approach, arbitrary point loads and/or distributed loads can be acting on the structure (beam) and the main structure (stiffened sidewall). Due to the complexity of the load transfer paths of these built-up structures, it is not easy to construct models which couple the various sub-components into a single dynamic system. The transfer matrix method proved to be relatively straightforward to apply to these stiffened structures. However, procedures based on transfer matrices suffer some drawbacks in practice. Because of the successive matrix multiplication required in this approach, ill-conditioned systems are produced which require high precision to obtain meaningful results. To circumvent these difficulties, several different methods have been used. These include the modified transfer matrix method [36], delta matrix formulation [37,38], precalculation of products using symbolic manipulation algorithms [39], double and quadruple precision, and special purpose routines for manipulating large numbers.

3.0 ANALYTICAL MODELS

3.1 Noise Generation Inside a Cylindrical Enclosure

Consider a closed cylindrical enclosure with interior volume $V = \pi R^2 L$ as shown in Figs. 3-6. The noise inside this enclosure is generated by the vibrations of the shell structure and/or the vibrations of the circular end plates. Assume the shell and the end plate motions are independent. The solutions for shell and plate vibrations due to random point loads are presented in Sec. 3.3 - 3.5. The acoustic pressure inside the cylindrical enclosure can be obtained from

$$p = p_1 + p_2 \tag{1}$$

where p_1 and p_2 are the acoustic pressures generated by the shell and end plate motions. The pressure p satisfies the linearized acoustic wave equation

$$\nabla^2 p - \beta \dot{p} = \ddot{p}/c^2 \tag{2}$$

in which β and c are the acoustic damping and speed of sound inside the enclosure, a dot indicates time derivative, and

$$\nabla^2 = \partial^2/\partial r^2 + (1/r)\partial/\partial r + (1/r^2)\, \partial^2/\partial \theta^2 + \partial^2/\partial x^2 \tag{3}$$

The boundary conditions to be satisfied are

$$\partial p_1/\partial r = -\rho \ddot{w} - (\rho/Z)\dot{p}_1 \qquad \text{at } r=R \qquad (4)$$

$$\partial p_1/\partial x = 0 \qquad \text{at } x = 0,L \qquad (5)$$

$$\partial p_2/\partial x = \rho \ddot{w}_L + (\rho/Z_L)\,\dot{p}_2 \qquad \text{at } x = 0 \qquad (6)$$

$$\partial p_2/\partial x = -\rho \ddot{w}_R - (\rho/Z_R)\,\dot{p}_2 \qquad \text{at } x = L \qquad (7)$$

$$\partial p_2/\partial r = 0 \qquad \text{at } r = R \qquad (8)$$

where ρ is air density, w, w_L, w_R are the displacements in the normal direction (positive outwards) of the shell, left end plate and right end plate, Z, Z_L, and Z_R are the absorbent wall impedances at the surfaces of the shell, left end plate and right end plate, respectively. In the present study, it was assumed that all interior walls are treated uniformly with insulating materials for which [40]

$$Z = Z_L = Z_R = -\rho c\ \{(1 + 0.0571\ (2\pi R_1/\rho\omega)^{0.754}) \qquad (9)$$

$$+ \underset{\sim}{i}\ (0.087\ (2\pi R_1/\rho\omega)^{0.732})\}$$

where R_1 is the flow resistivity of porous acoustic material, ω is radial frequency and $\underset{\sim}{i} = \sqrt{-1}$. The acoustic damping in the interior is modeled as

$$\beta = 2\zeta_0\omega^1 / c^2 \tag{10}$$

where ω^1 is the lowest acoustic modal frequency and ζ_o is the damping coefficient corresponding to the first acoustic modal frequency in the cylindrical enclosure.

The solution to Eqs. 2-8 can be written in frequency domain in terms of the orthongonal acoustic modes corresponding to acoustically hard walls as

$$\bar{p}_1 (x,r,\theta,\omega) = \sum_{i=0}^{\infty} \sum_{j=0}^{\infty} P_{ij}(r,\omega)\, X_{ij}(x,\theta) \tag{11}$$

$$\bar{p}_2(x,r,\theta,\omega) = \sum_{j=0}^{\infty} \sum_{k=1}^{\infty} Q_{jk}(x,\omega) Y_{jk}(r,\theta) \tag{12}$$

where the acoustic modes for a closed cylindrical enclosure are

$$X_{ij} = (2/\pi L)^{1/2} \cos(i\pi x/L)\, \cos(j\theta) \tag{13}$$

$$Y_{jk} = J_j(\lambda_{jk} r)\, \cos(j\theta) \tag{14}$$

where J_j is the Bessel function of the first kind of order j, $\lambda_{jk} = \alpha_{jk}/R$ where α_{jk} is the kth root of the equation $dJ_j/dr = 0$. Substituting Eqs. 11 and 12 into Eqs. 2-8 and using orthogonality condition of acoustic modes gives a set of ordinary differential equations which can be solved for the generalized coordinates P_{ij} and Q_{jk}. A detailed procedure of this approach is given in Refs. 31, 41,42. Then, the spectral density of the acoustic pressure p can be determined from

$$S_p(x,r,\theta,\omega) = S_{p_1}(x,r,\theta,\omega) + S_{p_2}(x,r,\theta,\omega) \tag{15}$$

where S_{p_1} and S_{p_2} are spectral densities corresponding to acoustic pressures p_1 and p_2. The sound pressure inside the enclosure is calculated from

$$SPL(x,r,\theta,\omega) = 10 \log \{S_p(x,r,\theta,\omega)\Delta\omega/p_0^2\} \tag{16}$$

where p_0 is the reference pressure ($p_0 = 2.9 \times 10^{-9}$ psi $= 20\ \mu N/m^2$) .

3.2 Noise Generation Inside a Rectangular Enclosure

Consider a rectangular acoustic space occupying a volume V = abd as shown in Fig. 7. Noise is generated in the acoustic enclosure through vibrations of the flexible portions of the sidewalls, partitions, or individual small panels which can be located at any arbitrary position on the structure. The perturbation pressure p within the enclosure satisfies Eq. 2 where now

$$\nabla^2 = \partial^2/\partial x^2 + \partial^2/\partial y^2 + \partial^2/\partial z^2 \tag{16}$$

The types of boundary conditions to be satisfied by Eq. 2 depend on the interior surface conditions of the walls. These could range from acoustically hard walls to those of highly absorbent walls which are treated with acoustic insulation materials. At acoustically rigid boundaries,

$$\partial p/\partial n = 0 \tag{17}$$

where n is outward normal to the boundary. Equation 2 together with Eq. 17 can be used to calculate modes and modal frequencies in the enclosure. For a surface treated with acoustic absorbent materials, the boundary conditions can be represented by

$$\partial p/\partial n = -\rho\dot{p}/Z \tag{18}$$

where Z is the point impedance defined in Eq. 9. For a flexible elastic surface treated with absorbing materials, the boundary conditions to be satisfied are

$$\partial p/\partial n = -\rho\ddot{w} - \rho\dot{p}/Z \tag{19}$$

where w is the normal displacement of the vibrating sidewall, partition, or a localized panel. Expressing the acoustic pressure in terms of orthogonal modes corresponding to hard walls at x=0,b and y=0,a we write

$$\bar{p}(x,y,z,\omega) = \sum_{i=0}^{\infty} \sum_{j=0}^{\infty} A_{ij}(z,\omega)Y_{ij0}(x,y) \tag{20}$$

in which A_{ij} are the acoustic modal coefficients and Y_{ijk} are the acoustic hard wall modes

$$Y_{ijk}(x,y,z) = \cos(i\pi/b)\ \cos(j\pi y/a)\ \cos(k\pi z/d) \tag{21}$$

The acoustic modal frequencies are

$$\omega_{ijk} = c[(i\pi/b)^2 + (j\pi/a)^2 + (k\pi/d)^2]^{1/2} \tag{22}$$

The solution for the perturbation perssure $\bar{p}$ can be obtained by taking Fourier transformation of Eqs. 2,18 and 19, substituting Eq. 20 into these equations and using the orthogonality condition of the acoustic modes. Then, the sound pressure levels inside the enclosure can be calculated using Eq. 16. Noise generated in the interior by other vibrating surfaces located at x=0,b and/or z=0,d can be estimated by a similar procedure. Then, the total acoustic pressure p inside the enclosure can be obtained from

$$p = p_1 + p_2 + \dots p_n \tag{23}$$

where $p_1, p_2, \dots, p_n$ are the acoustic pressure contributions from the n vibrating flexible parts surrounding the enclosure. If these pressure contributions are assumed to be independent, the spectral density of the total acoustic pressure p can be calculated from

$$S_p(x,y,z,\omega) = S_{p_1}(x,y,z,\omega) + S_{p_2}(x,y,z,\omega) + \dots S_{p_n}(x,y,z,\omega) \tag{24}$$

A detailed treatment on noise generation inside rectangular enclosures can be found in Refs. 34,35,38 and 43.

The solutions for interior acoustic pressure, p, and the sound pressure levels are functions of the structural vibrations at the boundaries of the acoustic space. Next, we obtain solutions for vibration response of cylindrical shells, circular plates and discretely stiffened rectangular panels.

3.3 Dynamic Response of a Cylindrical Shell

Figure 3 shows a cylindrical shell exposed to external and/or internal random point forces. The input forces are taken as stationary and Gaussian random processes which can be located at any arbitrary position on the shell. A Dirac delta function is used to define the location of point load. The external p^e, and the internal p^i, random loads are expressed in terms of two point forces F_1 and F_2 as [26,31,32]

$$p^e(x,\theta,t) = (1/A_1^e A_2^e)\,\{F_1^e(t)\,\delta(x-x_1^e)\,\delta(\theta-\theta_1^e) \tag{25}$$

$$+\,F_2^e(t)\,\delta(x-x_2^e)\,\delta(\theta-\theta_2^e)\}$$

$$p^i(x,\theta,t) = (1/A_1^i A_2^i)\,\{F_1^i(t)\,\delta(x-x_1^i)\,\delta(\theta-\theta_1^i) \tag{26}$$

$$+\,F_2^i(t)\,\delta(x-x_2^i)\,\delta(\theta-\theta_2^i)\}$$

where the superscripts e and i denote the external and the internal loads, δ is the Dirac delta function, and for the cylindrical shell shown in Fig.3, $A_1^e = 1$, $A_2^e = R + h$, $A_i^i = 1$ and $A_2^i = R$. The point loads are assumed to be independent and each characterized by a spectral density. For a space station operation, the point loads could be generated through various mounts and attachments by vibrations of mechanical and electrical equipment, thruster action and other mechanical impacts.

Using the Donnel-Mushtari approximations for thin shells [44,45], the equations of motion for the outward normal displacement w can be written as

$$D\nabla^8 w + (Eh/R^2)\,\partial^4 w/\partial x^4 + \rho_s h \nabla^4 \ddot{w} + \gamma \dot{w} = \nabla^4 \{p^e - p^i\} \quad (27)$$

where

$$D = Eh^3/12(1 - \nu^2) \quad (28)$$

$$\nabla^4 = \partial^4/\partial x^4 + (2/R^2)\,\partial^4/\partial x^2 \partial\theta^2 + (1/R^4)\,\partial^4/\partial\theta^4 \quad (29)$$

$$\nabla^8 = \partial^8/\partial x^8 + (4/R^2)\,\partial^8/\partial x^6 \partial\theta^2 + (6/R^4)\,\partial^8/\partial x^4 \partial\theta^4 \quad (30)$$

$$+ (4/R^6)\,\partial^8/\partial x^2 \partial\theta^6 + (1/R^8)\,\partial^8/\partial\theta^8$$

in which E, ρ_s , ν and γ are modulus of elasticity, material density, Poisson's ratio and viscous damping coefficient, respectively. The general solution to Eq. 27 can be obtained in terms of simply supported shell modes

$$w(x,\theta,t) = \sum_{m=1}^{\infty} \sum_{n=0}^{\infty} A_{mn}(t)\, X^{s}_{mn}(x,\theta) \qquad (31)$$

where $X^{s}_{mn}(x,\theta) = \sin(m\pi x/L) \cos n\theta$. The input loads p^e and p^i are also expanded in terms of the shell modes. Substitution of Eq. 31 into Eq. 27 and use of the orthogonality principle, gives a set of ordinary differential equations in A_{mn}. Solving these equations and utilizing the theory of random processes [46] spectral densities of the displacement response are

$$S_{w}(x,\theta,\omega) = \sum_{m=1}^{\infty} \sum_{n=0}^{\infty} \sum_{r=1}^{\infty} \sum_{s=0}^{\infty} S_{mnrs}(\omega)\, X_{mn} X_{rs} \qquad (32)$$

where S_{mnrs} are the cross spectral densities of the generalized coordinates A_{mn}.

$$S_{mnrs} = H_{mn}(\omega) \cdot H^{*}_{rs}(\omega)\, [S^{e}_{mnrs} + S^{i}_{mnrs}] \qquad (33)$$

The frequency response function H_{mn} and the generalized random forces S^{e}_{mnrs} are

$$H_{mn} = \frac{1}{\rho_s h\, [\omega^2_{mn} - \underset{\sim}{i}\omega\gamma/\rho_s h - \omega^2} \qquad (34)$$

$$S^{e}_{mnrs} = \{S^{e}_{F_1}(\omega)\, X_{mn}(x^{e}_{1}, \theta^{e}_{1})\, X_{rs}(x^{e}_{1}, \theta^{e}_{1}) \qquad (35)$$

$$+ S^{e}_{F_2}(\omega)\, X_{mn}(x^{e}_{2}, \theta^{e}_{2})\, X_{rs}(x^{e}_{2}, \theta^{e}_{2})\}/R^2$$

where $S^{e}_{F_1}$ and $S^{e}_{F_2}$ are the spectral densities of the random point forces $F_1(t)$ and $F_2(t)$. Similar expression can be written for the generalized random forces S^i_{mnrs} acting on the inner side of the shell. The natural frequencies ω_{mn} of a cylindrical shell can be obtained from

$$\omega^2_{mn} = \{(D/\rho_s h)\ [(m\pi/L)^2 + (n/R)^2]^4 + (E/\rho_s R^2)\ (m\pi/L)^4\}/\ [(m\pi/L)^2 + (n/R)^2]^2 \tag{36}$$

The solution for shell vibrations presented in this section can be used in Eq. 4 to obtain noise generated inside a cylindrical enclosure.

3.4 Response of a Double Wall Cylindrical Shell

A double wall shell construction shown in Fig. 4 can be used to represent a design where the interior shell is the pressurized module and the exterior shell is used as a radiation and thermal shield. Following Refs. 31,32,41,42 and using Eq. 27, the shell vibrations can be modeled by two coupled partial differential equations for normal deflections w_E and w_I as

$$D_E \nabla^8_E w_E + (E_E h_E/R^2_E)\partial^4 w_E/\partial x^4 + \rho_E \nabla^4_E \ddot{w}_E + \nabla^4_E\{k_s(w_E - w_I) + c_E \dot{w}_E + (1/3)m_s \ddot{w}_E + (1/6)m_s \ddot{w}_I\} = \nabla^4_E\ p^e(x,\theta,t) \tag{37}$$

$$D_I \nabla_I^8 w_I + (E_I h_I / R_I^2) \partial^4 w_I / \partial x^4 + \rho_I \nabla_I^4 \ddot{w}_I + \nabla_I^4 \{ k_s (w_I - w_E)$$

$$+ c_I \dot{w}_I + (1/3) m_s \ddot{w}_I + (1/6) m_s \ddot{w}_E \} = - \nabla_I^4 p^i(x, \theta, t) \qquad (38)$$

where m_s and k_s are mass per unit area and core stiffness. The subscripts E and I denote the external and the internal shells, respectively. The viscoelastic core separating the two shells is taken to be relatively soft, so that bending and shearing stresses can be neglected, and subsequently the soft core is characterized by a uniaxial constitutive law. Such a model allows in-phase (flexural) and out-of-phase (dilatational) motions of the double wall systems. The vibrations of the inner shell generate noise inside the cylindrical enclosure. However, the motions of the two shells are coupled through the core. Thus, vibrations of the outer shell could induce motions of the inner shell and consequently generate noise in the interior.

The equations of motion of the double wall shells are solved by modal expansion methods. The solution of Eqs. 37 and 38 is expressed in terms of simply supported shell modes

$$w_E(x, \theta, t) = \sum_{m=1}^{\infty} \sum_{n=0}^{\infty} A_{mn}^E \, X_{mn}^S(x, \theta) \qquad (39)$$

$$w_I(x, \theta, t) = \sum_{m=1}^{\infty} \sum_{n=0}^{\infty} A_{mn}^I \, X_{mn}^S(x, \theta) \qquad (40)$$

where A_{mn}^E and A_{mn}^I are the generalized coordinates of external and internal shells, and X_{mn}^S are the shell modes. The solution procedure for shell displacements w_E and w_I are similar to the procedure presented in Sec. 3.3. The details of the response analysis of double wall shells to random point loads are given in Refs. 32 and 42.

3.5 Response of Double Wall Composite Shells

The design of space structures is impacted by the interactions of functional requirements, such as strength, stiffness, weight, reliability, etc. To accomodate many of these requirements, new design concepts for lower weight, extended service life and improved integrity are needed. It has been demonstrated that composite materials could give weight and structural integrity advantages over many commonly used materials [47-50]. However, the low-weight composites might not provide any advantage with respect to less response or reduced noise transmission. Past studies have demonstrated that sandwich constructions might be an efficient way of dissipating vibrational energy [51-54]. Thus, to satisfy the required vibroacoustic environment, designs utilizing composite materials might need to be modified by including the double-wall sandwich concepts.

The sandwich shell system is composed of two simply supported cylindrical shells and a soft viscoelastic core as shown in Fig. 4. Each shell is a composite buildup of laminae, which consists of fibers imbedded in a supporting matrix. The laminae can be oriented in any arbitrary direction. The fibers are basically the load carriers. The equations of motion are derived using assumptions similar to those given in Refs. 26,44 and 45. The viscoelastic core separating the two composite shells is taken to be relatively soft, so that bending and shearing stresses in the core can be neglected. The natural frequencies and vibration response are obtained for simply supported cases by modal solutions and a Galerkin-like procedure. The details of the theoretical formulation and analysis of the double wall composite shells are given in Refs. 32 and 42.

3.6 Response of a Stiffened Shell

The design configuration of the habitability modules is expected to be a discretely stiffened cylindrical shell as shown in Fig. 5. Analytical formulations and response calculations have been performed for the cases where the stiffened shell shown in Fig. 5 is represented by an equivalent orthotropic shell. In this case the effect of rings and stiffeners is smeared into an equivalent skin. Then, the natural frequencies can be calculated by the procedures presented in Ref. 9 and 10. For the application of low frequency vibrations and noise transmission, such a model might be adequate to evaluate the noise criteria inside the habitability modules.

3.7 Vibration of Double Wall Circular Plates

Consider the two circular plates shown in Figs. 4 and 6 are simply supported at the edges. The governing equations of motion of the two plates, coupled through a linear soft core, can be written as [17-24,42]

$$D_T \nabla^4 w_T + c_T \dot{w}_T + m_T \ddot{w}_T + k_s^P (w_T - w_B) + (1/3) m_s^P \ddot{w}_T + (1/6) m_s^P \ddot{w}_B = - p^T(r,\theta,t) \tag{41}$$

$$D_B \nabla^4 w_B + c_B \dot{w}_B + m_B \ddot{w}_B + k_s^P (w_B - w_T) + (1/3) m_s^P \ddot{w}_B + (1/6) m_s^P \ddot{w}_T = p^B(r,\theta,t) \tag{42}$$

where

$$D_{T,B} = E_{T,B} h_{T,B}^3 / 12(1 - \nu_{T,B}^2) \tag{43}$$

$$m_{T,B} = \rho_{T,B} h_{T,B} \tag{44}$$

$$m_s^P = \rho_s^P h_s^P \tag{45}$$

$$\nabla^4 = \left(\frac{\partial^2}{\partial r^2} + \frac{1}{r}\frac{\partial}{\partial r} + \frac{1}{r^2}\frac{\partial^2}{\partial \theta^2}\right)\left(\frac{\partial^2}{\partial r^2} + \frac{1}{r}\frac{\partial}{\partial r} + \frac{1}{r^2}\frac{\partial^2}{\partial \theta^2}\right) \tag{46}$$

The subscripts T,B denote the top and bottom plates and s denotes the core. The loads $p^T(r,\theta,t)$ and $p^B(r,\theta,t)$ are the random excitations applied to the top and bottom plates. In obtaining Eqs. 41 and 42 it was assumed that the mass of the core follows an apportioned linear distribution. The $w_{T,B}$ are the normal displacements of the midsurfaces of the top (exterior) and the bottom (interior) circular plates. The boundary conditions to be satisfied are

$$w_{T,B}(r,\theta) = 0 \qquad \text{at } r = R^P \tag{47}$$

$$- D_{T,B} \left\{\frac{\partial^2 w_{T,B}}{\partial r^2} + \nu_{T,B} \left(\frac{1}{r} \frac{\partial w_{T,B}}{\partial r} + \frac{1}{r^2} \frac{\partial^2 w_{T,B}}{\partial \theta^2}\right)\right\} = 0 \text{ at } r = R^P \tag{48}$$

The solution to Eqs. 41 and 42 can be expressed in terms of normal modes

$$w_T(r,\theta,t) = \sum_{s=0}^{\infty} \sum_{q=1}^{\infty} {}_T A_{sq}(t)\, X^P_{sq}(r,\theta) \tag{49}$$

$$w_B(r,\theta,t) = \sum_{s=0}^{\infty} \sum_{q=1}^{\infty} {}_B A_{sq}(t)\, X^P_{sq}(r,\theta) \tag{50}$$

where ${}_T A_{sq}$ and ${}_B A_{sq}$ are the generalized coordinates of top (exterior) and bottom (interior) circular plates, and $X^P_{sq}(r,\theta)$ are the circular plate modes given by

$$X^P_{sq}(r,\theta) = R_{sq}(r) \cos (s\theta) \tag{51}$$

$$R_{sq}(r) = J_s(k_{sq} r) - \frac{J_s(\lambda^s_{sq})}{I_s(\lambda^s_{sq})} I_s(k_{sq} r) \tag{52}$$

in which J_s and I_s are Bessel functions and modified Bessel functions of the first kind respectively, and λ_{sq}^{s} is the qth root of the frequency equation

$$\frac{J_{s+1}(\lambda)}{J_s(\lambda)} + \frac{I_{s+1}(\lambda)}{I_s(\lambda)} = \frac{2\lambda}{1-\nu} \tag{53}$$

Results given in Eq. 53 are obtained by substituting Eqs. 51 and 52 into Eqs. 47 and 48 and using relationships which relate the derivatives of Bessel functions to higher order functions [24 and 65]. In Eq. 53 $\lambda = kR^P$, $k^4 = \frac{\omega^2 m}{D}$ and consequently

$$\lambda_{sq}^{s} = k_{sq} R^P \tag{54}$$

$$k_{sq}^{4} = {}_{T,B}\omega_{sq}^{2}\; m_{T,B}/D_{T,B} \tag{55}$$

Substituting Eqs. 49 and 50 into Eqs. 41 and 42 and using the orthogonality principle, gives a set of coupled differential equations in ${}_TA_{sq}$ and ${}_BA_{sq}$. Taking the Fourier transform of these equations it can be shown that

$$\begin{aligned} {}_T\bar{A}_{sq}(\omega) = H_{sq}^{T}(\omega)\; \{ {}_B\bar{A}_{sq}(\omega)\; (k_s + (1/6)m_s\omega^2) \\ + {}_T\bar{P}_{sq}(\omega)/\tilde{Q}_{sq}\}/m_T \end{aligned} \tag{55}$$

$$\begin{aligned} {}_B\bar{A}_{sq}(\omega) = H_{sq}^{B}(\omega)\; \{ {}_T\bar{A}_{sq}(\omega)\; (k_s + (1/6)m_s\omega^2) \\ + {}_B\bar{P}_{sq}(\omega)/\tilde{Q}_{sq}\}/m_B \end{aligned} \tag{56}$$

$$H^{T,B}_{sq}(\omega) = 1/\{{}_{T,B}\omega^2_{sq} - \omega^2\gamma_{T,B}/m_{T,B} + \underset{\sim}{i}\omega c_{T,B}/m_{T,B} + k_s/m_{T,B}\} \tag{57}$$

$$\gamma_{T,B} = m_{T,B} + (1/3)m^P_s \tag{58}$$

$$ {}_{T,B}\bar{P}_{sq}(\omega) = \mp \int_0^{R^P}\int_0^{2\pi} \bar{p}^{T,B}(r,\theta,\omega)\; X^P_{sq}(r,\theta)\,r\,dr\,d\theta \tag{59}$$

$$\tilde{Q}_{sq} = \int_0^{R^P}\int_0^{2\pi}\{X^P_{sq}(r,\theta)\}^2 r\,dr\,d\theta = \begin{cases} \pi Q_{sq} & \text{if } s \neq 0 \\ 2\pi Q_{0q} & \text{if } s = 0 \end{cases} \tag{60}$$

$$\begin{aligned} Q_{sq} &= \frac{(R^P)^2}{2}\left\{J_s'^2(\lambda^s_{sq}) + \left(1 - \frac{s^2}{(\lambda^s_{sq})^2}\right) J^2_s(\lambda^s_{sq})\right\} \\ &- \frac{(R^P)^2}{\lambda^s_{sq}}\,\frac{J_s(\lambda^s_{sq})}{I_s(\lambda^s_{sq})}\left\{I_s(\lambda^s_{sq})J_{s+1}(\lambda^s_{sq}) + J_s(\lambda^s_{sq})I_{s+1}(\lambda^s_{sq})\right\} \\ &+ \frac{(R^P)^2}{2}\,\frac{J^2_s(\lambda^s_{sq})}{I^2_s(\lambda^s_{sq})}\left\{\left(1 + \frac{s^2}{(\lambda^s_{sq})^2}\right)I^2_s(\lambda^s_{sq}) - I_s'^2(\lambda^s_{sq})\right\} \end{aligned} \tag{61}$$

$${}_{T,B}\omega^2_{sq} = k^4_{sq}\, D_{T,B}/m_{T,B} \tag{62}$$

Furthermore, a ( )' indicates differentiation with respect to the spatial variable r and a bar indicates transformed quantity.

The excitations applied to the top and/or bottom circular plates are assumed to be uniform random pressure or random point loads as shown in Fig. 6 for which the spectral densities are specified. In the case of uniform pressure input the generalized random forces reduce to

$$
{}_{T,B}\bar{P}_{sq}(\omega) = \left\{ \begin{array}{ll} 2\pi\mu_{0q}\bar{p}^{T,B}(\omega) & s = 0 \\ 0 & s \neq 0 \end{array} \right. \tag{63}
$$

where

$$
\mu_{0q} = \frac{R^{P}}{k_{0q}} \{J_1(\lambda^{s}_{0q}) - \frac{J_0(\lambda^{s}_{0q})}{I_0(\lambda^{s}_{0q})} I_1(\lambda^{s}_{0q})\} \tag{64}
$$

and $\bar{p}^{T,B}(\omega)$ is the Fourier transform for spatially uniform pressure input $p^{T,B}(r,\theta,t)$.

The random loads acting on the top and bottom plates are expressed in terms of two point loads $F^{T,B}_1$ and $F^{T,B}_2$ as

$$
\begin{aligned} p^{T}(r,\theta,t) = (1/A^{T}_1 A^{T}_2)\{&F^{T}_1(t)\ \delta(\theta-\theta^{T}_1)\ \delta(r-r^{T}_1) \\ &+ F^{T}_2(t)\ \delta(\theta-\theta^{T}_2)\ \delta(r-r^{T}_2)\} \end{aligned} \tag{65a}
$$

$$
\begin{aligned} p^{B}(r,\theta,t) = (1/A^{B}_1 A^{B}_2)\{&F^{B}_1(t)\ \delta(\theta-\theta^{B}_1)\ \delta(r-r^{B}_1) \\ &+ F^{B}_2(t)\ \delta(\theta-\theta^{B}_1)\ \delta(r-r^{B}_2)\} \end{aligned} \tag{65b}
$$

where T,B denote the external and internal loads, δ is the Dirac delta function and for a circular plate [26] $A^{B,T}_1 = 1$, $A^{B,T}_2 = r$. The generalized random forces corresponding to point loads given in Eqs. 65a and 65b are

$$
{}_{T}\bar{P}_{sq}(\omega) = \{\bar{F}^{T}_1(\omega)\ X^{P}_{sq}(r^{T}_1,\theta^{T}_1) + \bar{F}^{T}_2(\omega)\ X^{P}_{sq}(r^{T}_2,\theta^{T}_2)\} \tag{66a}
$$

$$
{}_{B}\bar{P}_{sq}(\omega) = \{\bar{F}^{B}_1(\omega)\ X^{P}_{sq}(r^{B}_1,\theta^{B}_1) + \bar{F}^{B}_2(\omega)\ X^{P}_{sq}(r^{B}_2,\theta^{B}_i)\} \tag{66b}
$$

Following the procedures of Ref. 46 and assuming the point loads are stationary and independent, the spectral densities of normal plate deflections w_T, w_B can be determined from

$$S_w^{T,B}(r,\theta,\omega) = \sum_{s=0}^{\infty} \sum_{q=1}^{\infty} \sum_{j=0}^{\infty} \sum_{k=1}^{\infty} \{{}_{T,B}\Theta_{sq} \, ({}_{T,B}\overset{*}{\Theta}_{jk})\, {}_{T,B}S_{sqjk}(\omega) + {}_{P}\Lambda_{sq}({}_{P}\overset{*}{\Lambda}_{jk})\, {}_{B,T}S_{sqjk}\} \; X_{sq}^{P} \cdot X_{jk}^{P} / \tilde{Q}_{sq}\tilde{Q}_{jk} \qquad (67)$$

where

$$ {}_{T,B}\Theta_{sq}(\omega) = \{H_{sq}^{T,B}(\omega)/m_{T,B}\}/\Phi_{sq}^{P}(\omega) \qquad (68)$$

$$ {}_{P}\Lambda_{sq}(\omega) = {}_{T}\Theta_{sq}(\omega) \; \{H_{sq}^{B}(\omega)/m_B\}(k_s + (1/6)m_s\omega^2) \qquad (69)$$

$$ {}_{P}\Phi_{sq}(\omega) = 1 - \{H_{sq}^{T}(\omega)H_{sq}^{B}(\omega)(k_s + (1/6)m_s\omega^2)^2\}/m_T m_B \qquad (70)$$

The asterisks in Eq. 67 denote complex conjugates and ${}_{B,T}S_{sqjk}$ are the cross spectral densities of the generalized random forces.

For the two stationary independent point loads acting on the external plate it may be shown that the cross-spectral density of the generalized forces ${}_{T}S_{sqjk}(\omega)$ may be determined from

$$ {}_{T}S_{sqjk}(\omega) = \{S_{F_1}^{T}(\omega)\; X_{sq}^{P}(r_1^T,\theta_1^T)\; X_{jk}^{P}(r_1^T,\theta_1^T) + S_{F_2}^{T}(\omega)\; X_{sq}^{P}(r_2^T,\theta_2^T)\; X_{jk}^{P}(r_2^T,\theta_2^T)\} \qquad (71)$$

where $S_{F_1}^{T}$ and $S_{F_2}^{T}$ are the spectral densities of the point loads F_1^T and F_2^T. Similar expressions can be developed for point loads acting on the interior plate.

The vibrations of the bottom plate generates noise inside the cylindrical enclosure. By setting $w_B = w_L$ at $x = 0$ and $w_B = w_R$ at $x = L$, substituting these results into Eqs. 6 and 7, the solution for interior noise pressure p_2 can be obtained.

3.8 Response of Stiffened and Interconnected Structures

The interconnected structural system shown in Fig. 7 is composed of a discretely stiffened panel and a cantilever stiffened box beam. The beam is attached to the stiffeners of the skin-stringer panel. The displacement response of the stiffened panel is needed for the solution of the perturbation pressure $\bar{p}$ given in Eq. 20. To develop a solution procedure, the structural system shown in Fig. 7 is separated into a stiffened panel, stiffened beam and a coupled panel-beam structure. The solution procedure is based on transfer matrix techniques.

3.8.1 Response of a Stiffened Panel to Random Loads

The vibrations of various panel units inside the habitability modules might be generated by various mechanical and/or electrical equipment that are attached to these panels.

Consider a flat stiffened panel located on a sidewall at $z = 0$, $a_0 \ll y \ll a_0 + L_y$, $b_0 \ll x \ll b_0 + L_x$ is simply supported at the edges normal to the stiffeners as shown in Figs. 7 and 8. Assume the random loads from the substructure are transferred to the panel at the stiffeners through shear force, bending moment and twisting moment action. Now consider a panel exposed to a random pressure $p^r(x,y,t)$, random point load $F_0(t)$ and random couples $M_y(t)$ and $M_x(t)$. The governing equation of motion for this single bay panel is

$$D\nabla^4 w + c\dot{w} + m_s\ddot{w} = p^r(x,y,t) + F_o(t)\,\delta(x-x_o)\,\delta(y-y_o) + \\ M_y(t)\,\delta(x-x_o)\,\delta'(y-y_o) + M_x(t)\,\delta'(x-x_o)\,\delta(y-y_o) \qquad (72)$$

where D is the plate stiffness, c_o is the visous damping coefficient, m_s is the panel mass per unit area, $w(x,y,t)$ is the normal deflection, δ is the Dirac delta function and the prime denotes a derivative. The point couples acting on a plane parallel to the axis are indicated by the subscript associated with them. Note that in formulating Eq. 72, the effect of acoustic radiation pressure is neglected.

The solution for the panel deflection can be written as

$$w(x,y,t) = \sum_{n=1}^{\infty} q_n(y,t)\; X_n(x) \qquad (73)$$

where q_n are the generalized coordinates and X_n are the modes corresponding to the x-direction. Assuming simply supported edges at $x = 0$, L_x, the modes are

$$X_n(x) = \sin\left(\frac{n\pi x}{L_x}\right) \qquad (74)$$

Taking the Fourier transform of Eqs. 72 and 73 and following the Galerkin procedure, the differential equation for the generalized coordinates $\bar{q}_n(y,\omega)$ can be obtained [34,35,43]. Introducing relationships between various derivatives of

$\bar{q}_n(y,\omega)$ in terms of slope, bending moment and shear, the solution can be written in convenient state vector form as

$$\{Z_n\} = \begin{Bmatrix} \delta_n \\ \theta_n \\ M_n \\ V_n \end{Bmatrix} \tag{75}$$

where δ_n, θ_n, M_n, and V_n are the modal components of deflection, slope, moment and shear, respectively. Then, the response state vector at station j on the panel is

$$\{Z_n\}_j^l = [F]_j \{Z_n\}_{j-1}^r + \int_o^{y_j} [F(y_j - \xi)] \{K_n(\xi)\} d\xi \tag{76}$$

where the superscripts l and r indicate either the left or right of station j, respectively, [F] is the field transfer matrix which transfers the stste vector across the panel [33,37,46] and $\left\{ K_n \right\}$ is the matrix of generalized random forces.

Now that we can transfer the state vector across the panel, we next develop procedures to transfer the state vector across the stiffener. The stiffener does not interfere with the continuity of the deflections and slopes in the skin on either side of the line of attachment between the stiffner and the skin. However, the stiffner, because of its elastic and inertial properties, produces an abrupt change in the moment and shear of the skin at the line of attachment. Since the substructures are attached to the stiffeners as shown in Fig. 7, axial loads will be induced along the coordinate x. The details of developing a transfer matrix for the stiffener can be found in Refs. 37 and 43. Then, the state vector at any arbitrary location s, where

$s = y_s + \sum_{m=1}^{j} y_m$, can be expressed as

$$\{Z_n\}_s^l = {}_s^l[T]_0^l \, \{Z_n\}_0^l + {}_s^l\{E\}_0^l \tag{77}$$

where matrix ${}_s^1[T]_0^1$ transfers the state vector from station 0 to station s such that

$${}_s^l[T]_0^l = [F_s] \, [G_A]_j \, [F]_j \, [G_A]_{j-1} \cdots [F]_1 \, [G_A]_0 \tag{78}$$

in which $[G_A]$ is the point transfer matrix for the jth stiffener, $[F_s]$ is a field transfer matrix which transfers the state vector over a portion of a panel located between stations j and j + 1. Transfer matrix ${}_s^1\{E\}_0^1$ represents the effect of the distributed and concentrated loads acting on the panel and the axial loads acting on the stringers:

$${}_s^l\{E\}_0^l = {}_s^l[T]_0^l \, \{L_0\} + {}_s^l[T]_1^l \, \{L_1\} + \cdots + {}_s^l[T]_j^l \, \{L_j\} + \{L_s\} \tag{79}$$

where the loading matrix L_j is

$$\{L_j\} = \{L_j^P\} + \{L_j^f\} \tag{80}$$

in which

$$\{L_j^f\} = \int_0^{y_j} [F(y_j - \xi)] \ \{K_n(\xi)\} d\xi \tag{81}$$

and matrix $\{L_j^P\}$ includes the effect of the axial loads induced in the stiffeners [43].

The solution for the state vector $\{Z_n\}_0^l$ in Eq. 77 can be obtained by utilizing the boundary conditions at the extreme ends of the panel, i.e. at y = 0 and y = L, and by extending Eq. 77 to the length of the panel. In this approach, simple, fixed, free or elastic supports at the boundaries can be included. For the case when either simple, fixed or free supports are used at the ends (not necessarily the same at both ends), the response state vector at location s can be expressed as

$$\{Z_n\}_s^l = - {}^{l}_{s}\begin{bmatrix} t_{1k} & t_{1l} \\ t_{2k} & t_{2l} \\ t_{3k} & t_{3l} \\ t_{4k} & t_{4l} \end{bmatrix}_0^l \left({}^{r}_{N}\begin{bmatrix} t_{ek} & t_{el} \\ t_{fk} & t_{fl} \end{bmatrix}_0^l \right)^{-1} {}^{r}_{N}\begin{Bmatrix} E_e \\ E_f \end{Bmatrix}_0^l + {}^{l}_{s}\begin{Bmatrix} E_1 \\ E_2 \\ E_3 \\ E_4 \end{Bmatrix}_0^l \tag{82}$$

where the t_{ij} element is the (i,j) element of transfer matrix [T]; E_i is the i-th element of matrix E ; and (k,l) denote the matrix elements corresponding to boundary conditions at the extreme left end (station 0):

$$(k,l) = \begin{cases} (2,4) & \text{simple} \\ (3,4) & \text{fixed} \\ (1,2) & \text{free} \end{cases} \tag{83}$$

Similarly, (e,f) denote matrix elements according to boundary conditions at the extreme right end (station N):

$$(e,f) = \left\{\begin{matrix} (1,3) \\ (1,2) \\ (3,4) \end{matrix}\right\} \begin{matrix} \text{simple} \\ \text{fixed} \\ \text{free} \end{matrix}$$

Finally, the response vector in terms of displacement, slope, moment and shear can be obtained from

$$\{R_e(x,\omega)\}_s^l = \sum_{n=1}^{\infty} \{Z_n\}_s^l \, X_n(x) \tag{85}$$

The displacements from Eq. 85 can be used in Eq. 20 to obtain sound pressure inside a rectangular enclosure.

3.8.2 Response of a Stiffened Beam

Consider a discretely stiffened beam composed of piecewise continuous segments as shown in Fig. 9. Concentrated masses, translational, torsional, longitudinal springs and point dampers can be added to the beam structure at any arbitrary location. Furthermore, random loads (distributed or concentrated) can act at any arbitrary location on the beam.

The deformations, forces, bending and twisting moments of the elastic beam at a given location s can can be represented by a state vector $\{Z_b\}_s^1$. Then, the response state vector can be obtained as with the skin stringer panel. Thus, we write

$$\{Z_b\}_s^l = {}_s^l[T_b]_0^l \{Z_b\}_0^l + {}_s^l\{E_b\}_0^l \tag{86}$$

where the transfer matrices now correspond to those of a where $\{\phi_b, \delta_b, \theta_b\}$ are angles of twist about the elastic axis, vertical displacement, slope in the vertical plane, respectively, and station K is at the base of the connection between the cantilever beam and stiffened panel. The sub matrices $\{T_b^{1u}\}$ and $\{T_b^{1l}\}$ are (3 x 3) reduced transfer matrices of a beam with bending and twisting modes and free boundary condition at z=0 for which the components of the state vector are $\{M_b, V_b, H_b\}_0^1 = \{0, 0, 0\}$. The second part of Eq. 87 reflects the effect of point loads which can be loacted at any arbitrary number of stations r = 0,1,2,...,K-1. Similarly, the submatrices $[T_{b_r}^{2u}]$ and $[T_{b_r}^{2l}]$ are reduced transfer matrices corresponding to the input load vector $\{M_0,F_0,M_T\}r$ in which M_0,F_0 and M_T are the point couple, point force and twisting moment acting at station r.

In the formulation of the skin-stringer problem, it was assumed that in-plane deformations with respect to directions x and y are small and can be neglected. To satisfy the compatibility conditions between the skin-stringer and cantilever beam at the point of attachment K, we assume that for the beam $\{\phi_b\}_K = \{\delta_b\}_K = 0$. Utilizing these conditions and Eq. 87, we obtain

$$\begin{Bmatrix} \psi_b \\ \delta_b \\ \phi_b \end{Bmatrix}_0^l = -\left({}_K^l[T_b^{1u}]_0^l\right)^{-1} \left[\begin{Bmatrix} 0 \\ 0 \\ \phi_b \end{Bmatrix}_K^l + \sum_{r=0}^{K-1} {}_K^l[T_b^{2u}]_r^l \begin{Bmatrix} M_o \\ F_o \\ M_T \end{Bmatrix}_r \right] \qquad (88)$$

At point K where the beam joins the panel, compatibility and equilibrium conditions need to be satisfied. Assume the cantilever beam is connected to a stiffened panel at a distance $x = \alpha$ as indicated in Fig. 7. The slope of the panel-stringer response along the x coordinate can be obtained by differentiating the displacement component of Eq. 77 with respect to x. Then,

$$\{\phi_b\}_K = \sum_{n=1}^{\infty} {}_K^l[t_{11}\ t_{12}\ t_{13}\ t_{14}]_0^l \ \{Z_n\}_0^l \left(\frac{n\pi}{L_x}\right) \cos\frac{n\pi\alpha}{L_x} \tag{89}$$

in which t_{ij} are elements of transfer matrix [T] corresponding to the skin-stringer panel, Eq. 78. Inserting Eq. 89 into Eq. 88 and using the results in Eq. 87, the response bending moment, shear and torsional moment at the connection of the beam to the skin stringer panel can be written as

$$\begin{Bmatrix} M_b \\ V_b \\ H_b \end{Bmatrix}_K = \left[\sum_{r=0}^{K-1} \left(-[T_b^{1l}][T_b^{1u}]^{-1}[T_{b_r}^{2u}] + [T_{b_r}^{2l}] \right) \begin{Bmatrix} M_o \\ F_o \\ M_T \end{Bmatrix}_r \right] + [T_b^{1l}][T_b^{1u}]^{-1} \left[\sum_{n=1}^{\infty} [T^t]\{Z_n\}_o^l \left(\frac{n\pi}{L_x}\right) \cos\frac{n\pi\alpha}{L_x} \right] \tag{90}$$

where transfer matrix $[T^t]$ is

$$[T^t] = {}_K^l\begin{bmatrix} 0 & 0 & 0 & 0 \\ 0 & 0 & 0 & 0 \\ t_{11} & t_{12} & t_{13} & t_{14} \end{bmatrix}_0^l \tag{91}$$

Consider now that the cantilever beam is connected to two adjacent stringers on the panel and that all the loads from the beam are transferred into the stringers at stations j-1 and j. These loads, given in Eq. 90, are functions of $\{Z_n\}_0^1$ and are inputs to the skin-stringer panel system. Then, the response state vector at station x of the stiffened panel is

$$\{Z_n\}_s^l = {}_s^l[T]_0^l \{Z_n\}_0^l - {}_s^l[T]_{j-1}^l \{L_{In}\} - {}_s^l[T]_j^l \{L_{IIn}\} \tag{92}$$

where

$$\{L_{I,IIn}\} = \{0, 0, 0, \mathrm{v}_{I.IIn}\} \tag{93}$$

in which

$$\mathrm{v}_{I.IIn} = \left[-\left(\frac{n\pi}{L_x^2}\right) \cos\frac{n\pi\alpha}{L_x} ,\ \frac{\hat{s}}{2} ,\ \lambda\frac{2}{L_x} \left(\sin\frac{n\pi\alpha_{II.I}}{L_x} - \sin\frac{n\pi\alpha_{I.II}}{L_x}\right) \right] \left\{ \begin{matrix} M_b \\ V_b \\ H_b \end{matrix} \right\}_K \tag{94}$$

In obtaining Eqs. 92 and 94 it was assumed that each stiffener to which the beam is attached shares one-half of the shear. The torsional moment produces loads in the z direction which can be approximated by four forces located at the four corners of the cross-section, each of which is equal to λM_T [56,57]. Also, α_I, α_{II} denote the distances in the x direction of the upper and lower corners of the cross section.

Now for the sake of numerical tractability, we proceed to examine the case where response of the panel is dominated by the bending moment $\{M_b\}_K$. Then, Eq. 94 reduces to

$$v_n = v_{I.II\,n} = -\left(\frac{n\pi}{L_x^2}\right) \cos\frac{n\pi\alpha}{L_x}\,\{M_b\}_K \tag{95}$$

which implies that

$$\{L_n\} = \{L_{I,II n}\} = \{0,0,0,v_n\} \tag{96}$$

Using Eqs. 90, 93 and 95 we can rewrite Eq. 92 as

$$\begin{aligned}\{Z_n\}_s^l = {}_s^l[T]_0^l\,\{Z_n\}_0^l + {}_s^l[D_{In}]\left(\sum_{\tau=0}^{K-1}[D_{II\tau}]\begin{Bmatrix}M_o\\F_o\end{Bmatrix}_\tau\right)\\ + {}_s^l[D_{IIIn}]\left(\sum_{m=1}^{\infty}[D_{IVm}]\,\{Z_m\}_0^l\right)\end{aligned} \tag{97}$$

where

$${}_s^l[D_{In}] = -\left({}_s^l[T]_{j-1}^l + {}_s^l[T]_j^l\right)\{L_n\} \tag{98}$$

$$[D_{II\tau}] = -[T_b^{1s}]\,[T_b^{1u}]^{-1}[T_{b_\tau}^{2v}] + [T_{b_\tau}^{2s}] \tag{99}$$

in which $[T_b^{1s}]$ is a (1 x 3) matrix obtained from $[T_b^{11}]$ by eliminating the second and third rows; $[T_{b_r}^{2s}]$ is a (3 x 2) matrix obtained from $[T_{b_r}^{2u}]$ by eliminating the third column; $[T_{b_r}^{2s}]$ is a (1 x 2) matrix obtained from $[T_{b_r}^{21}]$ by eliminating the second and third rows and third column. Also,

$$ {}^{l}_{s}[D_{IIIn}] = {}^{l}_{s}[D_{In}]\,[T_b^{1s}]\,[T_b^{1u}]^{-1} \tag{100}$$

$$[D_{IVm}] = -\left(\frac{n\pi}{L_x^2}\right)\cos\frac{n\pi\alpha}{L_x}\;[T^t] \tag{101}$$

where $[T^t]$ is given in Eq. 91. Note that the dimensions of matrices ${}^{1}_{s}[T]^{1}_{0}$, ${}^{1}_{s}[D_{In}]$, ${}^{1}_{s}[D_{II\tau}]$, $[D_{IIIn}$ and $[D_{IVm}]$ are respectively, 4x4, 4x1, 1x2, 4x3 and 3x4.

The state vector $\{Z_n\}^1_0$ are $\{z_{nk}, z_{nl}\}$, where k,l are given in Eq. 83 according to the boundary conditions at the extreme left end of the panel. Now we approximate the infinite summation $\sum\limits_{n,m=1}^{\infty}$ with $\sum\limits_{m,m=1}^{\nu}$ where ν is a selected integer number. Then, using Eq. 97 for the entire panel and the boundary conditions at the extreme right end, a system of equations can be written in the following form:

$$[W_\nu]\cdot\begin{Bmatrix} z_{1k}\\ z_{1l}\\ z_{2k}\\ z_{2l}\\ \vdots\\ z_{\nu k}\\ z_{\nu l}\end{Bmatrix}^{l}_{0} = \begin{Bmatrix} N1_1\\ N2_1\\ N1_2\\ N2_2\\ \vdots\\ N1_\nu\\ N2_\nu\end{Bmatrix} \tag{102}$$

where

$$\begin{Bmatrix} N1_n\\ N2_n\end{Bmatrix} = -\,{}^{r}_{N}[D^{ef}_{In}]\sum_{\tau=1}^{K-1}[D_{II\tau}]\begin{Bmatrix} M_o\\ F_o\end{Bmatrix}_{\tau} \tag{103}$$

$$[W_\nu]=\begin{bmatrix} K1_1+R1_{11} & H1_1+S1_{11} & R1_{12} & S1_{12} & \cdots & R1_{1\nu} & S1_{1\nu} \\ K2_1+R2_{11} & H2_1+S2_{11} & R2_{12} & S2_{12} & \cdots & R2_{1\nu} & S2_{1\nu} \\ R1_{21} & S1_{21} & K1_2+R1_{22} & H1_2+S1_{22} & \cdots & R1_{2\nu} & S1_{2\nu} \\ R2_{21} & S2_{21} & K2_2+R2_{22} & H2_2+S2_{22} & \cdots & R2_{2\nu} & S2_{2\nu} \\ \vdots & \vdots & \vdots & \vdots & \ddots & \vdots & \vdots \\ R1_{\nu 1} & S1_{\nu 1} & R1_{\nu 2} & S1_{\nu 2} & \cdots & K1_\nu+R1_{\nu\nu} & H1_\nu+S1_{\nu\nu} \\ R2_{\nu 1} & S2_{\nu 1} & R2_{\nu 2} & S2_{\nu 2} & \cdots & K2_\nu+R2_{\nu\nu} & H2_\nu+S2_{\nu\nu} \end{bmatrix} \tag{104}$$

and

$$\begin{bmatrix} R1_{nm} & S1_{nm} \\ R2_{nm} & S2_{nm} \end{bmatrix} = {}^{r}_{N}[D^{ef}_{IIIn}]\,[D^{kl}_{IVm}] \tag{105}$$

$$\begin{bmatrix} K1_n & H1_n \\ K2_n & H2_n \end{bmatrix} = {}^{r}_{N}\begin{bmatrix} t_{ek} & t_{el} \\ t_{fk} & t_{fl} \end{bmatrix}^{l}_{0} \tag{106}$$

in which the superscripts e,f in matrices ${}^{r}_{N}[D_{In}]$, ${}^{r}_{N}[D_{IIIn}]$ denote rows and k,l in matrix $[D_{IVm}]$ indicate columns retained from the total matrix according to the boundary conditions at stations N and 0, respectively. The values of e,f and k,l are given in Eqs. 84 and 83, respectively. For example, if the panel is simply supported at station N, the first and the third rows of matrix ${}^{r}_{N}[D_{In}]$ are retained. Elements t_{ij} in Eq. 106 are defined as in Eq. 82.

The natural frequencies of the coupled skin-stringer-beam system can be obtained by setting the determinant of matrix $[W_\nu]$ to zero, i.e.,

$$|W_\nu| = \Delta(\omega) = 0 \tag{107}$$

Finally, from Eq. 102, the unknown elements of the state vector at station 0 can be obtained. Then, using Eq. 97, the final expression for the response state vector at any location s on the panel can be expressed as

$$\{Z_n\}^l_s = {}^l_s[A_n] \sum_{r=0}^{K-1} [D_{IIr}] \begin{Bmatrix} M_o \\ F_o \end{Bmatrix}_r \tag{108}$$

where

$${}^l_s[A_n] = {}^l_s[T^{kl}]^l_0 \begin{Bmatrix} z_{nk} \\ z_{nl} \end{Bmatrix}^l_o + {}^l_s[D_{In}] + {}^l_s[D_{IIIn}] \sum_{m=1}^{\nu} [D^{kl}_{IVm}] \begin{Bmatrix} z_{mk} \\ z_{ml} \end{Bmatrix}^l_o \tag{109}$$

Consider now that the bending moment of the stiffened beam is acting in the plane parallel to the y axis. The slope of the panel at the vertical plane along the y coordinate is obtained from

$$\{\phi_b\}_K = \sum_{n=1}^{\infty} {}^l_K[t_{21}\ t_{22}\ t_{23}\ t_{24}]^l_0 \ \{Z_n\}^l_0 \sin\frac{n\pi\alpha}{L_x} \tag{110}$$

where Eqs. 95 and 96 are now replaced by

$$\mathrm{v}_n = \left(\frac{1}{L_x}\right) \sin\frac{n\pi\alpha}{L_x} \ \{M_b\}_K \tag{111}$$

which implies that

$$\{L_n\} = \{0,\ 0,\ v_n,\ 0\} \tag{112}$$

All other expressions remain the same, but now, instead of Eq. 101, we have

$$[D_{IVm}] = \left(\frac{1}{L_x}\right) \sin\frac{n\pi\alpha}{L_x} \; {}^{l}_{K}\!\begin{bmatrix} 0 & 0 & 0 & 0 \\ 0 & 0 & 0 & 0 \\ t_{21} & t_{22} & t_{23} & t_{24} \end{bmatrix}^{l}_{0} \tag{113}$$

As a final case we consider axial forces acting on a beam producing longitudinal vibrations in the beam and transverse vibrations of the skin-stringer panel. Now, the compatibility conditions of the skin-stringer panel and beam interface of the displacements in the z direction are satisfied by setting

$$\{u_b\}_K = \sum_{n=1}^{\infty} {}^{l}_{K}[t_{11}\ t_{12}\ t_{13}\ t_{14}]^{l}_{0}\ \{Z_n\}^{l}_{0}\ \sin\frac{n\pi\alpha}{L_x} \tag{114}$$

Equation 96 remains unchanged, but Eq. 94 needs to be modified to include axial forces. It can be assumed that (1) the axial load

P_b is transferred into the panel as four point forces acting at corners of the cross-section, in which case Eq. 95 is replaced by

$$v_n = \frac{1}{2L_x}\left[\sin\frac{n\pi(\alpha - h_b/2)}{L_x} + \sin\frac{n\pi(\alpha + h_b/2)}{L_x}\right]\{P_b\}_K \qquad (115)$$

where h_b is the length of the beam in x direction; or (2) that the axial load is transferred as distributed forces along the stringer where now

$$v_n = \frac{1}{n\pi h_b}\left[\cos\frac{n\pi(\alpha - h_b/2)}{L_x} + \cos\frac{n\pi(\alpha + h_b/2)}{L_x}\right]\{P_b\}_K \qquad (116)$$

The final solution takes the same form as that of Eq. 108 but Eq. 101 is replaced by

$$[D_{IVm}] = \sin\frac{m\pi\alpha}{L_x}\;[T^t] \qquad (117)$$

4.0 NUMERICAL RESULTS

The numerical results were obtained for single wall cylindrical shells, double wall cylindrical shells, double wall composite shells, stiffened shells, double wall circular plates, rectangular enclosures with vibrating stiffened sidewall panels or partitions and rectangular enclosures of which stiffened sidewalls are interconnected to beam-like type structures. Damping of the shell structures was assumed to be composed of material damping, viscous damping caused by radiation effects, and structural damping of the core material (double wall configuration). Using the complex elastic modulus approach, we have

$$\bar{E} = E^{R}(1 + \underset{\sim}{i}g) \tag{118}$$

where $\bar{E}$ is the complex modulus, E^{R} is the real component of $\bar{E}$, and g is the loss factor. The viscous damping coefficients were expressed in terms of modal damping ratios ζ_{mn}^{e} and ζ_{mn}^{i} corresponding to the external and internal shells. Damping in the core is introduced through the core stiffeness constant $k_s = k_o(1 + \underset{\sim}{i}\, g_s)$ where g_s is the loss factor for the core material. Similar damping model was used for the double wall circular plates. For stiffened panel and stiffened beam vibrations, damping was introduced by replacing elastic modulus E and shear modulus G with $E(1 + \underset{\sim}{i}g)$ and $G(1 + \underset{\sim}{i}\, g)$. Furthermore, the translational, k_{T1}, and rotational, k_{R1}, spring constants of the cantilever beam construction were replaced with

$k_{T_1}(1 + \underset{\sim}{i}\, g_1)$ and $k_{R_1}(1 + \underset{\sim}{i}\, g_1)$, respectively, where g_1 is the loss factor for the external springs. The effect of viscous damping was neglected for those structures.

4.1 Noise Transmission Into a Cylindrical Enclosure

4.1.1 Single Wall Aluminum Shell

The aluminum shell shown in Fig. 3 has the following dimensions: L = 300 in., R = 58 in. and h = 0.1 in. Both ends are closed and the interior walls are lined with a layer of porous acoustic material [40]. The inputs to the shell are exterior random point loads located at $x_1 = x_2 = 150$ in., $\theta_1 = -90^0$ and $\theta_2 = 90^0$. These point forces are characterized by truncated Gaussian white noise spectral densities

$$S_{F_1^e,\, F_2^e} = \begin{Bmatrix} 0.84\ \text{lb}^2/\text{Hz} & 0 < f < 1000\ \text{Hz} \\ 0 & \text{otherwise} \end{Bmatrix} \qquad (119)$$

The elastic modulus, Poisson's ratio and the material densities were respectively, $E = 10.5 \times 10^6$ psi, $\nu = 0.3$ and $\rho_m = 0.000259$ $\text{lb}_f\text{-sec}^2/\text{in.}^4$. The speed of sound, c, in the enclosure, the air density ρ and flow resistivity of porous acoustic material lining, R_1, of the interior surfaces are taken to be c = 13540 in/sec., $\rho = 1.147 \times 10^{-7}\ \text{lb}_f\text{-sec}^2/\text{in}^4$ and $R_1 = 3.74 \times 10^{-3}\ \text{lb}_f\text{-sec/in.}^4$. The sound pressure levels are computed inside the shell at x = L/2, r = 28 in. and $\theta = 45^0$. The structural modal damping coefficients were taken to be constant, $\zeta_{mn} = \zeta_0 = 0.04$. The deflection response levels RL are calculated from

$$RL(x,\theta,\omega) = 10 \log [S_w(x,\theta,\omega) \Delta\omega/w_{ref}^2] \qquad (120)$$

where S_w is the deflection response spectral density and w_{ref} = h. Numerical procedures were developed to calculate modal frequencies, deflection response spectral densities and interior sound pressure levels. Pressurized and unpressurized modules were considered.

The deflection response levels calculated at x = L/2 and $\theta = 45^0$ are given in Fig. 10 for pressurized and unpressurized shell. The effect of pressurization is to shift some of the lower frequency response peaks to a higher frequency values. Similar results are shown in Fig. 11 where sound pressure levels are plotted versus frequency. Since interior sound pressure is dominated by the modes (structural and acoustic) above 300 Hz, pressurization does not have much of an effect on sound pressure levels. It should be noted that the magnitudes of the point loads chosen in this study are arbitrary values. When the actual input force values are known, the results presented in this report can be scaled accordingly. For example, if the actual input forces are ten times less than the ones used in this study, the RL and the SPL levels given in Figs. 10 and 11 will be reduced by ten decibels.

4.1.2 Double Wall Aluminum Shell

Numerical results presented herein correspond to the double wall sandwich shell shown in Fig. 4 and input point loads as given in Fig. 6. The magnitude and location of the inputs acting either on the exterior shell or the interior shell are assumed to be the same as prescribed by Eq. 119. The thicknesses of the external and internal shells are $h_E = 0.032$ in and $h_I = 0.1$ in. The stiffness, material density and thickness of the soft core are $k_s = 4.17\ lb_f/in^3$, $\rho_s = 3,4 \times 10^{-6} lb_f - sec^2/in^4$ and $h_s = 2$ in., respectively.

The natural frequencies of a double wall aluminum shell are given in Fig. 12. For the double wall shell construction, the flexural (in phase) and the dilatational (out of phase) modes are included. The highest modal frequency is that of "breathing" mode for which $n = 0$ and $m = 1$. Results plotted in Fig. 12 indicate that for the large shell dimensions and the ratio radius/length = 0.1933 chosen in this study the modal frequencies at $n = 0$ seem to converge to a single point for all values of $m = 1,2,\ldots,10$. This suggests that in the vicinity of the "breathing" mode frequency large numbers of structural modes could couple to acoustic modes resulting in high levels of noise transmission. The deflection response levels of the outer shell are given for pressurized and unpressurized conditions in Fig. 13. These results correspond to $x = L/2$, $\theta = 45^0$, $g_s = 0.05$, $\zeta_0 = 0.04$ and inputs provided by two point loads acting on the interior shell at $x_1^i = x_2^i = 150$ in., $\theta_1^i = -90^0$ and $\theta_2^i = 90^0$. As can be seen from these results, shell response is dominated by low frequency modes in the range 0-50 Hz. In Fig. 14, sound pressure levels in the cylindrical enclosure generated by two interior point loads are given for reverberant (hard interior walls) and absorbent (interior walls treated with soft acoustic materials) conditions. For reverberant conditions, noise levels inside the cylinder become relatively large and are dominated by peaks at acoustic resonant frequencies. The effect of pressurization on noise transmission in the interior is shown in Fig. 15 for absorbent interior wall conditions. Those results tend to indicate that pressurization plays only a minor role on noise generation inside the shell. It is expected that the habitability modules will be pressurized for which static pressure differential $\Delta p = 11.8$ psi . The interior sound pressure generated by identical inputs but acting at different locations is given in Fig. 16. As can be observed from these results, noise generated by shell vibrations is a function of location of random point loads.

4.1.3 Double Wall Composite Shell

The dimensions of the double wall composite shell are the same as those of double wall aluminum shell. The outer shell consists of three laminae while the inner shell is composed of ten laminae. Fiberglass and graphite fibers are used to reinforce the plexiglass material. The ratio of fibers volume to the plexiglass volume is 0.2. The fiber orientation is prescribed by angle α as shown in Fig. 4. The elastic moduli, Poisson's ratios and material densities are $E_f = 7.75 \times 10^6$ psi, $\nu_f = 0.33$, $\rho_f = 0.0002$ $lb_f\text{-}sec^2/in^4$, $E_g = 10.5 \times 10^7$ psi, $\nu_g = 0.33$, $\rho_g = 0.00015$ $lb_f\text{-}sec^2/in^4$, $E_p = 2.35 \times 10^5$ psi, $\nu_p = 0.35$, $\rho_p = 0.00011$ $lb_f\text{-}sec^2/in^4$, where the subscripts f,g,p denote fiberglass, graphite and plexiglass, respectively. The fiber reinforcement--same pattern is used for internal and external shell--is arranged as follows: 1st layer fiberglass, 2nd layer graphite, 3rd layer fiberglass and so on. The fiber orientation for the three laminae of the exterior shell are $\alpha = -45^0, 45^0, -45^0$ (first case) and $\alpha = 90^0, 0^0, 90^0$ (second case). The fiber orientation for the ten laminae of the interior shell is arranged in an alternating order with

$\alpha = -45^0, 45^0, -45^0, 45^0$, etc. (first case) and

$\alpha = 90^0, 0^0, 90^0, 0^0$, etc., (second case).

The natural frequencies of double wall composite shell are plotted in Fig. 17. A comparison of modal frequencies of aluminum and composite shells shows that depending on fiber reinforcement orientation, significantly higher modal frequencies can be obtained for a composite shell. However, the mass of the composite shell is about 50% less than that of the aluminum shell while all other geometric parameters remain the same. The deflection response levels for point loads acting on the exterior surface are shown in Fig. 18a for modal damping coefficient $\zeta_0 = 0.01$ and loss factor in the core $g_s = 0.02$. As can be seen from these results, a large number of flexural and dilatational modes are excited by point loads. Due to the large number of participating modes and modal frequency overlaps as shown in Fig. 17, it is difficult to identify the response peaks corresponding to dilatational frequencies. However, for n = 0 the flexural and dilatational frequencies are well separated. A direct comparison of these results to the results given in Fig. 13 indicate that at most frequencies the response levels of the composite shell are lower than when compared to the response levels of the aluminum shell. However, at some frequency values the opposite is true. Similar results are presented in Fig. 18b but for the point loads acting on the interior shell. As can be seen from Figs. 17 and 18b, response levels at the first three peaks are about the same for both of these cases. However, significantly different vibration levels might be observed at other frequencies when the input point loads are moved from external to internal shells. The location and magnitude of these loads are the same for both cases.

To demonstrate the effect of shell and core damping, results are presented in Figs. 19 and 20 for constant modal damping ratios $\zeta_{mn}^{E} = \zeta_{mn}^{I} = \zeta_{o} = 0.04$ and $g_s = 0.1$. The point loads are acting on the interior shell for both of these cases. By increasing modal damping of the interior and exterior shell from 0.01 to 0.04, about 12 dB of response reduction can be gained at most modal frequencies. As can be seen from Figs. 19 and 20, only about 2-4 dB of the response reduction is achieved at some peaks when damping in the core is increased from 0.02 to 0.1. However, the shells forming a double wall construction are bonded to the core. Thus, the cumulative effect of damping on vibration response would be similar to the combined results given in Figs. 19 and 20.

Figure 21 depicts sound pressure levels for an aluminum and fiber reinforced laminated shell under exterior point load inputs, with $\zeta_{mn}^{E} = \zeta_{mn}^{I} = 0.01$, $g_s = .02$ and $\beta = 1. \times 10^{-8}$ rad-sec/in^2 . As can be observed from these results, the noise levels generated by a composite shell are higher than the noise levels for an aluminum shell at most frequencies. The mass of the composite shell is about one half of the mass of the aluminum shell. However, the composite shell is much stiffer than the aluminum one. For a shell structure, a shift in modal frequency could induce different coupling between structural and acoustic modes. The effect of structural and acoustic damping on sound generation is illustrated in Figure 22. These results correspond to $\beta = 1 \times 10^{-8}$ rad-sec/in^2. As can be seen from these results, a significant amount of noise reduction can be achieved in a composite shell by increasing structural and acoustic damping. The results shown in Fig. 22 indicate that for acoustically hard interior walls $(Z_A \to \infty)$, the noise levels in the cylinder become relatively large.

A direct comparison of interior sound pressure levels in the cylinder excited by exterior and interior point loads is given in Fig. 23. The loading conditions are the same for both cases. Since vibration coupling is provided by the viscoelastic core, the noise generated in the interior is a function of how the point loads are acting on the double wall shell. The results presented in Fig. 23 correspond to point loads acting on the interior shell at $x_1^i = x_2^i = L/2$, $\theta_1^i = -90^0$ and $\theta_2^i = 90^0$. The fiber orientation of the three layers (Fig. 4) at the exterior shell is described in Fig. 24. The fiber orientation for the ten layers of the interior shell are: (A) 0°,22.5°,45°,45°,22.5°, 0°,90°,90°,90°,90° (B) 90°,0°,90°,0°,90°,0°,90°,0°,90°,0° (C) -45°,45°,-45°,45°,-45°,45°,-45°,45°,-45°,45°. These results show that shell response and interior noise are functions of fiber orientation in a composite shell. The interior noise levels might be tailored to meet specific needs by selecting a suitable fiber orientation. However, interior noise is a function of frequency and only specific frequency bands might be affected by this procedure.

4.1.4 Discretely Stiffened Cylindrical Shell

Analytical formulations and noise transmission calculations have been performed for the case where the stiffened shell shown in Fig. 5 is represented by an equivalent orthotropic shell model. The solution procedure for shell response and noise transmission is similar to a monocoque shell presented in Secs. 3.1, 3.3 and 4.1.1, but the natural vibration frequencies and mass of the stiffened shell structure are calculated by the methods presented in Ref. 10. For the application to low frequency (below 1000 Hz) vibrations and noise generation, such a model might be adequate to evaluate noise transmission characteristics of space station habitability modules. The structural parameters chosen in this study are typical of the proposed habitability modules where $L = 420$ in., $R = 78$ in and $h = 0.1$ in. Skin and stiffening elements (rings and stringers) are constructed from aluminum with the following section and material properties:

A_r = (cross-sectional area, ring) = 1.897 in^2

A_s = (cross-sectional area, stringer) = 0.252 in^2

I_r = (moment of inertia of ring about its centroid) = 5.294 in^4

I_s = (moment of inertia of stiffener about its centroid) = 0.255 in^4

J_r = (torsion constant for ring) = 0.1152 in^4

J_s = (torsion constant for stiffener) = 0.000302in^4

$E = E_r = E_s$ (moduli of elasticity) = 10.0×10^6 psi

$G = G_r = G_s$ (shear moduli) = 3.846×10^6 psi

$\nu = \nu_r = \nu_s$ = (Poisson's ratio) = 0.3

$\rho_s = \rho_r = \rho_s$ = (material density) = 0.000259 lb-sec^2/in^4

The natural frequencies of the orthotropic shell are shown in Figs. 25 and 26 for two different cases of structural configuration. The modal frequencies for the first few circumferential modes (N = 0,1,2,3) are not affected much by the number of ring frames. However, for mode numbers larger than N =3, the ring frames have a strong effect on modal frequencies. Furthermore, for the circumferential wave numbers larger than six and longitudinal modes higher than ten, the modal frequencies tend to converge to a single line. From these results, it can be seen that at each selected frequency several modes could be contributing to structural response and noise transmission. The noise transmission inside the cylindrical enclosure shown in Fig. 5 was calculated for a variety of structural configurations. The inputs are point loads acting at $x_1 = x_2 = L/2$, $\theta_1 = 90^0$, $\theta_2 = -90^0$. These inputs are assumed to be stationary Gaussian white noise random processes characterized by truncated spectral densities

$$S_{F_1} = S_{F_2} = \begin{Bmatrix} 0.01 \text{ lb}^2/\text{Hz} & 0 \ll f \ll 1000 \text{ Hz} \\ 0 & \text{otherwise} \end{Bmatrix} \qquad (121)$$

It is assumed that some absorbent acoustic material is intact at the interior walls of the cylindrical enclosure.

The generated interior SPL in the enclosure at $x = L/2$, $\theta = 45^0$ and $r = 68$ in are presented in Fig. 27 for several geometric stiffening configurations. For the stiffened cases it is assumed that only transverse rings are present as stiffening elements. As can be seen from these results, at low frequencies (below 150 Hz) interior noise levels for unstiffened shells are higher when compared to the results of a stiffened case. However, for frequencies above 150 Hz, higher noise levels might be generated at some frequencies for a shell stiffened with rings. This could be due to the fact that the acoustic modes at these frequencies are strongly coupled to the shell structural modes. The sound pressure levels for a pressurized shell stiffened with 10 rings and stringers which are spaced at 10 inches apart are given in Figure 28. The results tend to indicate that more interior noise is generated by a thinner shell. The effect of stringers on interior noise levels is illustrated in Fig. 29. As can be seen from these results, the sound pressure levels do not change by much when stringers are added to the positions shown in Fig. 30. These results correspond to a shell stiffened with ten heavy frames and stringers which are spaced 10 inches apart. The sensitivity of noise generation due to different locations of input forces is clearly demonstrated in this figure. Structural modes which are not excited for a particular forcing condition might become efficient sound radiators for a different set-up of input forces.

Numerical results were also obtained for a shell stiffened with relatively small ring frames. The structural parameters selected are:

$A_r = 0.228\ \text{in}^2$
$A_s = 0.295\ \text{in}^2$
$I_r = 0.4437\ \text{in}^4$
$I_s = 0.5087\ \text{in}^4$
$J_r = 0.000122\ \text{in}^4$
$J_s = 0.000246\ \text{in}^4$

The material properties are the same as given in the previous examples. A comparison of interior sound pressure levels for the two cases of different ring frame stiffening is shown in Fig. 31. These results indicate that interior noise levels are significantly higher for a shell stiffened with small frames (frequency range 50-500 Hz). The results shown in Fig. 32 show the effect of increasing the number of small frames from 10 to 41. In the frequency ranges 50-200 Hz, 400-500 Hz, interior noise levels are higher for a shell stiffened with 41 small ring frames than for a shell stiffened with 10 heavy frames. However, for frequencies above 750 Hz more noise is transmitted when ring frames are large.

The results presented indicate the sensitivity of interior noise environment inside the habitability modules due to changes in structural, geometric and loading conditions. These results were obtained for a particular level of the point load intensity. At the present time, the magnitude characteristics and location of mechanical inputs that will be present in the habitability modules during orbital operations are not known. The measurements obtained for the Skylab operations shown in Figs. 33 and 34 indicate typical interior noise levels. In general noise levels generated by various mechanical or electrical components are relatively low, but the total level might reach about 80 dB at some frequencies.

4.1.5 End Plates

Consider noise is being generated by vibration of double wall end plates which are excited by point loads as illustrated in Fig. 6. The core separating the double wall end plate construction is taken to be relatively soft in order to allow for dilatational modes to be present. The coupled modal frequencies of the double wall aluminum caps for $s = 0,1,2,3$ (number of nodal diameters) and $q = 1,2,\ldots,10$ (number of nodal circles) were calculated. The first three structural modes for zero number of diametrical nodes are shown in Fig. 35.

In Fig. 36, the first three radial acoustic modes are illustrated. These results were obtained from Eq. 14 for zero number of nodal diameters (i.e., $j = 0$, no variation in θ - direction) and $k = 1,2,3$, where k represents the number of nodal circles (r-direction).

The sound pressure levels at x = L/2, r = 23 in. and θ = 45° due to noise transmitted through the double wall circular end plates located at x = L, are shown in Fig. 37 for reverberant and absorbent interiors. The input is a uniform 120 dB acoustic pressure acting on the exterior end plate. In this case, the end plate located at x = 0 is assumed to be rigid. The reverberant and absorbent conditions are simulated by selecting Z_L, $Z_R \to \infty$, $\beta = 0$, and Z_L, Z_R as given in Eq. 9 and $\beta = 1 \times 10^{-7}$ rad-sec/in^2, respectively. As can be seen from Fig. 37, a large number of acoustic modes are excited by the vibration of the end plates for reverberant conditions. Modal plate damping is taken to be constant and equal to $\zeta^T_{sq} = \zeta^B_{sq} = 0.06$. The structural loss factor of the core $g^P_s = 0.02$. The noise transmission of the end caps is predominantly low frequency. The fundamental circular plate frequency is 3.73 Hz while the lowest acoustic modal frequency in the shell enclosure is 22.56 Hz. From these results it can be seen that under uniform random pressure input, the noise transmitted by the double wall shell and circular end plates could be relatively large over the selected frequency range.

The results presented in Fig. 38 illustrate the difference between the noise transmitted due to a uniformly distributed acoustic pressure input and sound generated by point loads. In both cases, the random excitations are acting on the exterior plate of the double wall construction located at x = L and the end plate located at x = 0 is assumed to be rigid. The uniform input is 120 dB acoustic pressure and the two point loads are characterized by a truncated Gaussian white noise spectral density given by Eq. 119 and are located at $r_1^T = r_2^T = 28$ in. and $\theta_1^T = -90^0$, $\theta_2^T = 90^0$. The absorbent conditions are described in Eq. 9 and the equivalent acoustic damping parameter is $\beta = 1 \times 10^{-7}$ rad-sec/in^2. The modal damping ratios are taken to be constant and equal to 0.06. The loss factor of the core $g_s^p = 0.02$. The sound pressure levels are calculated at x = L/2, r = 23 in., $\theta = 45^0$. From Fig. 38 it can be seen that the uniform acoustic pressure tends to generate more noise in the low frequency region while the sound generated by point loads inside the enclosure is about 10-15 dB higher in the high frequency region.

4.1.6 Total Interior Noise

Due to the assumption of independently vibrating double wall shell and end plate systems, the total interior pressure can be calculated by a superposition of the individual contributions. In Fig. 39 results are shown of noise generated inside the enclosure due to uniform random pressure applied on the exterior surfaces of the double wall shell and double wall end plates. It can be seen that transmitted noise is dominated by end plate vibrations for frequencies up to 200 Hz and by shell vibrations for frequencies above 200 Hz. Then, the total interior pressure is presented in Fig. 40. These results indicate that neglecting noise transmitted by the end caps would underestimate interior sound pressure levels for the low frequency region. Similar results are presented in Figs. 41 and 42 but for random point load inputs. These loads were applied on the exterior surfaces of the shell and end plate systems. As can be observed from these results, low frequency noise is dominated by end plate motions.

4.2 Structural Response and Noise Transmission of Rectangular Enclosures

Numerical results have been obtained for several simplified versions of the interconnected structure shown in Fig. 7. Examples of such simplified structural systems are given in Figs. 43,44 and 45. The stiffened panel is taken to be composed of three equal bays. The supports at $y = 0$ and $y = L_y$ are assumed to be elastic stiffeners. The stiffeners are identical and placed at equal distances, $y_1 = y_2 = y_3 = 8.2$ in. and $L_x = 20$ in. The physical parameters for the aluminum panel and stiffeners are typical of a transport jet aircraft [9]. For the special case shown in Fig. 43, the box beam is not attached to the skin-stringer system and inputs to the structure are provided by four random point forces or four point couples. The geometric parameters of the box beam shown in Fig. 44 are $L_b = 60$ in., $A = 12.48$ in^2 (cross-sectional area), $I_y = 35.127$ in^4 (second moment of area about y-axis and $I_x = 35.127$ in^4 (second moment of area about x-axis). To reflect the effect of different box beam geometries, cross-sectional areas and second moments of inertia were adjusted for different values of beam height H and beam thickness t_1 and t_2. The sectional properties for the piecewise continuous box beam shown in Fig. 45 are $A_1 = 5.814$ in^2, $A_2 = 9.196$ in^2, $A_3 = 12.48$ in^2, $I_{y1} = 2.115$ in^4, $I_{y2} = 12.265$ in^4, $I_{y3} = 35.127$ in^4 and the distances between the continuous segments are $z_1 = z_2 = z_3 = 20$ in. Numerical results were also obtained for cases with concentrated mass ($m_1 = 0.5$ lb_f-sec^2/in), and a translational spring ($k_{T1} = 9000$ lb/in) and rotational spring ($k_{R1} = 2 \times 10^7$lb-in/rad) attached at station $z = z_1$. Inputs to the beams are the concentrated couples M_{ox} or M_{oy} which act at the centroid of the cross-sectional area at $z = 0$. All the structural elements are assumed to be made from the same aluminum material as the skin-stringer panel. Damping in the skin-stringer-beam structure is introduced by replacing the elastic modulus E and shear modulus G with $E(1 + \underset{\sim}{i}g)$ and $G(1 + \underset{\sim}{i}g)$ where g is a loss factor. Furthermore, the translational, k_{T1}, and rotational, k_{R1}, spring constants are replaced with $k_{T1}(1 + \underset{\sim}{i}g_1)$ and $k_{R1}(1 + \underset{\sim}{i}g_1)$, respectively where g_1 is the loss factor for the two external springs. The effect of viscous damping is neglected by setting the viscous damping coefficient to zero.

Numerical results were also obtained for a large rectangular enclosure of which the dimensions could be representative of interior dimensions of the space station construction. The geometry of such an enclosure is shown in Fig. 46. The noise in the interior is generated by vibrations of panels or partitions which can be located at any arbitrary position on the enclosure. Vibrations to these panels might be induced by various mechanical and electrical equipment such as fans, life support systems, printers, experimental devices, etc.

4.2.1 Response of Stiffened Panel to Point Forces and Point Couples

The four point forces or four point couples are assumed to be of equal strength and characterized by truncated Gaussian white noise spectral densities

$$S_{F_i} = \begin{Bmatrix} 0.84 \ \mathrm{lb}^2/\mathrm{Hz} & 0 \ll f \ll f_u \\ 0 & \text{otherwise} \end{Bmatrix} \tag{122}$$

$$S_{M_i} = \begin{Bmatrix} 0.84(\mathrm{lb\text{-}in})^2/\mathrm{Hz} & 0 \ll f \ll f_u \\ 0 & \text{otherwise} \end{Bmatrix} \tag{123}$$

where f is the frequency in Hz, i = 1,2,3,4 and f_u is the upper cut-off frequency. These point loads are located at the positions as indicated in Fig. 43. The response spectral densities corresponding to point force inputs are given in Fig. 47. These results are for an upper cut-off frequency $f_u = 800$ Hz. The panel deflection response is calculated at x = 10 in., y = 4.1 in. and y = 8.2 in. The first point is at the middle of the first panel bay while the second point is at the middle of the first stringer. Depending on the value of frequency, significant differences in response values are obtained at different locations of the panel. Similar results are presented in Fig. 48 for x = 5 in., y = 12.1 in. and several values of the structural damping coefficient g. A large amount of response reduction can be achieved by increasing the structural damping.

Deflection response spectral densities for point couple inputs are shown in Fig. 49 for two different values of input conditions. From the results presented in Figs. 47 and 49, differences can be seen in the skin-stringer panel response between the point force and the point couple inputs.

4.2.2 Response of Stiffened Panel to Calculated Bending Moment Inputs

The response of a stiffened panel to calculated point couple inputs was obtained. These inputs were determined from the response solution of the cantilever beam shown in Fig. 44. The beam is assumed to be clamped at $z = L_b$ and free at $z = 0$. The bending moment spectral densities were calculated at the root of the cantilever beam. The spectral densities shown in Fig. 50 for two different cross-sectional areas of the box beam are then used as point couple inputs to the stiffened panel. The response spectral densities of the skin-stringer panel calculated at x = 5 in. and y = 12.3 in. are shown in Fig. 51 for two different geometries of the cantilever beam. The inputs to the panel are assumed to be acting on two adjacent stringers at a distance α = 6.666 in. as shown in Fig. 7. The solid line given in Fig. 51 corresponds to a beam with a fundamental bending frequency of 52 Hz, while the conditions represented by a dashed line are for a beam with a natural frequency of 123 Hz. Since the natural frequency of one of the skin-stringer panel modes is approximately 123 Hz, a very strong peak appears in the response spectral density when the beam resonant frequency coincides with one of the skin-stringer panel's resonant frequencies. Therefore, the dynamic conditions of such substructures could play a significant role in controlling the response levels of a stiffened sidewall.

The effect of direction of the input point couple action is illustrated in Fig. 52. The dashed line illustrates skin-stringer panel response at point x = 5 in. and y = 12.3 in for M_{ox} input (bending effect on the stringers) and the solid line is for M_{oy} (twisting effect on the stringers) input. These results indicate that the deflection response is significantly smaller for bending moment input M_{ox} than for twisting moment input M_{oy}. This is due to the fact theat these stiffeners provide more resistance in bending than in torsion.

4.2.3 Response of a Coupled Skin-Stringer-Beam Structure

Skin-stringer panel response was calculated for the geometries shown in Figs. 44 and 45. The inputs are point couples M_{ox}, for which the spectral densities are given in Eq. 123, with an upper cut-off frequency of 320 Hz. A direct comparison of the results is given in Fig. 53 for the cases of a completely coupled problem (Fig. 44) and under special conditions where the inputs to the skin-stringer panel are the bending moments of a clamped-free beam. When the box beam is attached to an elastic stringer, the mechanism for transmitting vibrational energy into the stiffened panel is different for separately calculating the bending moment of the cantilever beam and then using the results as inputs to the skin-stringer panel. Results indicate the response levels of the coupled problem are lower at most of the frequencies.

The effect of different beam geometries on skin-stringer panel response is illustrated in Fig. 54 for the structure shown in Fig. 44. The deflection response spectral densities of the skin-stringer-beam structure shown in Fig. 45 are presented in Fig. 55 for damping coefficients $g = 0.02$ and $g_1 = 0.05$. These results illustrate the effect of the concentrated mass and elastic springs attached to the beam at station $z = z_1$. Skin-stringer panel vibrations are particularly sensitive to changes in beam dynamic characteristics in the frequency range of approximately 10 Hz to 80 Hz. The first beam bending mode occurs in this frequency range and moves to lower frequencies with the addition of mass and to higher frequencies with the attachment of elastic springs. By adjusting the structural and geometric parameters of the box beam structure, the response characteristics of the skin-stringer panel can be tailored to prescribed conditions.

4.2.4 Noise Transmission

For the calculation of noise transmission into an enclosure, the simplified models shown in Figs. 56 and 57 have been chosen. A cantilever box beam is attached to two stiffeners of a discretely stiffened sidewall. A random poit couple acts at the free end of the cantilever beam. The walls at z = 0 and z = d of the acoustic enclosure are treated with uniformly applied absorptive materials which are represented by a point impedance model as given in Eq. 9. The results obtained here are for R_1 = 4×10^4 mks rayals/m. The point couple $M_{ox}(t)$ acting on the cantilever beam is assumed to be characterized by a truncated Gaussian white noise spectral density given in Eq. 123. The upper cut-off frequency was chosen to be f_u = 600 Hz.

Numerical results were obtained for a = 142 in., b = 50 in., d = 48 in., a_o = 60 in., b_o = 15 in., $y_1 = y_2 = y_3$ = 8.2 in., L_x = 20 in., L_y = 24.6 in., I_y = 38.127 in^4 (second moment of area of box beam), A = 12.48 in^2 (cross-sectional area of the box beam), L = 60 in. (beam length) and α = 6.666 in. Interior noise in the enclosure was calculated at x = 25 in., y = 71 in., and z = 24 in. Noise transmission calculations were obtained for a loss factor for the panel g = 0.02. The acoustic damping coefficient β was related to the acoustic modal damping ratios ξ_{ij} by

$$\xi_{ij} = \frac{\beta c^2}{2\omega_{ijo}} \tag{124}$$

where $\beta c^2 = 2\omega_o \xi_o$, in which ω_o is the lowest acoustic modal frequency chosen from ω_{001}, ω_{010}, and ω_{100} (i.e., ω_{010} in our case). The damping ratio corresponding to the fundamental acustic mode, $\xi_o = 0.03$, takes into account the contributions of all the damping effects of the acoustic space. Air density and speed of sound in the enclosure are $\rho = 1.147 \times 10^{-7}$ lb_f-sec^2/in^2 and c = 13540 in/sec., respectively. All the calculations are based on a frequency bandwidth $\Delta f = 1$ Hz.

Sound pressure levels are given in Fig. 58 for an acoustic enclosure with a small amount of absorption at the walls ($Z_A \to \infty$), and for the case where the walls are treated with porous materials for which the point impedance is given in Eq. 9. In this case, as shown in Fig. 58, the inputs to the stiffened panel are four point forces acting on the two intermediate stringers for which the spectral densities are assumed to be the same and equal to $0.84 \times 10^{-3} lb^2/Hz$. As can be observed from these results, the peaks of the acoustic modes are suppressed when the acoustic absorption in the interior is large.

The results presented in Fig. 59 are for the beam-skin-stringer geometry shown in Fig. 56 and acoustic absorption as prescribed by Eq. 9. The two cases correspond to two different dynamic characteristics of the beam where f_1^b is the fundamental bending frequency of a clamped-free cantilever beam. In this case, the bending moment response spectral density of a clamped-free beam was calculated first. Then, the bending moment spectral density at the root was used as the input to the skin-stringer panel. These results indicate that when the natural frequency of the beam coincides with one of the natural frequencies of the stiffened panel, a large amount of noise can be generated inside the enclosure. To minimize this, the modal frequencies of the substructure should not have values which are close to modal frequencies of the noise transmitting sidewall.

A direct comparison of the results of the cases of a coupled problem and under special conditions where the inputs to the stiffened panel are the bending moments of a clamped-free beam is given in Fig. 60. The sound pressure levels of the coupled problem are lower at most frequencies. These results clearly illustrate the significance of a complete solution when the elastic coupling between the substructure and stiffened panel is included.

4.2.5 Noise Transmission - A Parametric Study

Parametric studies of noise transmission were performed for the acoustic enclosure shown in Fig. 46. The inputs to the panels or partitions are random point forces characterized by an idealized spectral density shown in Fig. 61. This spectral density is composed of low level wide band noise and periodic tones with a fundamental tone at 60 Hz. These types of excitations are often produced from operations of electrical and mechanical devices such as fans, compressors, turbines, rotating and reciprocating tools, etc. Structural damping of the panels, acoustic damping and acoustic absorption in the interior are taken to be the same as in Sec. 4.2.4. Interior noise levels are calculated at x = 42 in., y = 210 in. and z = 30 in. (middle of the enclosure).

The narrow band sound pressure levels are given in Fig. 62. The overall and the overall A-weighted levels are also indicated in this figure. Similar results are shown in Fig. 63

where the sound pressure levels are plotted on the one-third octave scale. The results given in Figs. 62 and 63 correspond to vibrating stiffened panels located at z = 0, x = 32 in. and y = 198 in. The panel dimensions are $y_1 = y_2 = y_3 = 8.2$ in., $L_x = 20$ in. and $L_y = 24.6$ in. It is assumed that noise is generated only by this panel. As can be observed from these results, strong peaks are observed at frequencies where the tone inputs coincide with structural and/or acoustic resonance frequencies. Interior noise is dominated by a peak at 500 Hz. The results shown in Figs. 64 and 65 are for the same conditions as in Figs. 63 and 64 but the vibrating panel is located at z = 0, x = 10 in. and y = 10 in. Similar results are given in Figs. 66 and 67 for z = 0, x = 32 in., y = 10 in., and in Figs. 68 and 69 for z = 20 in., x = 84 in. and y = 198 in. As can be observed from these results, the spatial location of the vibrating source could have a significant effect on interior noise levels.

The results presented in Figs. 70 and 71 are for an enclosure separated by a partition at y = 140 in. (Fig. 46). Noise is generated by a vibrating panel located at z = 42.3 in, x = 32 in., and y = 0 (left end of enclosure). Sound pressure levels are calculated at x = 30 in., y = 42 in. and z = 20 in. A direct comparison of these results with the results presented in Figs. 62-69 indicate that many more acoustic modes are excited in a smaller enclosure.

To illustrate the effect on interior noise by vibrating stiffened panels of different sizes, noise transmission calculations were obtained for a variety of panel sizes. All these panels were located at $z = 0$, $x = 32$ in. and $y = 198$ in. for the enclosure shown in Fig. 46. Noise is calculated at the middle of the interior space. The one-third octave sound pressure levels for several vibrating panel sizes are given in Figs. 72-74. These results indicate that the size of the vibrating surface could have a significant effect on the levels of interior noise. However, there seems no strong indication that a larger panel would produce more noise. Interior noise is controlled by coincidences of tone frequencies and modal frequencies of the stiffened panels.

Noise generated by a large unstiffened panel with dimensions $L_x = 20$ in., $L_y = 16.4$ in. is given in Figs 75 and 76. Inputs are two point forces acting on the panel as shown in Fig. 75. Since the panel fundamental frequency is at about 35 Hz, large peak is seen at this frequency. Similar results are shown in Figs. 77 and 78 for the same geometric and input conditions but the panel is stiffened with stringers at the boundaries and at the middle of the panel. The effects of stiffening are lower noise levels in the frequency region of 0 - 300 Hz.

5.0 CONCLUSIONS

Analytical models were developed to predict vibration response and noise transmission of cylindrical and rectangular enclosures to random point inputs. These enclosures are intended to represent the exterior and interior geometries of the habitability modules of the space station design. The main emphasis of this study was on performing various parametric studies of structureborne noise generation and transmission. Numerical results are presented for several possible input conditions that might arise during prolonged orbital operations. When the actual input conditions are known, the results presented in this report can be scaled to these conditions. The intent of this work is to give preliminary guidelines for constructing analytical models and evaluating vibration and noise levels.

Results indicate that the shell response is strongly dependent on damping characteristics of the shell material and the core, location of the point load action, and reinforcing fiber orientation of the different laminae. In general, the response levels for a composite double wall shell are lower at most frequencies than those of an equivalent aluminum shell. The vibration response of the end caps (circular plates) are predominantly low frequency with the largest peak occurring at the fundamental mode.

The interior noise in a cylindrical enclosure is strongly dependent on damping characteristics of the shell and the core, location of the point load action, fiber orientation of the different laminae and wall absorption of the interior walls. A fiber reinforced composite double wall shell tends to generate more noise than an equivalent aluminum shell. This is due to the fact that the mass of the composite shell is about one half of the mass of the aluminum shell and increase of the modal frequencies of the stiffer composite shell could induce different coupling of the structural-acoustic modes. The noise transmitted by the end caps is predominantly low frequency. Thus, neglecting noise transmitted by the end caps could underestimate interior sound pressure levels for the low frequency region. Furthermore, by a proper selection of structural damping, reinforcing fiber orientation, acoustic absorption and core stiffness, a significant amount of lower response and higher noise attenuation can be achieved by a design consisting of double wall laminated fiber reinforced composite shells and a soft viscoelastic core.

The response and noise transmission characteristics of a shell stiffened with rings and stiffeners is strongly dependent on the type and the number of stiffening rings. Presence of small longitudinal stiffeners do not seem to have much effect on noise transmission. Furthermore, the location of point input forces could have a significant effect on generated noise levels in the cylindrical interior.

Transfer matrix procedures were developed to study the dynamic response, noise generation and transmission of stiffened and interconnected structures to random loads. It has been demonstrated that the formulation can be applied to a variety of discretely stiffened structures. In addition, it has been shown that structural response and transmitted noise levels in the interior are sensitive to the dynamic characteristics not only of the stiffened sidewall but also of the substructure to which random loads are applied. Significant differences were found in the structural response and noise transmission characteristics of different types of matching boundary conditions at the points of structural interconnection between the substructure and the stiffened sidewall, i.e., between a completely coupled case and an idealized condition where the response of the substructure is computed independently from the response of the noise transmitting sidewall. The results indicate that by tailoring the geometric and material characteristics of structural subcomponents, the vibration levels and noise transmission can be reduced.

Noise generated by vibration of various interior panels and/or partitions is sensitive to geometric conditions of the interior, panel sizes, location of the vibrating panels and types of inputs. No simple rules seem to exist in relating these conditions to the levels of interior noise. The coincidence of structural resonance frequencies with one of the input tones could result in high interior noise levels. For broad bond input types, increase in structural damping and interior acoustic absorption seem to be the most effective means for noise control. An alternative procedure would be to isolate the vibrating equipment so that force inputs to the panels are reduced. The results presented in this study demonstrate that a relatively small amount of vibrational energy is needed to produce relatively high structureborne noise levels.

6.0 REFERENCES

1. National Aeronautics and Space Adminstration, "Guidelines for Noise and Vibration Levels for the Space Station," NASA CR-178310, June 1987.

2. National Aeronautics and Space Administration Space Station Program, Description, Applications and Opportunity, Noyes Publications, 1984.

3. Baratono, J.R., Hellweg, R.D., Jr. and Rader, W.P., "Skylab Program Payload Integration," Technical Report under Contract NAS8-2400, February, 1972.

4. Eilers, D., Wyn-Roberts, D. and Borchers, I.U., "Audible Noise Control in Spacelab - As Part of Manned Spacecraft Environmental Control," Proceedings of Spacecraft Thermal and Environmental Control Systems Symposium, ESA SP-139, Munich, FGR, October, 1978.

5. Rader, W.P. Baratono, J., Bandogen, H. and Erwin, R., "Noise in Space," 89th Acoustical Society of America Meeting, Austin, Texas, April, 1975.

6. Rader, W.P., "Acoustic and Vibration Environments for Laboratory Experiments in Space," NASA CP-2199.

7. Willshire, K.F., "Low Frequency Vibration Effects in Space Station," Journal of Acoustical Society of America, S1, Vol. 79, S87, 1986.

8. Vaicaitis, R. and Mixson, J.S., "Review of Research on Structureborne Noise," 26th AIAA/ASME/ASCE/AHS SDM Conference, Paper No. 85-0786-CP, Orlando, FL, April, 1985.

9. Cockburn, J.A. and Jolly, A.C., "Structural Acoustic Response, Noise Transmission Losses, and Interior Noise Levels of an Aircraft Fuselage Excited by Random Pressure Fields," AFFDC-TR-682 Air Force Flight Dynamics Laboratory, Wright Patterson Air Force Base, Ohio, August 1968.

10. Mikulas, M.M. and McElman, J.A., "On Free Vibration of Eccentrically Stiffened Cylindrical Shells and Flat Plates," NASA TN D-3010, 1965.

11. Weingarten, V.I., "Free Vibration of Thin Cylindrical Shells," Vol. 2, No. 4, April 1964, pp. 717-721.

12. Yu, Y.-Y., "Free Vibrations of Thin Cylindrical Shells Having Finite Lengths with Freely Supported and Clamped Edges," Transactions of the ASME, Journal of Applied Mechanics, Vol. 77, 1955, pp. 547-552.

13. Forsberg, K., "Influence of Boundary Conditions on the Modal Response of Thin Cylindrical Shells," AIAA Journal, Vol. 2, No. 12, Dec. 1964, pp. 2150-2157.

14. Arnold, R.N. and Warburton, G.B., "The Flexural Vibrations of Thin Cylinders," Proceedings of the Insitution of Mechanical Engineers," Vol. 167, 1953, pp. 62-74.

15. Warburton, G.B., "Vibration of Thin Cylindrical Shells," Mechanical Engineering Science Journal, Vol. 7, No. 4, 1965, pp. 399-407.

16. Leissa, A.W. and Iyer, K.M., "Modal Response of Circular Cylindrical Shells with Structural Damping," Journal of Sound and Vibration, Vol. 77, No. 1, 1981, pp. 1-10.

17. Kunukkasseril, V.X. and Swamidas, A.S.J., "Normal Modes of Elastically Connected Circular Plates," Journal of Sound and Vibration, Vol. 30, No. 1, 1973, pp. 99-108.

18. Chonan, S., "The Free Vibrations of Elastically Connected Circular Plate Systems with Elastically Restrained Edges and Radial Tensions," Journal of Sound and Vibration, Vol. 49, No. 1, 1976, pp. 129-136.

19. Schlak, A.L., Jr., Kessel, W.N. and Dong, W.N., "Dynamic Response of Elastically Supported Circular Plates to a General Surface Load," AIAA Journal, Vol. 10, No. 6, June 1972, pp. 733-738.

20. Reismann, H., "Forced Vibrations of a Circular Plate," Journal of Applied Mechanics, Vol. 26, 1959, pp. 526-527.

21. Wah, T., "Vibration of Circular Plates," Journal of the Acoustical Society of America, Vol. 34, No. 3, 1962, pp. 275-281.

22. Anderson, G., "On the Determination of Finite Integral Transforms for Forced Vibrations of Circular Plates," Journal of Sound and Vibration, Vol. 9, 1969, pp. 126-144.

23. Weiner, R.S., "Forced Axisymmetric Motions of Circular Elastic Plates," Journal of Applied Mechanics, Vol. 4, 1965, pp. 893-989.

24. Leissa, A.W. and Narita, Y., "Natural Frequencies of Simply Supported Circular Plates,"Journal of Sound and Vibration, Vol. 70, No. 2, 1980, pp. 221-229.

25. Bert, C.W. and Eagle, M.D., "Dynamics of Composite, Sandwich, and Stiffened Shell-Type Structures," Journal of Spacecraft and Rockets, Vol. 6, No. 12, Dec. 1969, pp. 1345-1361.

26. Soedel, W., Vibrations of Shells and Plates, Marcel Dekker, Inc., 1981.

27. Keffe, R.E. and Windholz, W.M., "Dynamic Analysis of Multilayered Cylinder," AIAA Paper 68-350, Palm Springs, California, 1968.

28. Dong, R.M., Pister, K.S. and Taylor, R.L., "On the Theory of Laminated Anisotropic Shells and Plates," Journal of Aerospace Sciences, Vol. 29, No. 8, Aug. 1962, pp. 969-975.

29. Bert, C.W., "Structural Theory for Laminated Anisotropic Shells," Journal of Composite Materials, Vol. 1, No. 4, Oct. 1967, pp. 414-423.

30. Bert, C.W., Baker, J.L. and Eagle, D.M., "Free Vibrations of Multilayered Anisotropic Cylindrical Shells," Journal of Composite Materials, Vol. 3, No. 4, July 1969, pp. 480-499.

31. Vaicaitis, R. and Bofilios, D.A., "Vibro-Acoustics for Space Station Applications," AIAA-86-1937, AIAA 10th Aeroacoustics Conference, Seattle, Washington, July 9-11, 1986.

32. Bofilios, D.A. and Vaicaitis, R., "Response of Double-Wall Composite Shells to Random Point Loads," AIAA Journal of Aircraft, Vol. 24, No. 4, April 1987.

33. Vaicaitis, R. and Lyrintzis, C.S., "Response of Discretely Stiffened Structures," AIAA/ASME/ASCE/AHS 28th Structures Structural Dynamics and Materials Conference, Paper No. 87-0914, Monterey, CA, April 6-8, 1987.

34. Vaicaitis, R. Lyrintzis, C.S., "Structure-borne Noise Generation and Transmission," U.S. - Austria Joint Seminar on Stochastic Structural Mechanics, Florida Atlantic University, Boca Raton, FL, May 4-5, 1987.

35. Vaicatis, R. and Lyrintzis, C.S., "Structure-borne Noise Transmission in Stiffened Structures," AIAA 11th Aeroacoustics Conference," Paper No. 87-2679, Sunnyvale, CA, Oct. 19-21, 1987.

36. Pestel, E.C. and Leckie, F.A., Matrix Methods in Elastomechanics, McGraw-Hill, New York.

37. Lin, Y.K. and Donaldson, B.K., "A Brief Survey of Transfer Matrix Techniques with Special Reference to Aircraft Panels," Journal of Sound and Vibration, Vol. 10(1), 1969, pp. 103-143.

38. Vaicatis, R. and Slazak, M., "Noise Transmission Through Stiffened Panels," Jounal of Sound and Vibration, Vol. 70(3), 1980, pp. 413-426.

39. Rand, R.H., "Computer Algebra in Applied Mathematics: An Introduction to MACSYMA," Pitman Advanced Publishiing Program, 1984.

40. Baranek, L.L., Noise and Vibration Control, McGraw-Hill, New York, 1971.

41. Vaicaitis, R. and Bofilios, D.A., "Noise Transmission of Double Wall Composite Shells," ASME, The 10th Biennial Conference on Mechanical Vibrations and Noise, Cincinnati, Ohio, Sept. 10-13, 1985.

42. Bofilios, D.A., "Response and Structure-borne Noise Transmission of Laminated Cylindrical Shells," Ph.D. Thesis, Columbia University, New York, NY, 1985.

43. Lyrintzis, C.S., "Response of Discretely Stiffened Structures and Transmission of Structure-borne Noise," Ph.D. Thesis, Columbia University, New York, NY, 1987.

44. Dong., S.B., "Free Vibration of Laminated Orthotropic Cylindrical Shells," Journal of the Acoustical Society of America, Vol. 44, No. 6, 1968.

45. Soedel, W., "Simplified Equations and Solutions for the Vibration of Orthotropic Cylindrical Shells," Journal of Sound and Vibration, 37(4), pp. 555-566, 1983.

46. Lin, Y.K., Probabilistic Theory of Structural Dynamics, McGraw-Hill, Inc., 1967.

47. Davis, G.W. and Sakata, I.F., "Design Considerations for Composite Fuselage Structure of Commercial Transport Aircraft," NASA CR-159296, March 1981.

48. Yang, J.C.S. and Tsui, C.Y., "Optimum Design of Structures and Composite Materials in Response to Aerodynamic Noise and Noise Transmission," NASA CR-155332, December 1977.

49. Durchlaub, E.C., "Minimized Fuselage Vibrations Using Advanced Composites," 33rd Annual Forum of the American Helicopter Society, Paper No. 77.33-84, Washington, DC, May 1977.

50. Koval, L.R., "Sound Transmission into a Laminated Composite Shell," Journal of Sound and Vibration, Vol. 71, 1980, pp. 523-530.

51. Bieniek, M.P. and Freudenthal, M.A., "Frequency Response Functions of Orthotropic Sandwich Plates," Journal of Aerospace Sciences, Vol. 28, No. 9, Sept. 1961.

52. Narayanan, S. and Shanbhag, R.L., "Acoustoelasticity of a Damped Sandwich Panel Backed by a Cavity," Journal of Sound and Vibration, Vol. 78, 1981, pp. 453-473.

53. Vaicaitis, R., "Noise Transmission by Viscoelastic Sandwich Panels," NASA-TND-8516, 1977.

54. Smolenski, C.P. and Krokosky, E.M., "Dilational Mode Transmission in Sandwich Panels," Journal of the Acoustical Society of America, Vol. 54, No. 6, 1973, pp. 1449-1457.

55. McLachlan, N.W., Bessel Functions for Engineers, 2nd ed., Clarendon Press, Oxford, England, 1955.

56. Kristek, V., Theory of Box Girders, John Wiley and Sons, New York, 1976.

57. Kuhn, P., Stresses in Aircraft and Shell Structures, McGraw-Hill, New York.

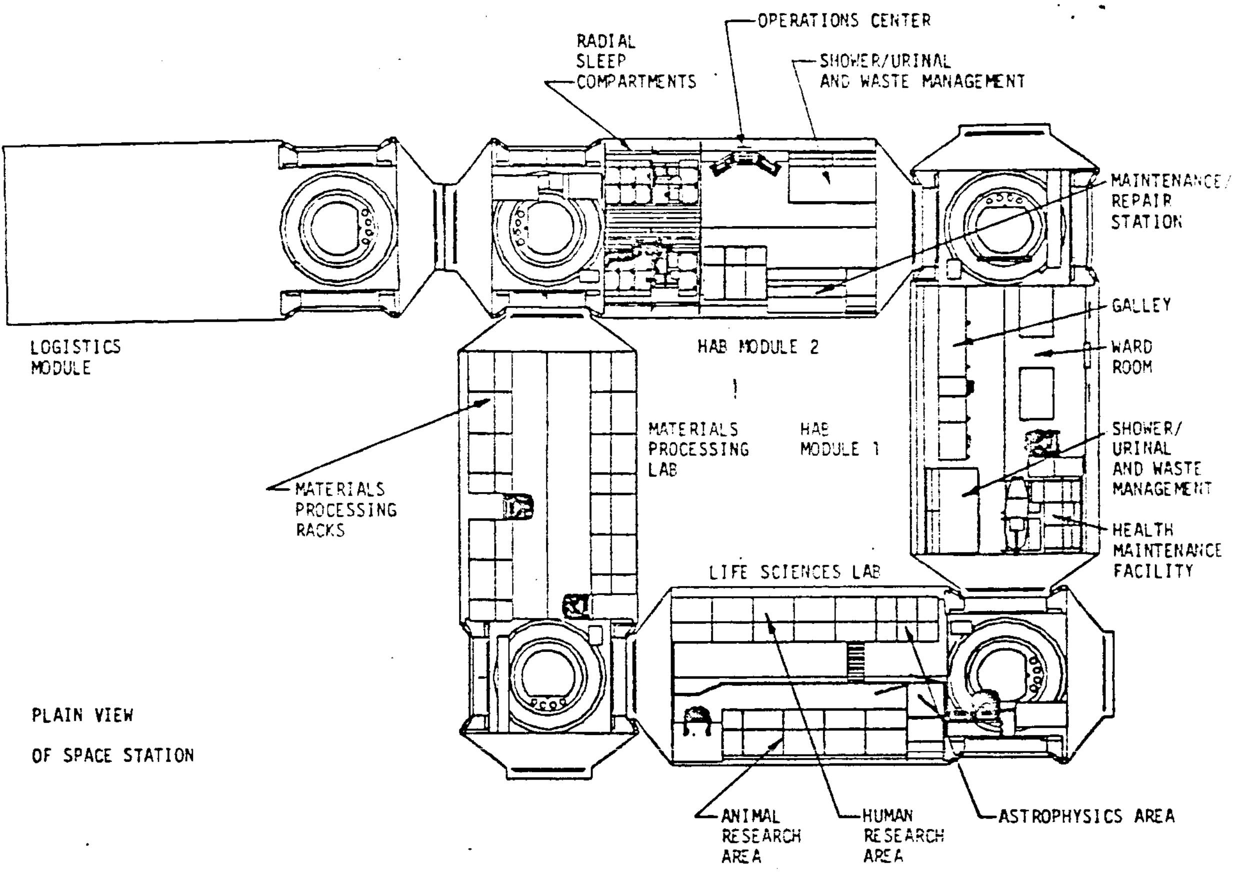

Fig. 1 Habitability modules of space station

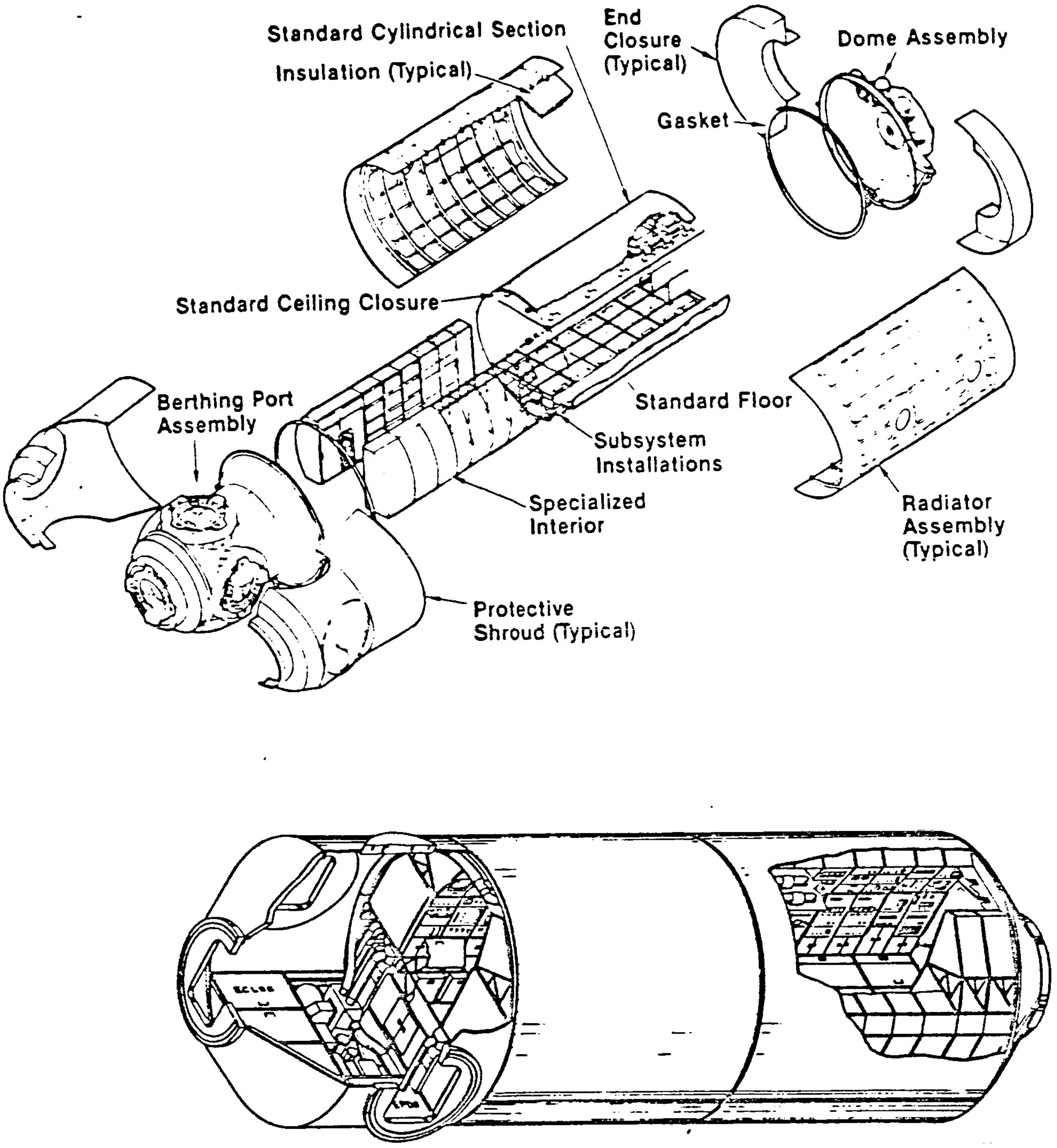

Fig. 2 Proposed geometry of habitability modules

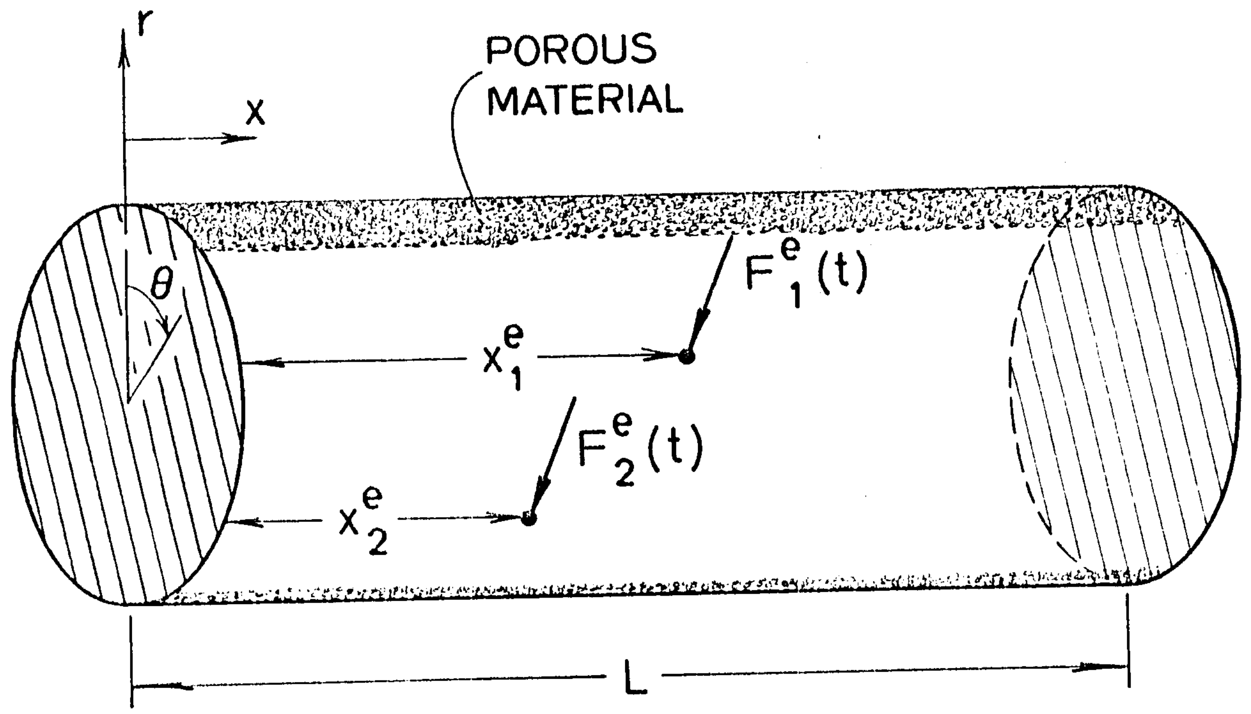

Fig. 3 Geometry of a cylindrical shell model

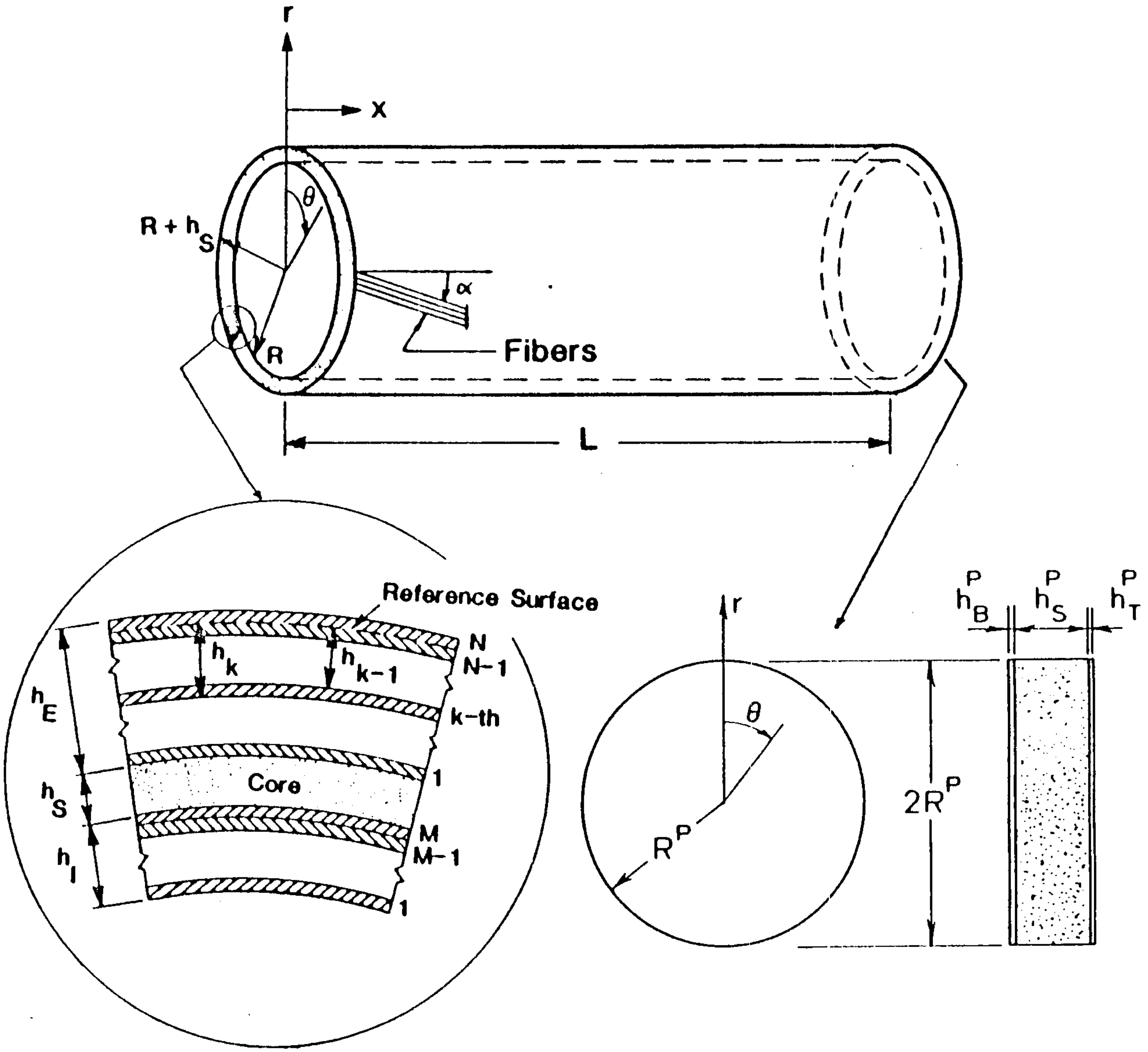

Fig. 4 Geometry of double wall composite shell

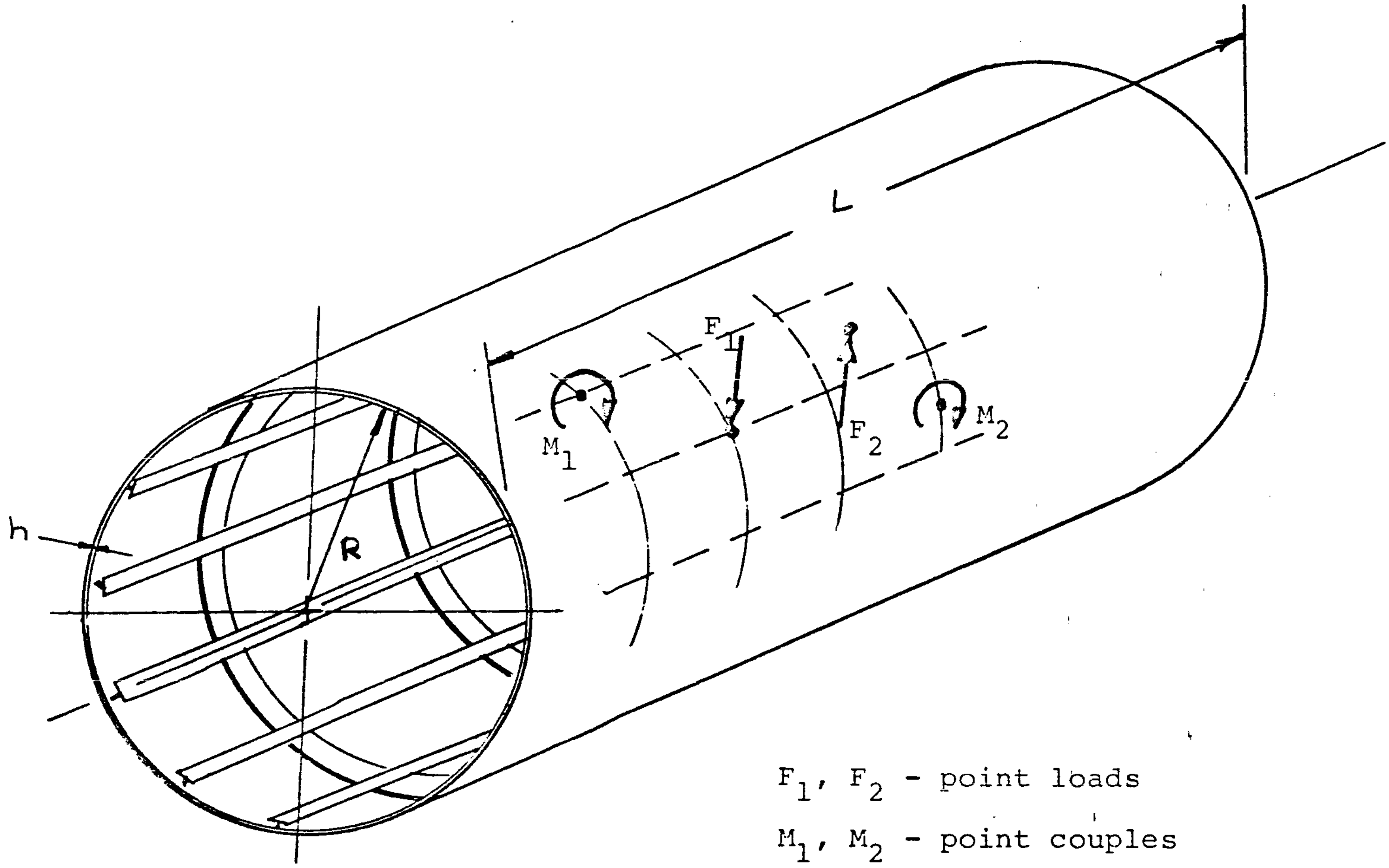

F_1, F_2 - point loads

M_1, M_2 - point couples

Fig. 5 Geometry of a stiffened cylindrical shell

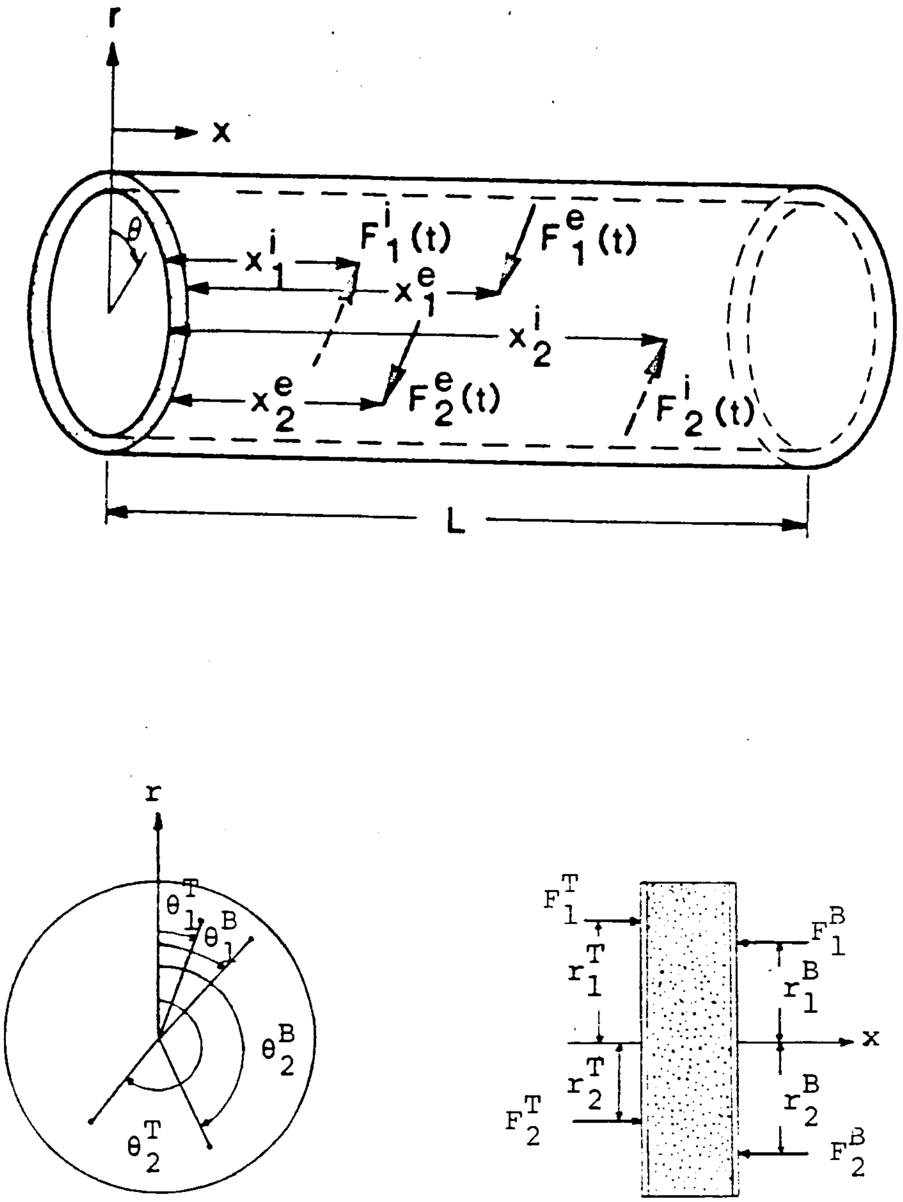

Fig. 6 Location of random point loads on the shell and plates

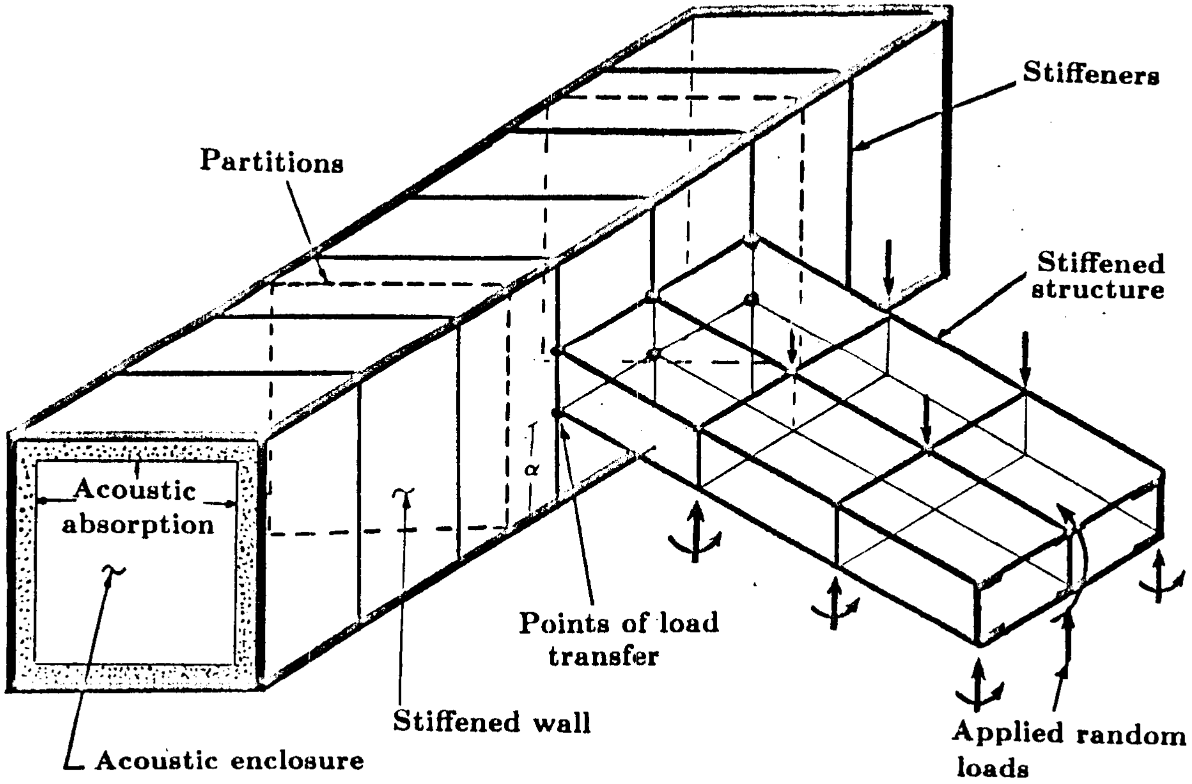

Fig. 7 *Geometry of an acoustic enclosure and a stiffened structure.*

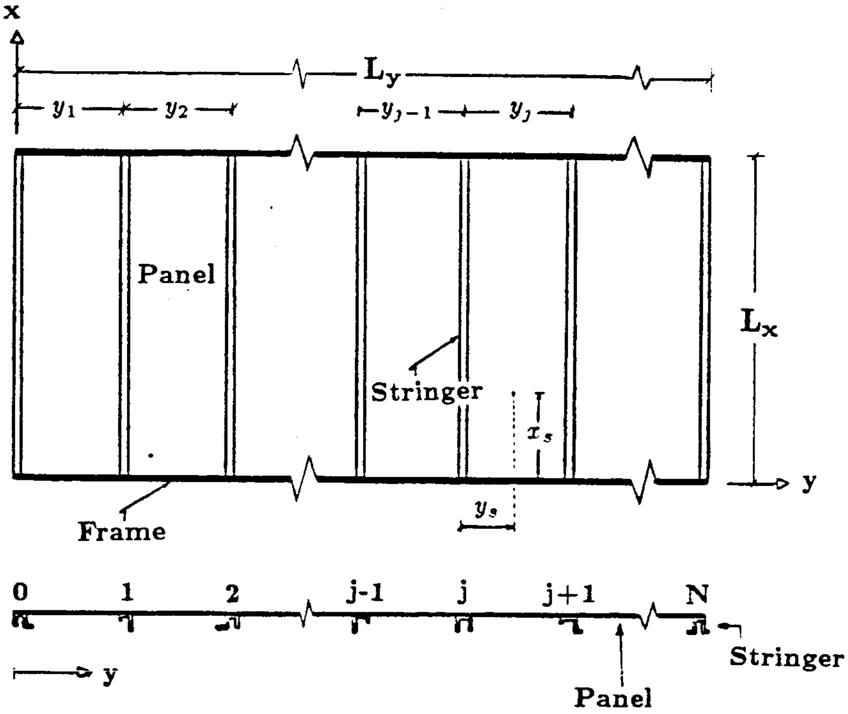

Fig. 8. *Stiffened multi-spaned panel array.*

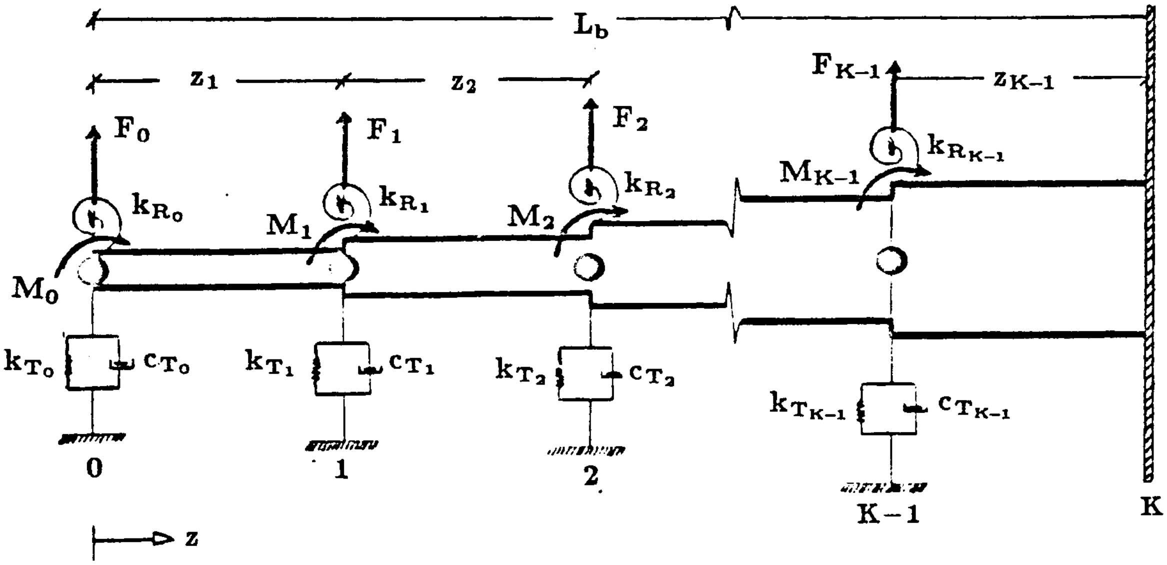

Fig. 9 *A piecewise continuous beam.*

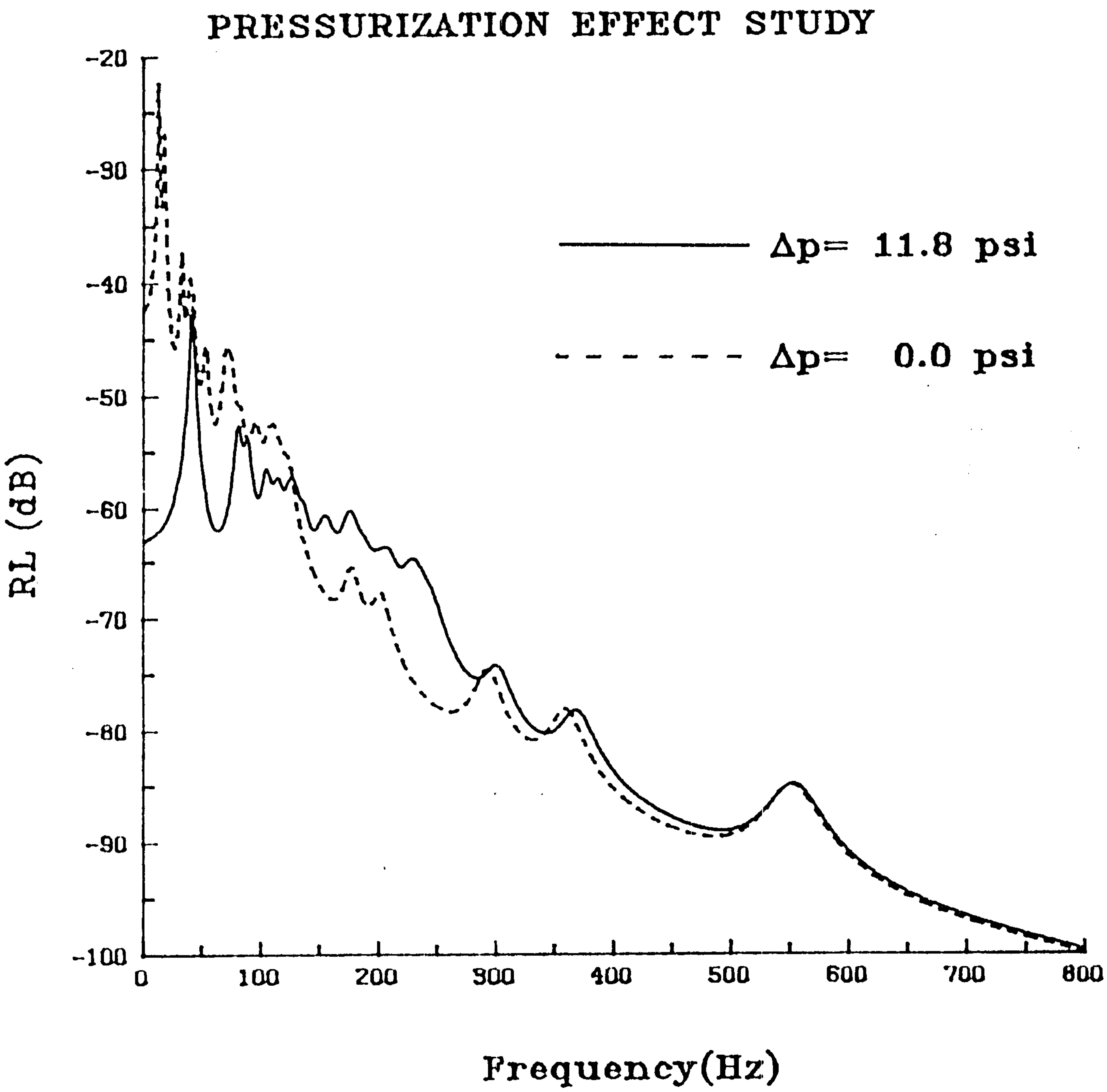

Fig. 10 Defelction levels for pressurized and unpressurized aluminum shells

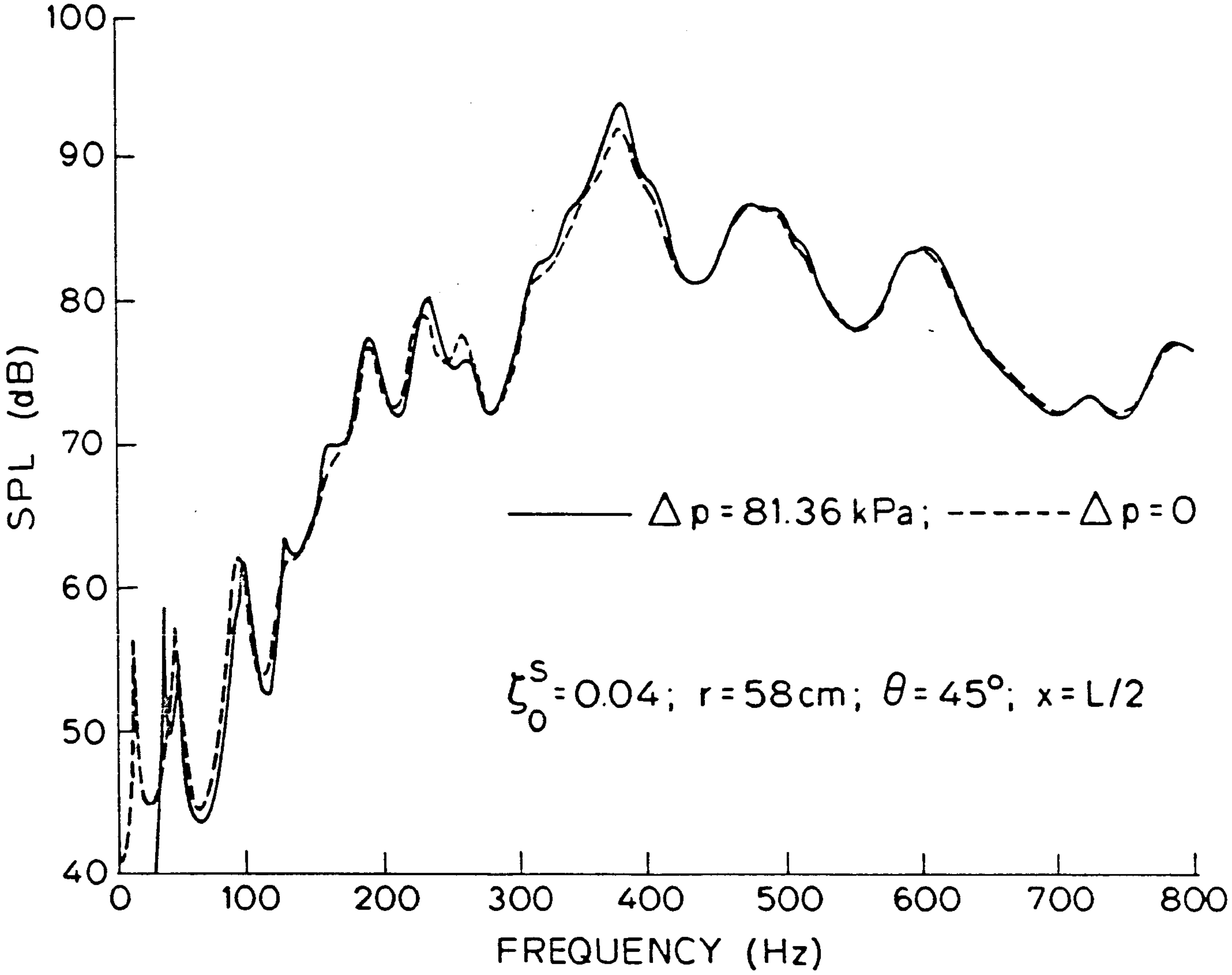

Fig. 11 Sound transmission into pressurized and unpressurized shells

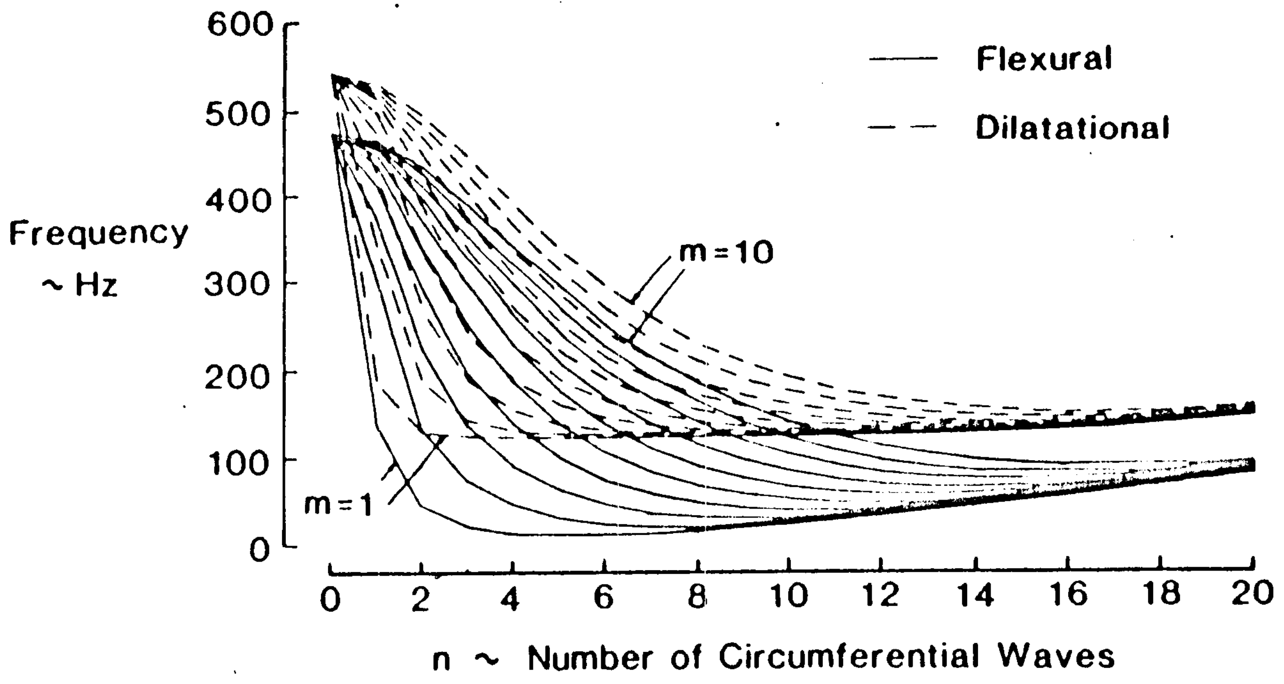

Fig. 12 Natural frequencies for double wall aluminum shell

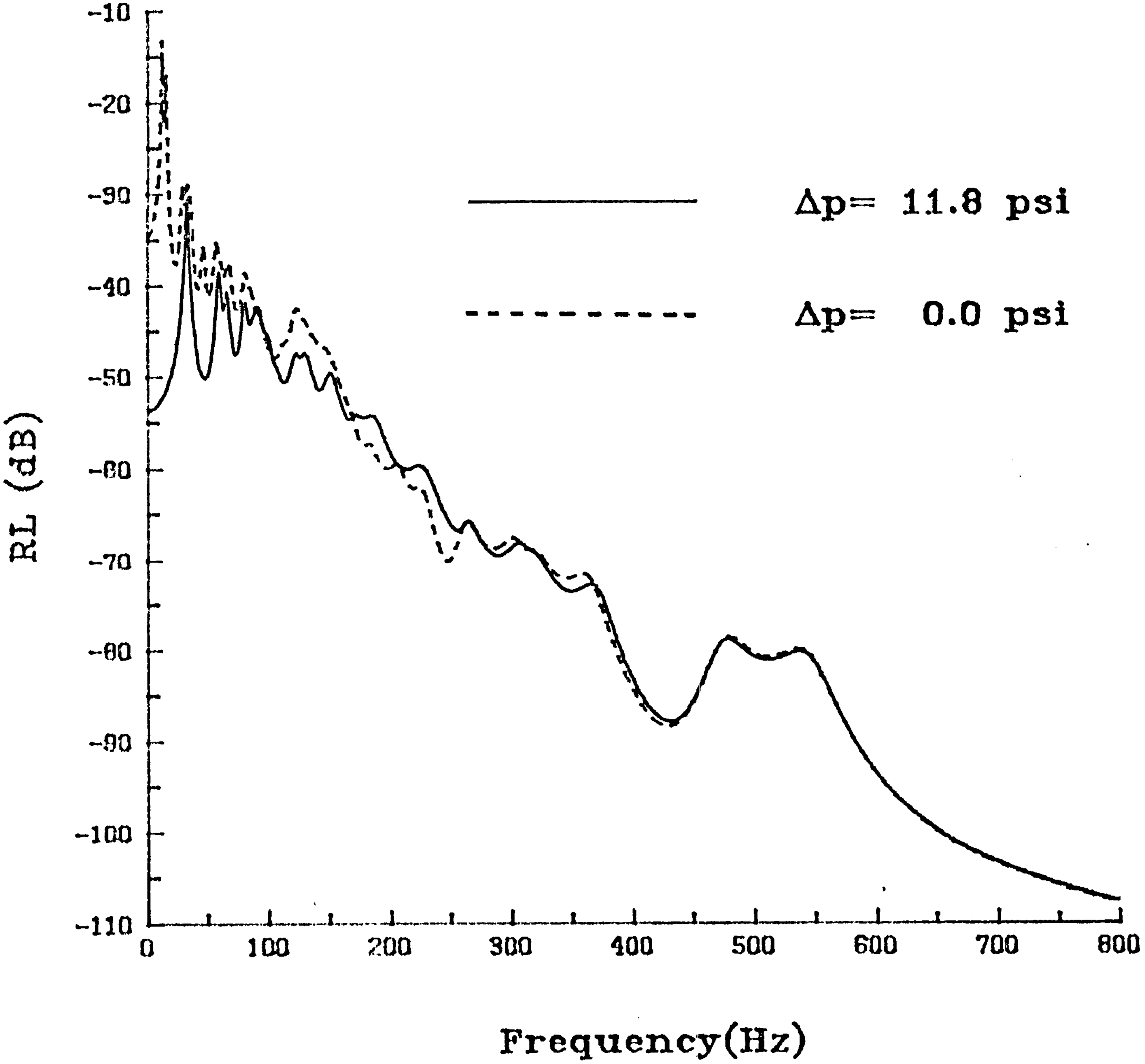

Fig. 13 Response of external shell (aluminum shell)

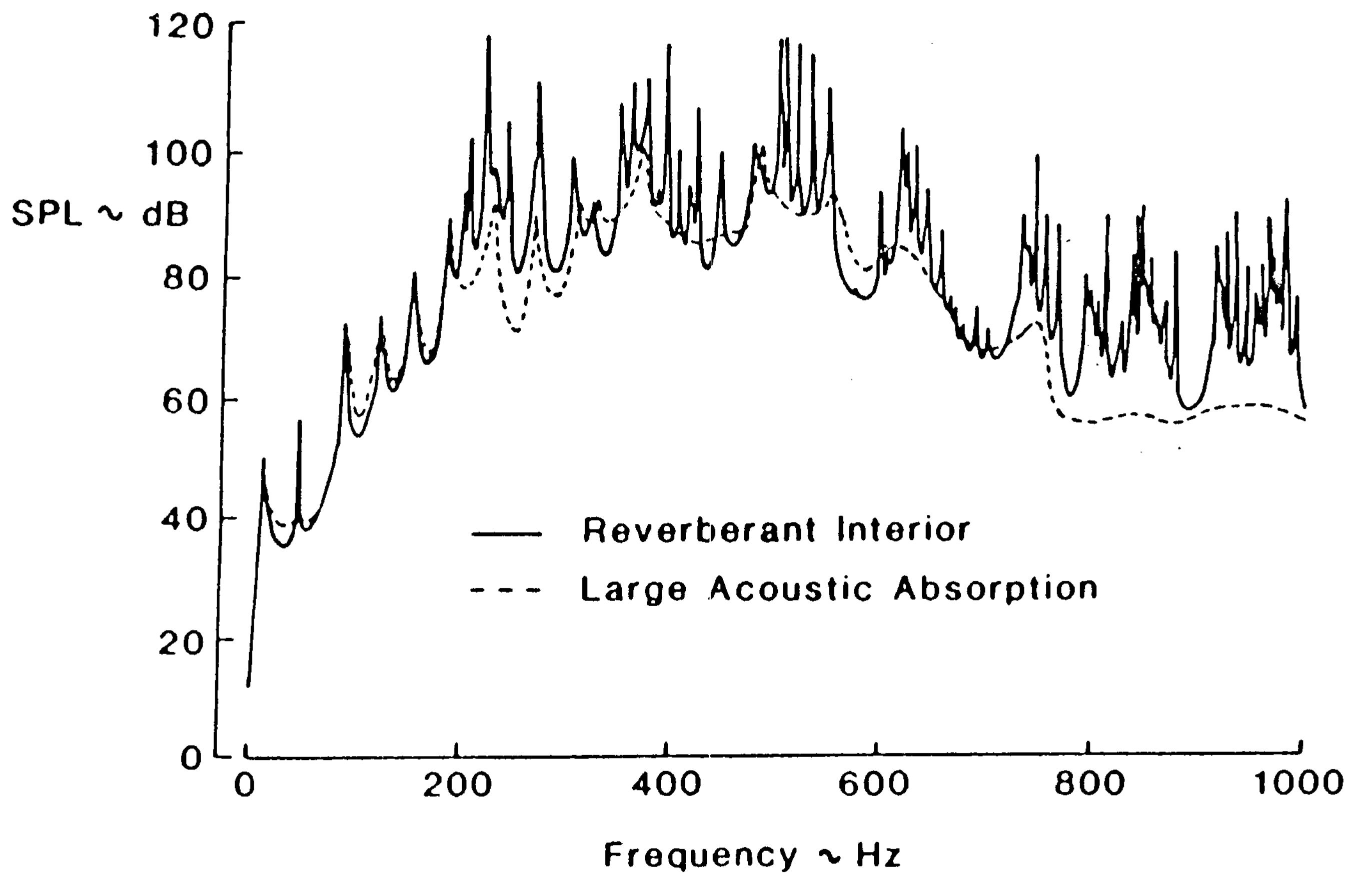

Fig. 14 Sound pressure levels of a double wall aluminum shell (exterior point loads)

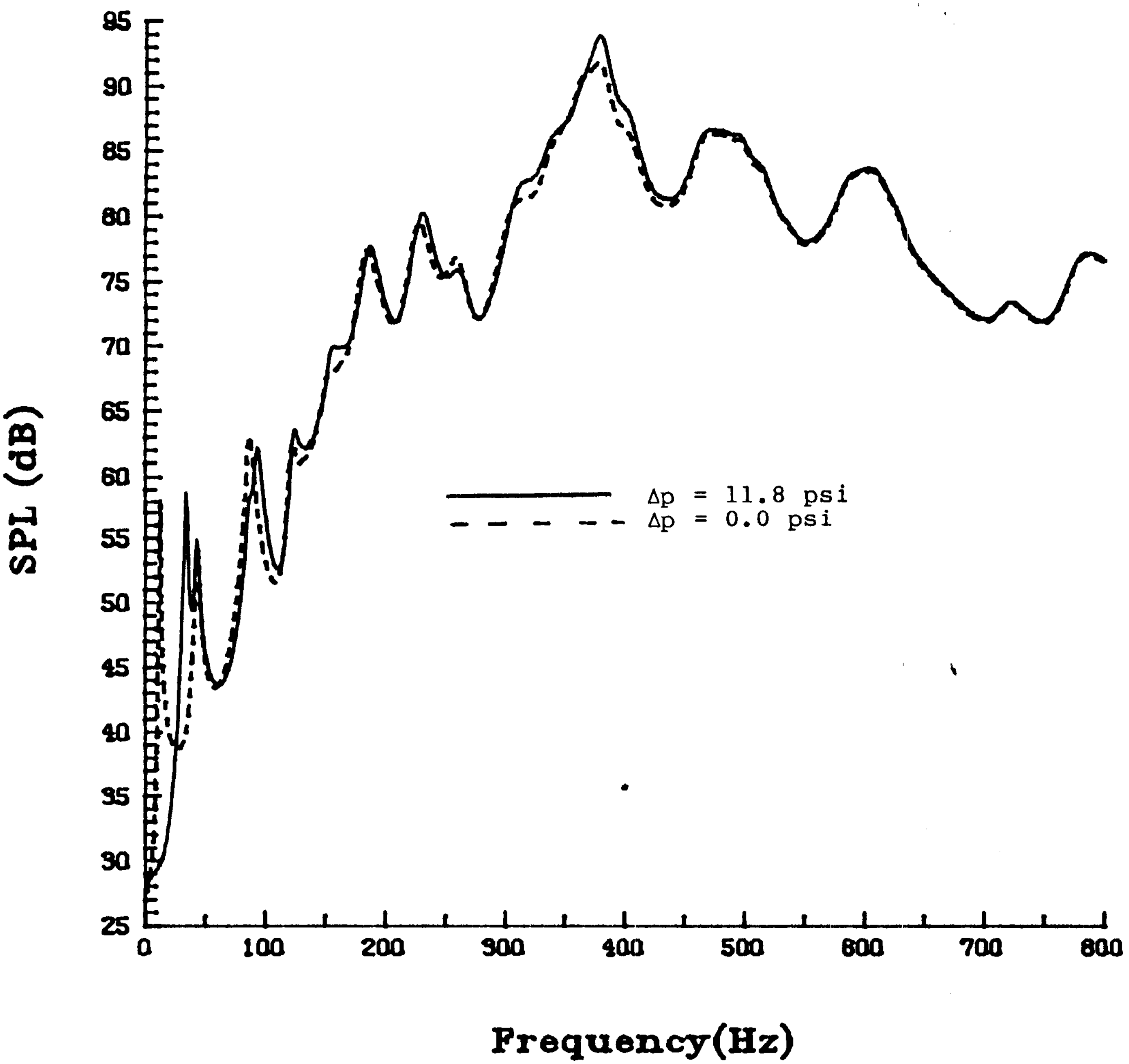

Fig. 15 Sound pressure levels in a pressurized and unpressurized double wall aluminum shell

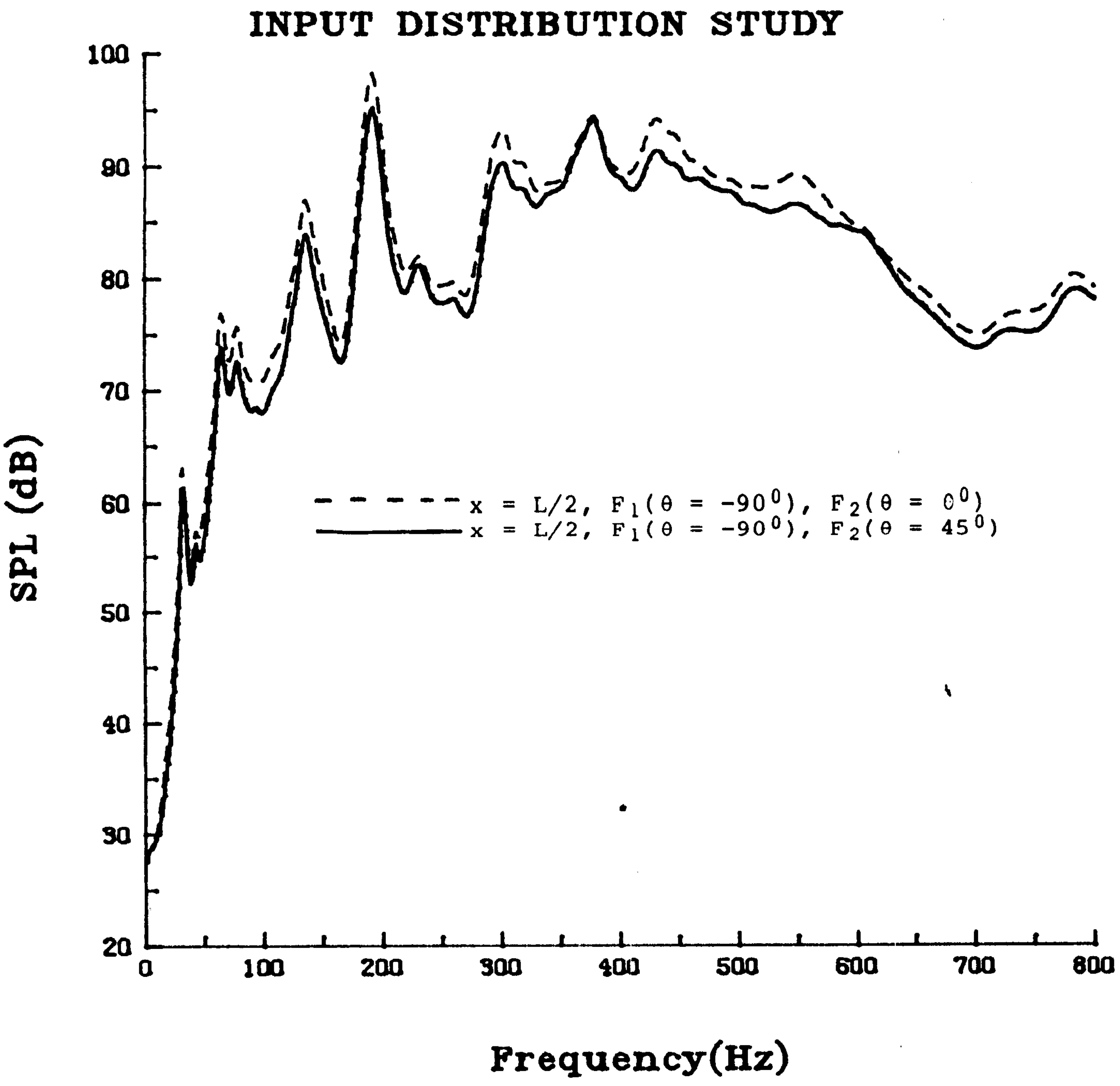

Fig. 16 Transmitted noise levels into a double wall aluminum shell for different input locations

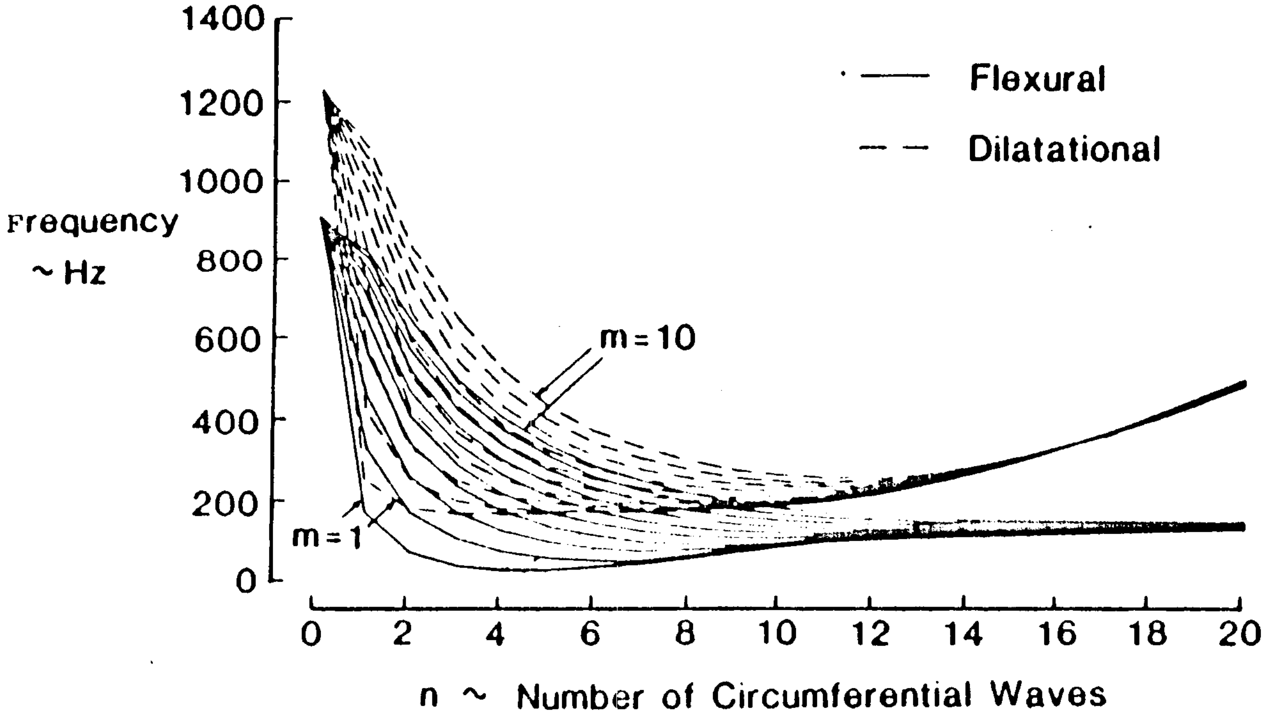

Fig. 17 Natural frequencies of double wall composite shell

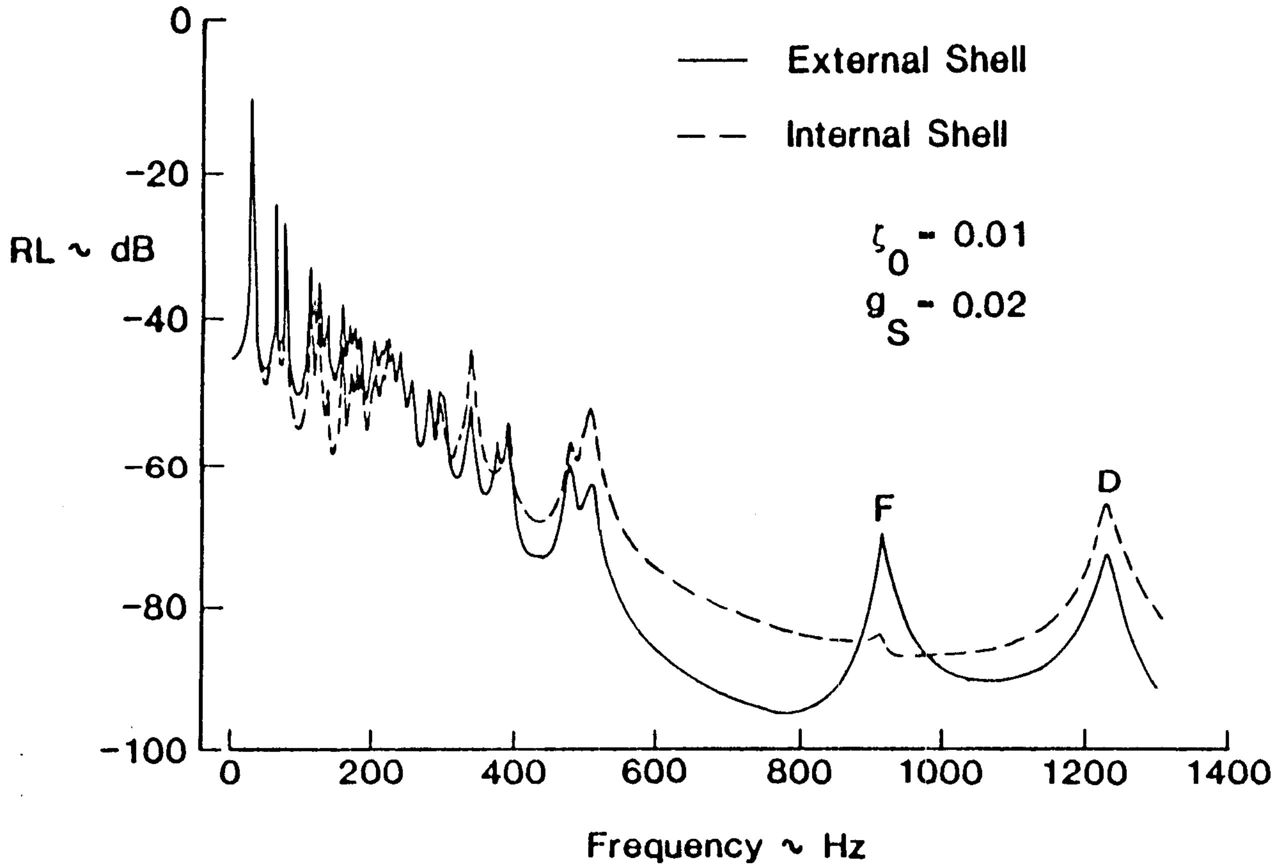

Fig. 18a Composite shell deflection levels for point loads acting on the interior surface

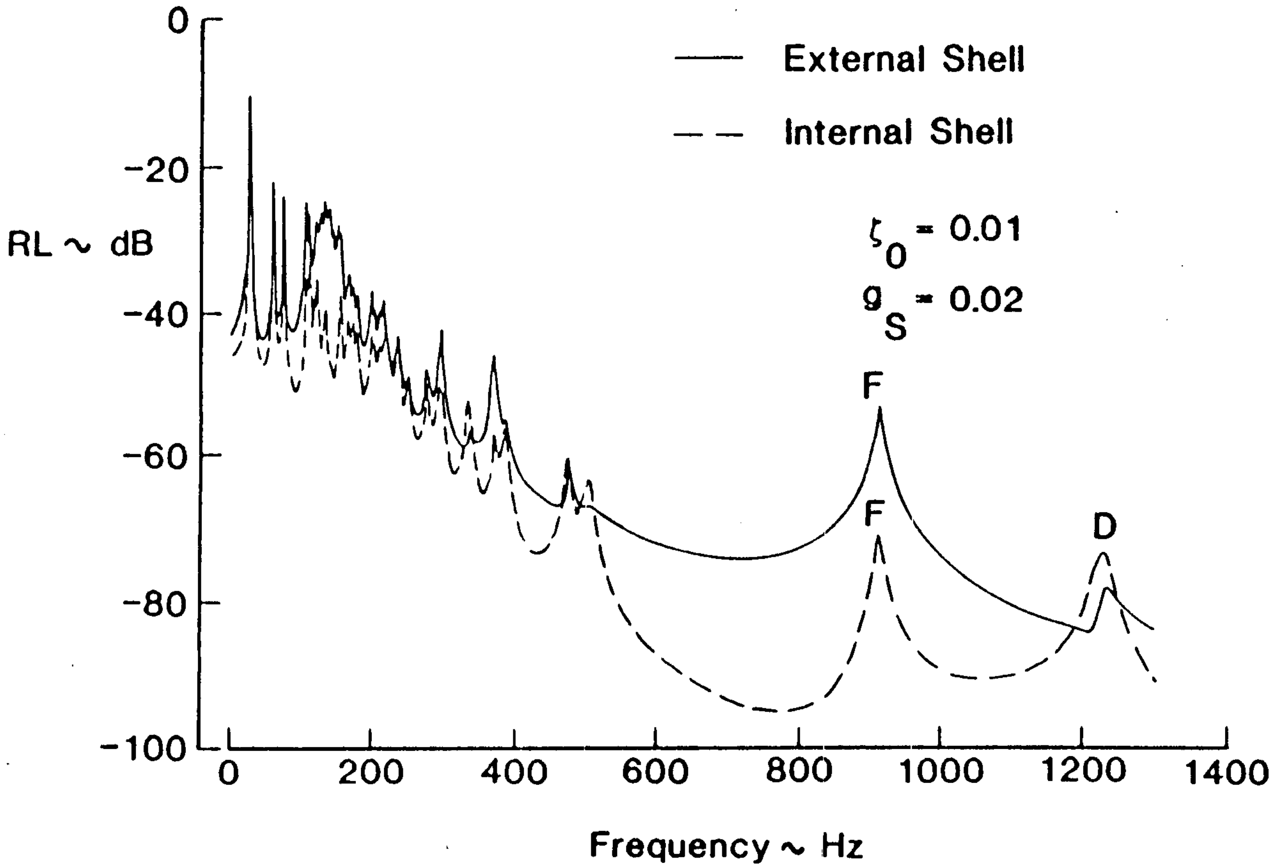

Fig. 18b Composite shell deflection levels for point loads acting on the exterior surface

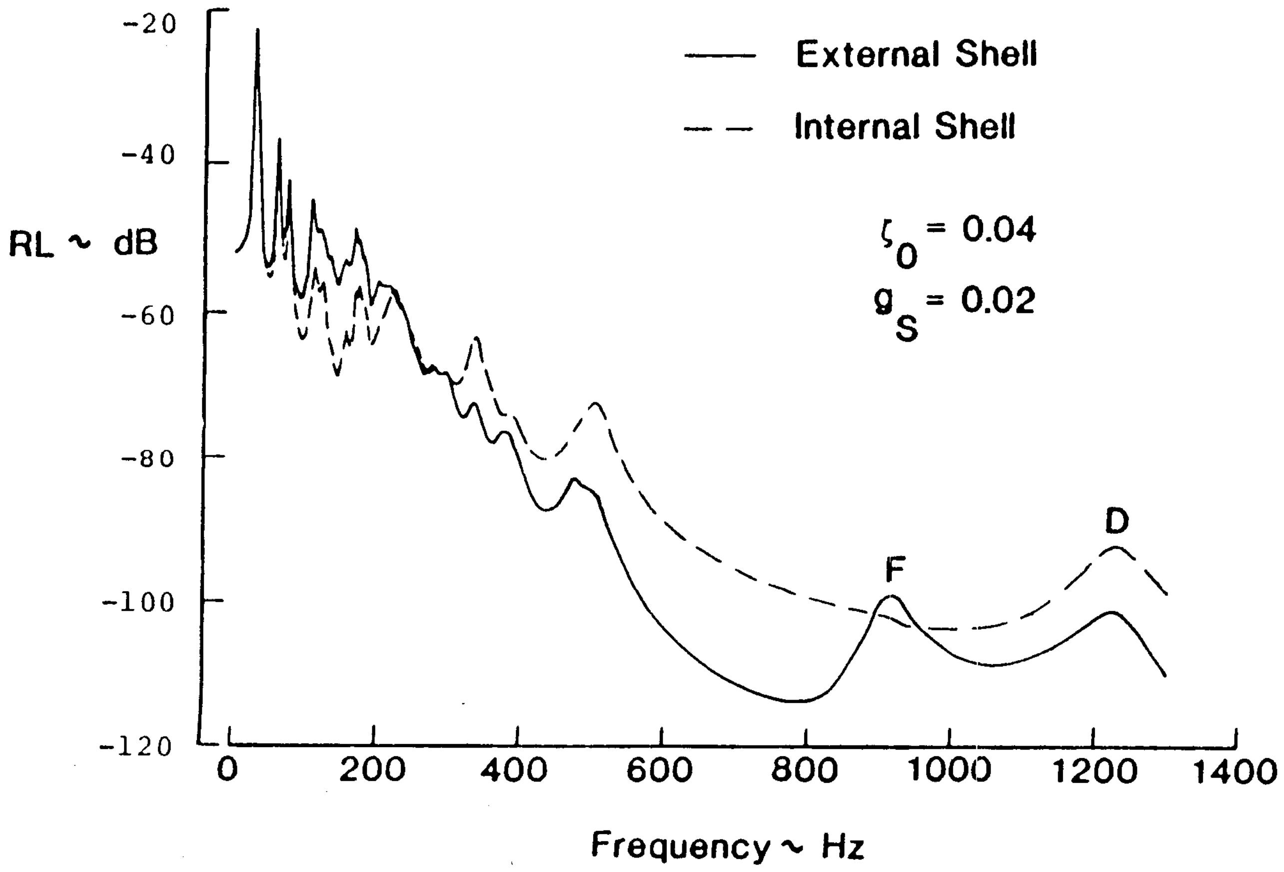

Fig. 19 Composite shell deflection levels for point loads acting on the interior surface

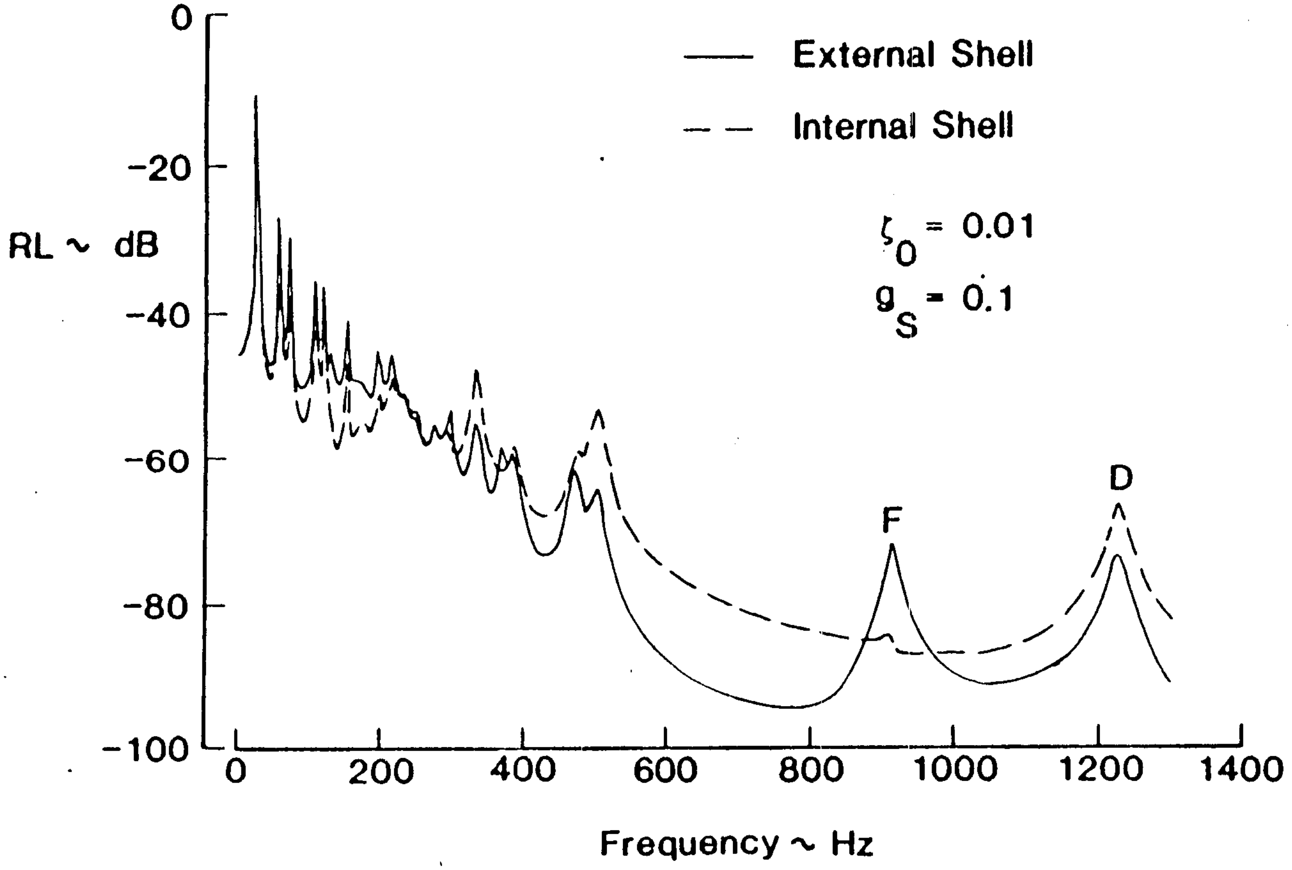

Fig. 20 Composite shell deflection levels for large core damping

C-2

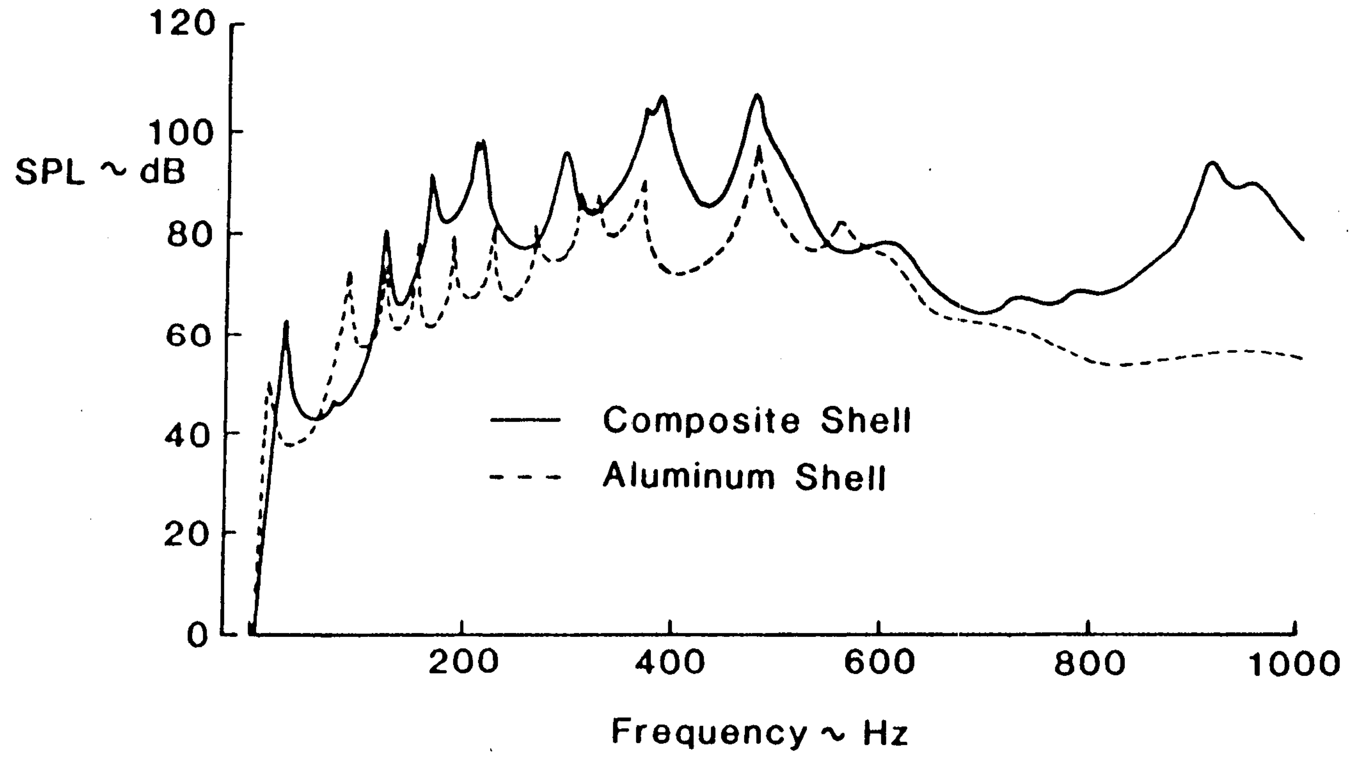

Fig. 21 Sound pressure levels for aluminum and composite shells (exterior point loads)

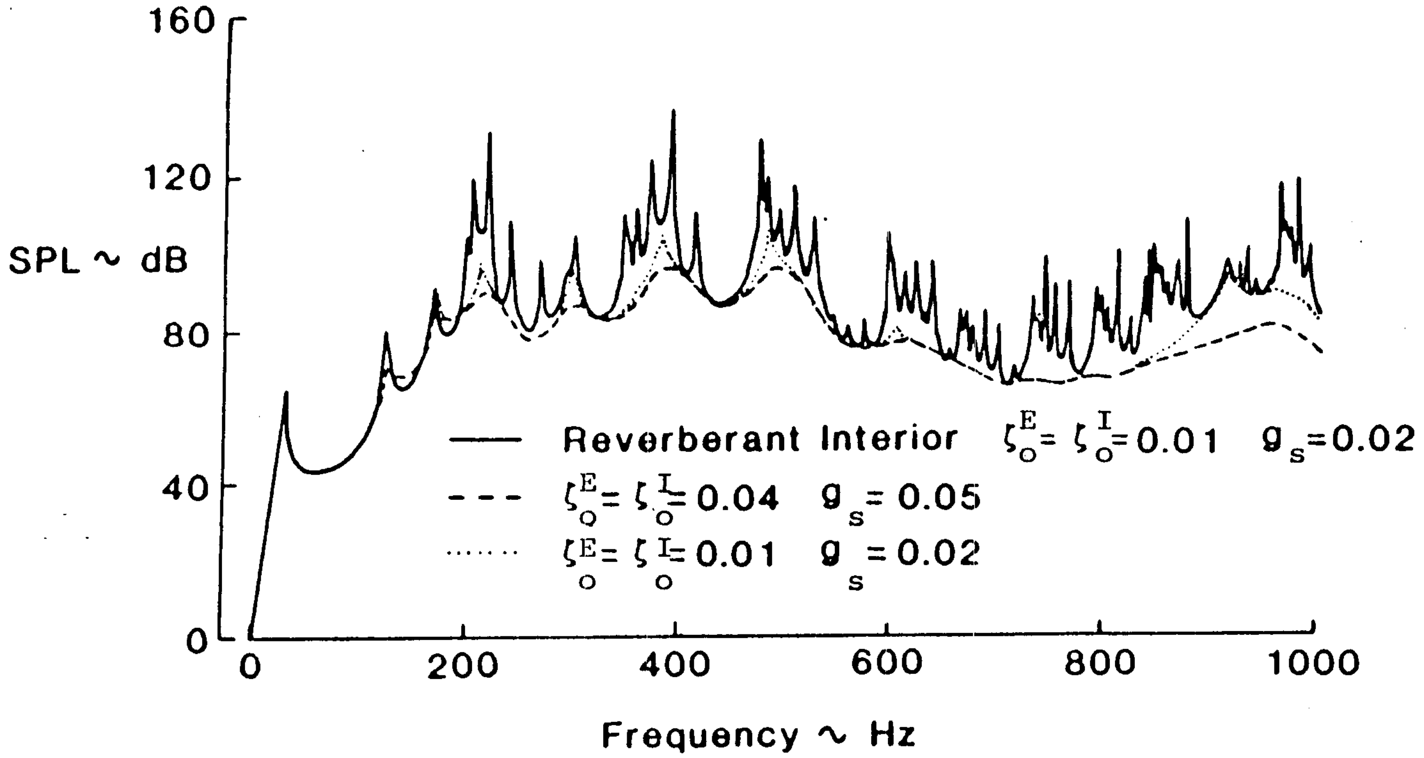

Fig. 22 Sound pressure levels for different structural and acoustic damping conditions (exterior point loads)

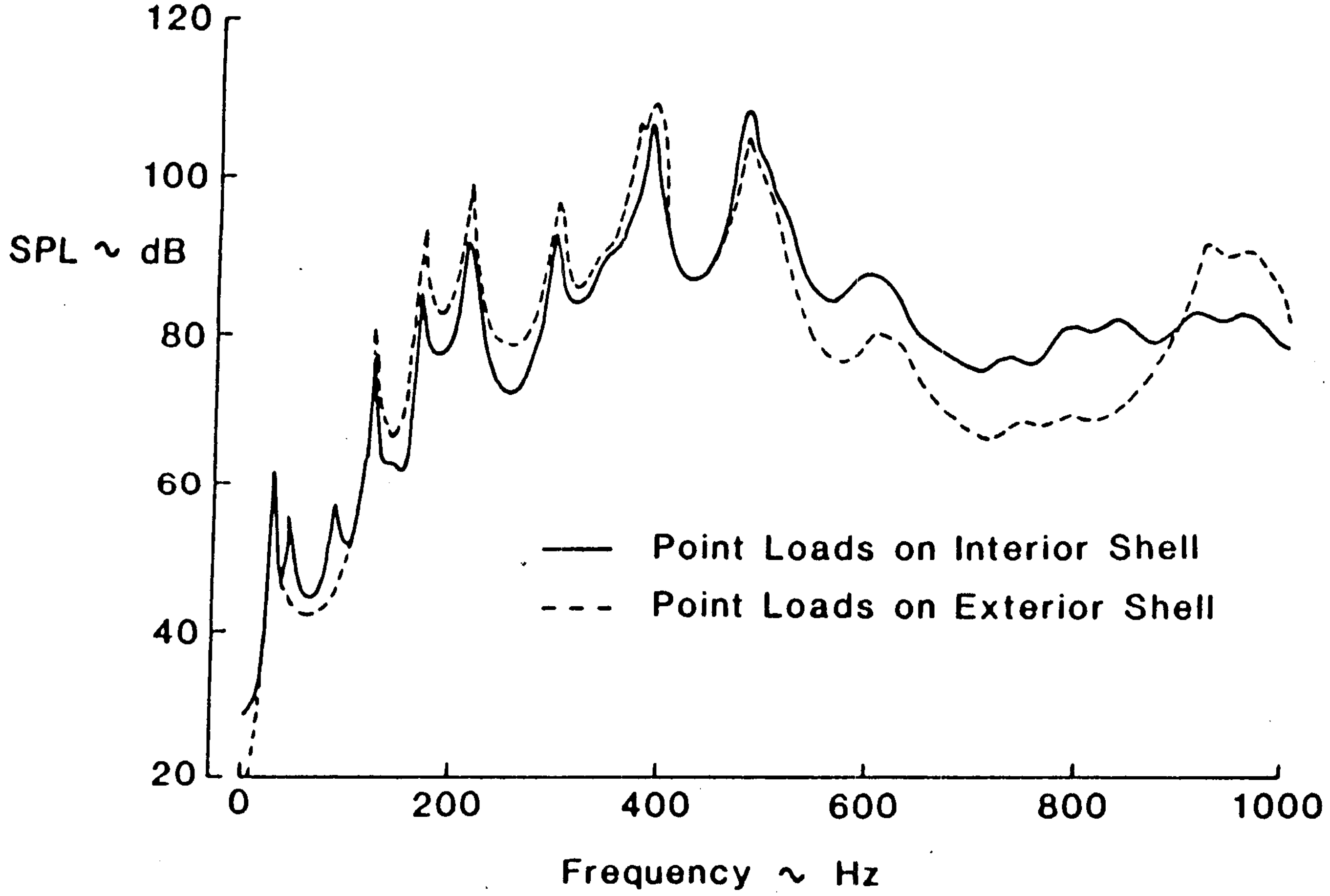

Fig. 23 Sound pressure levels in a composite shell for different loading conditions

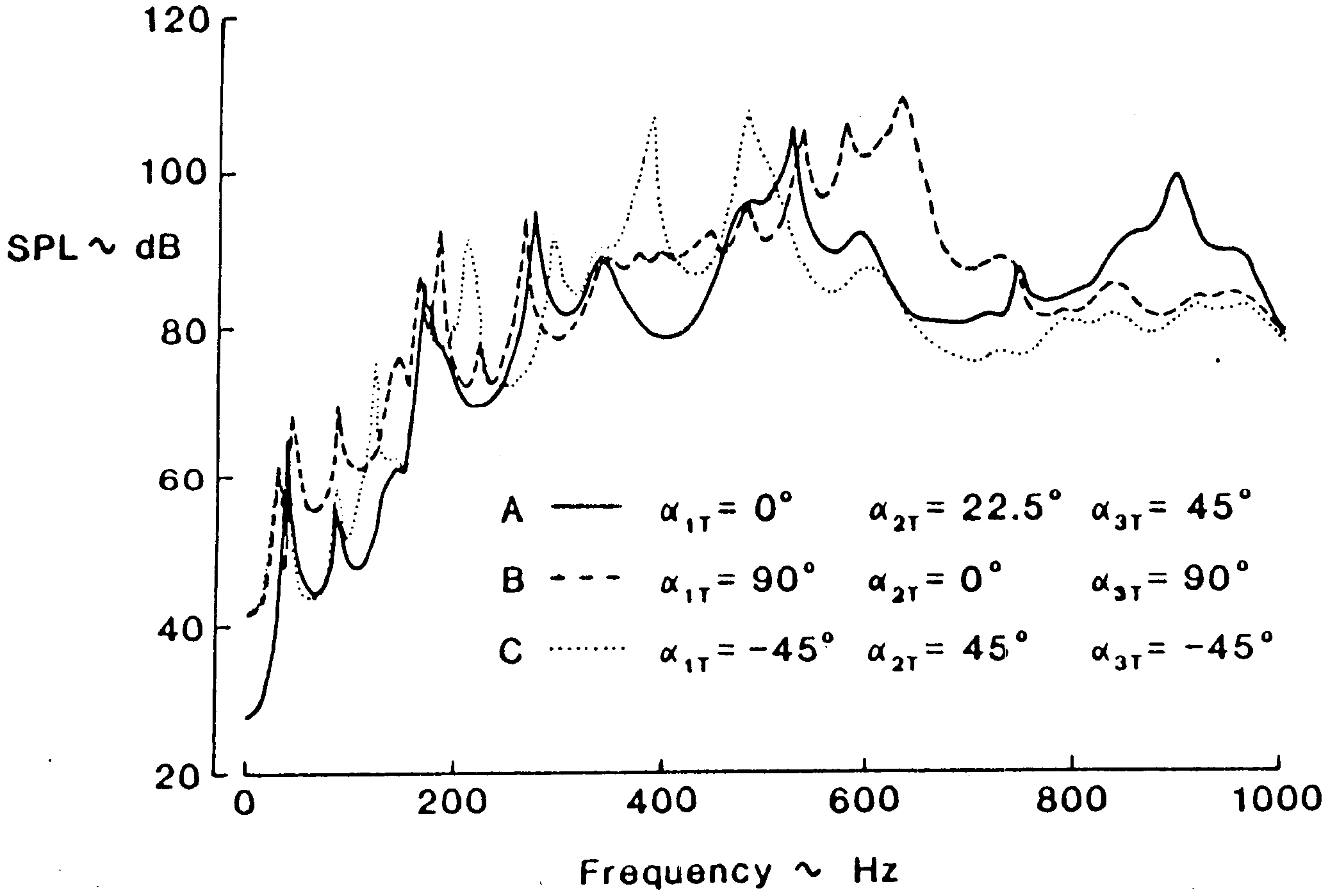

Fig. 24 Sound pressure levels in a composite shell for different fiber orientations (interior point loads)

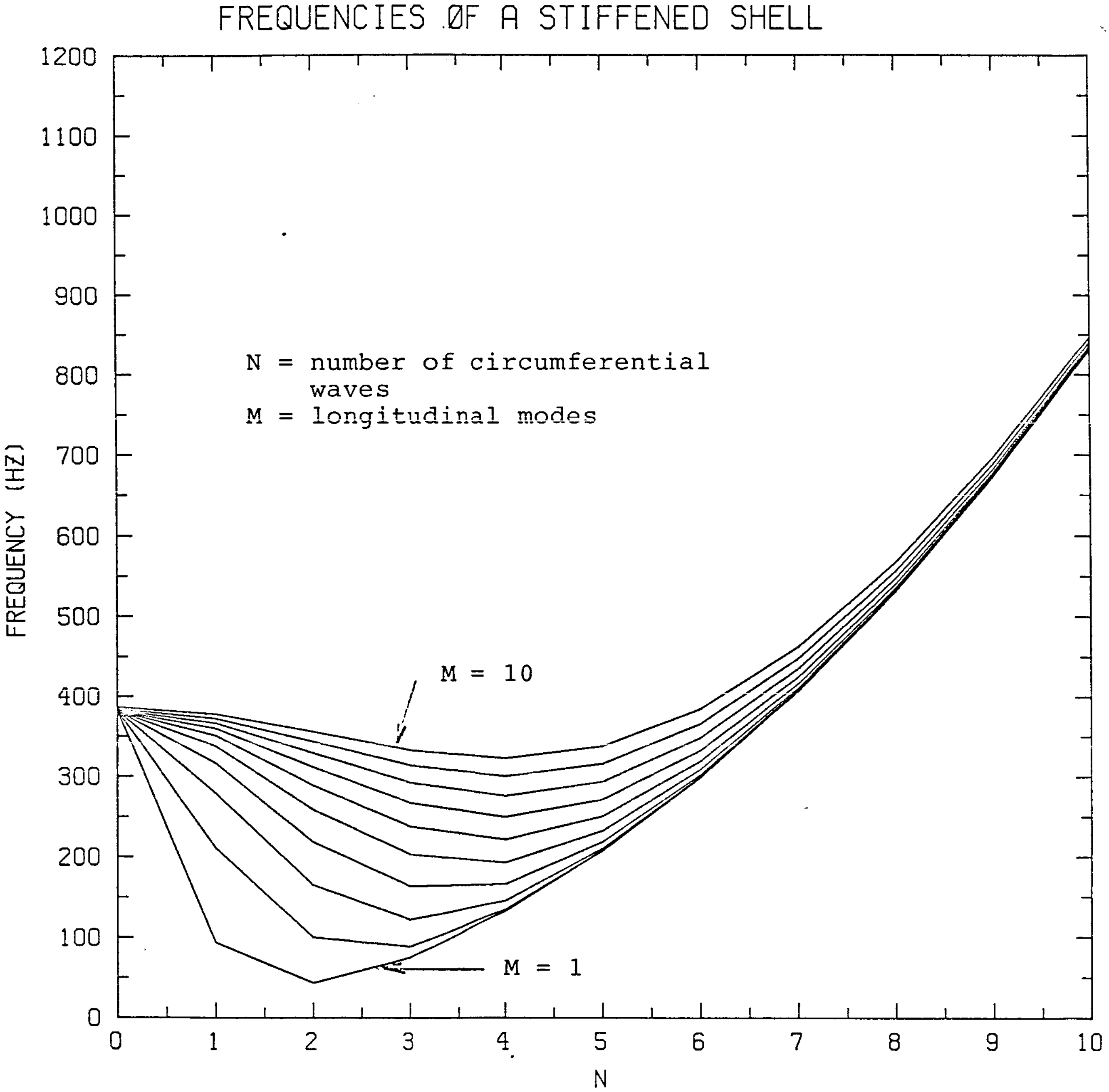

Fig. 25 Natural frequencies of a shell stiffened with 2 frames (distance between stringers = 20 in)

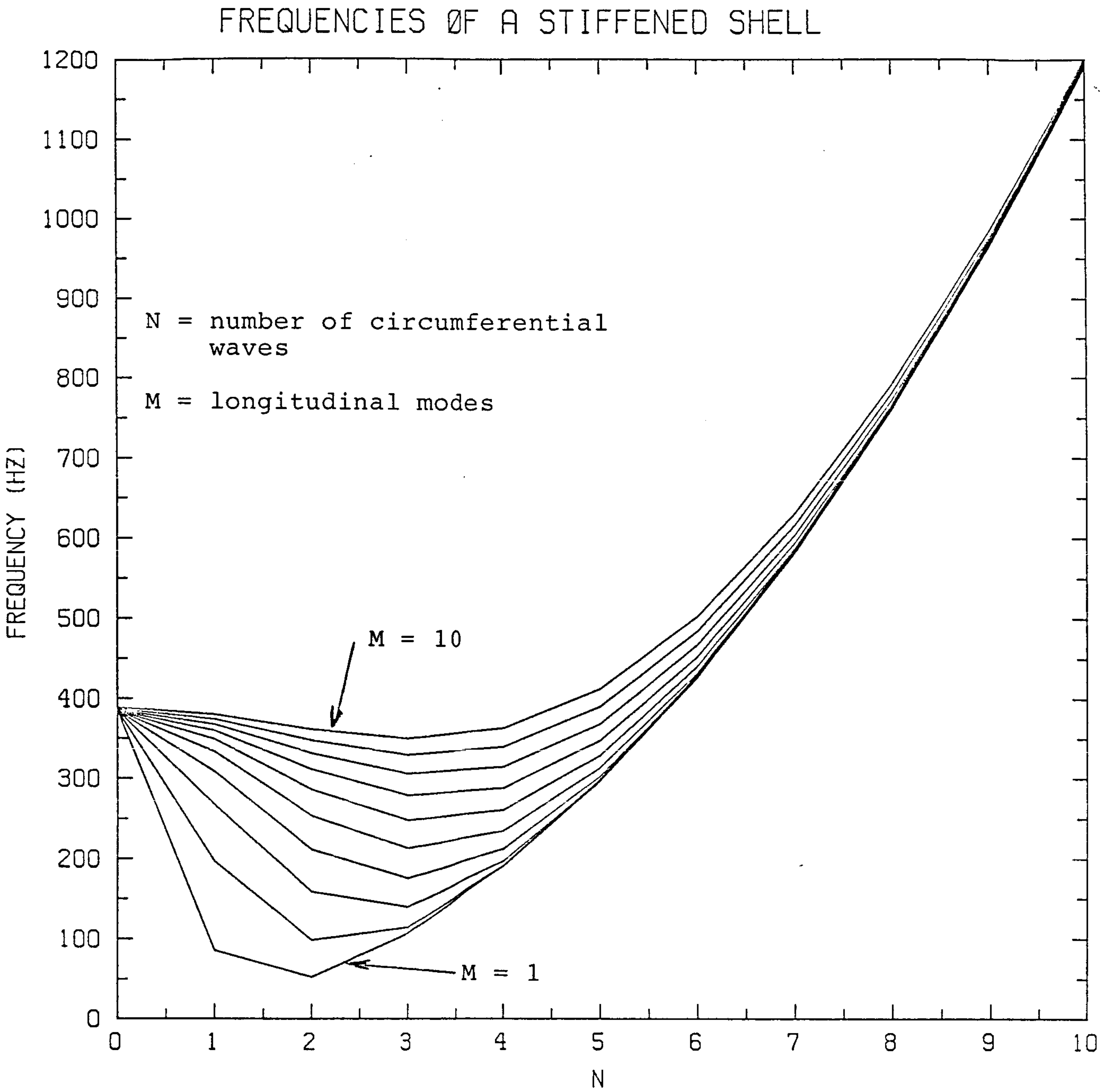

Fig. 26 Natural frequencies of a shell stiffened with eight frames (distance between the stringers = 20 in)

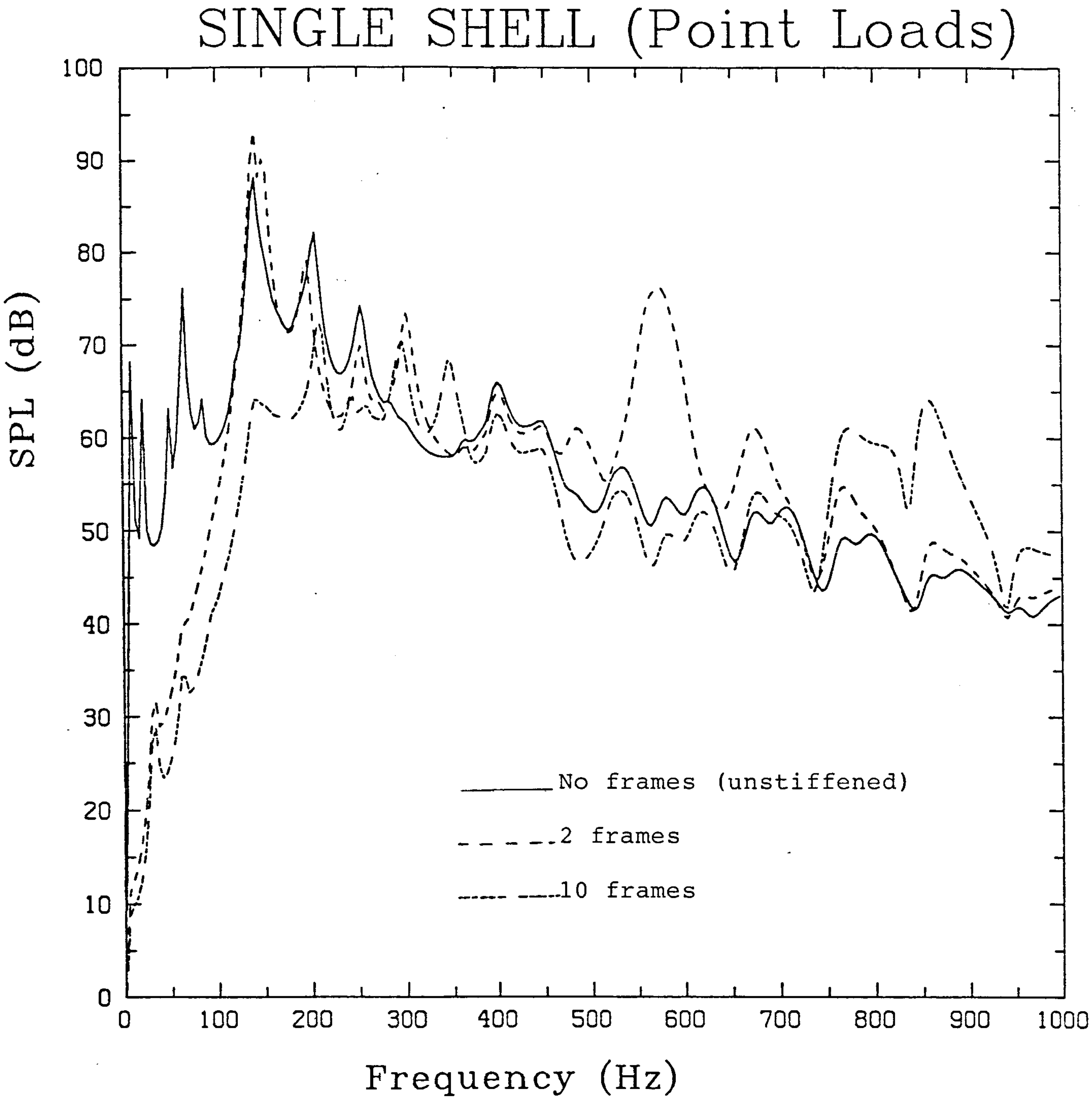

Fig. 27 Interior sound pressure levels for different shell configurations (no stringers)

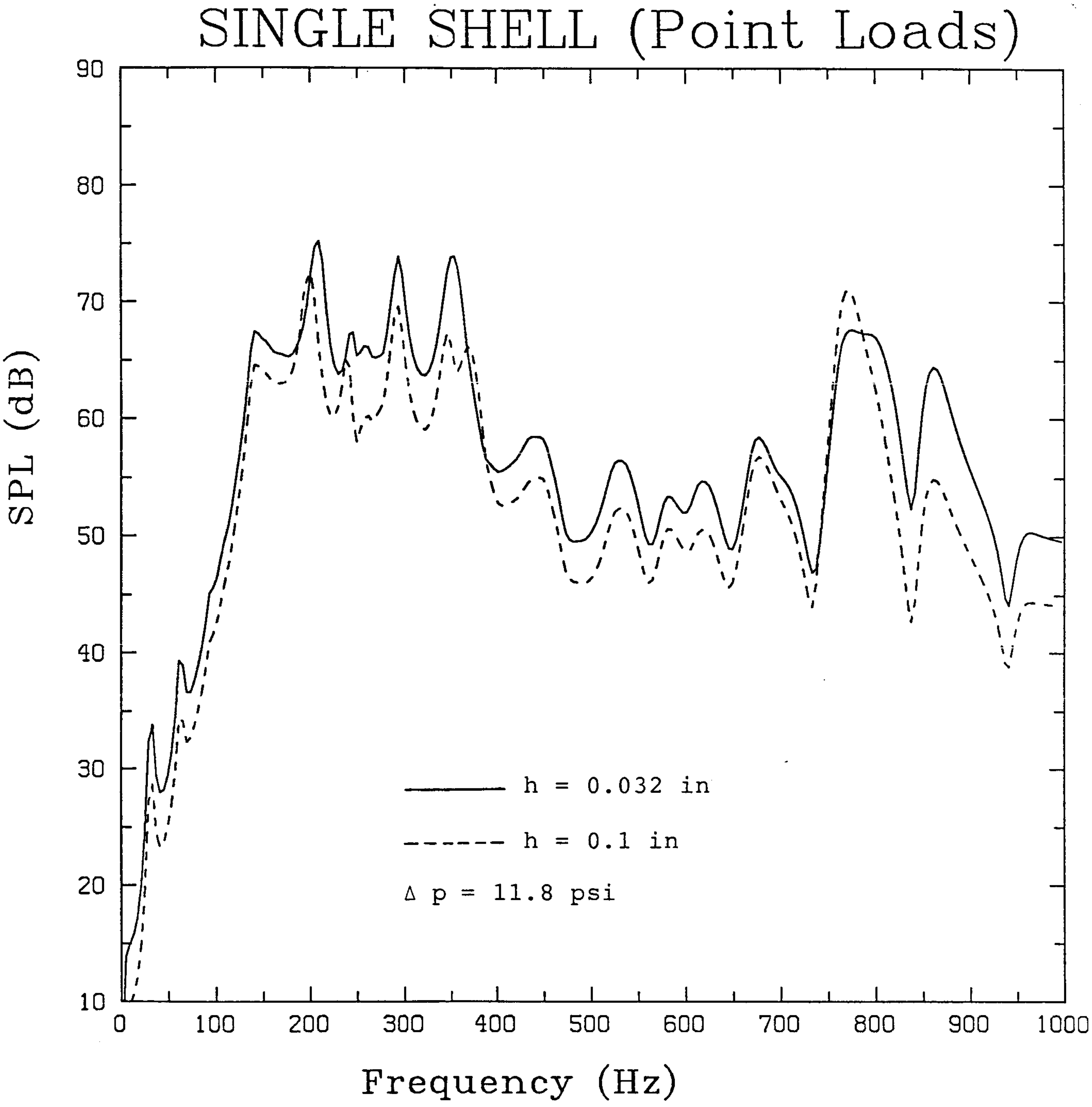

Fig. 28 Interior sound pressure levels for different shell skin thicknesses

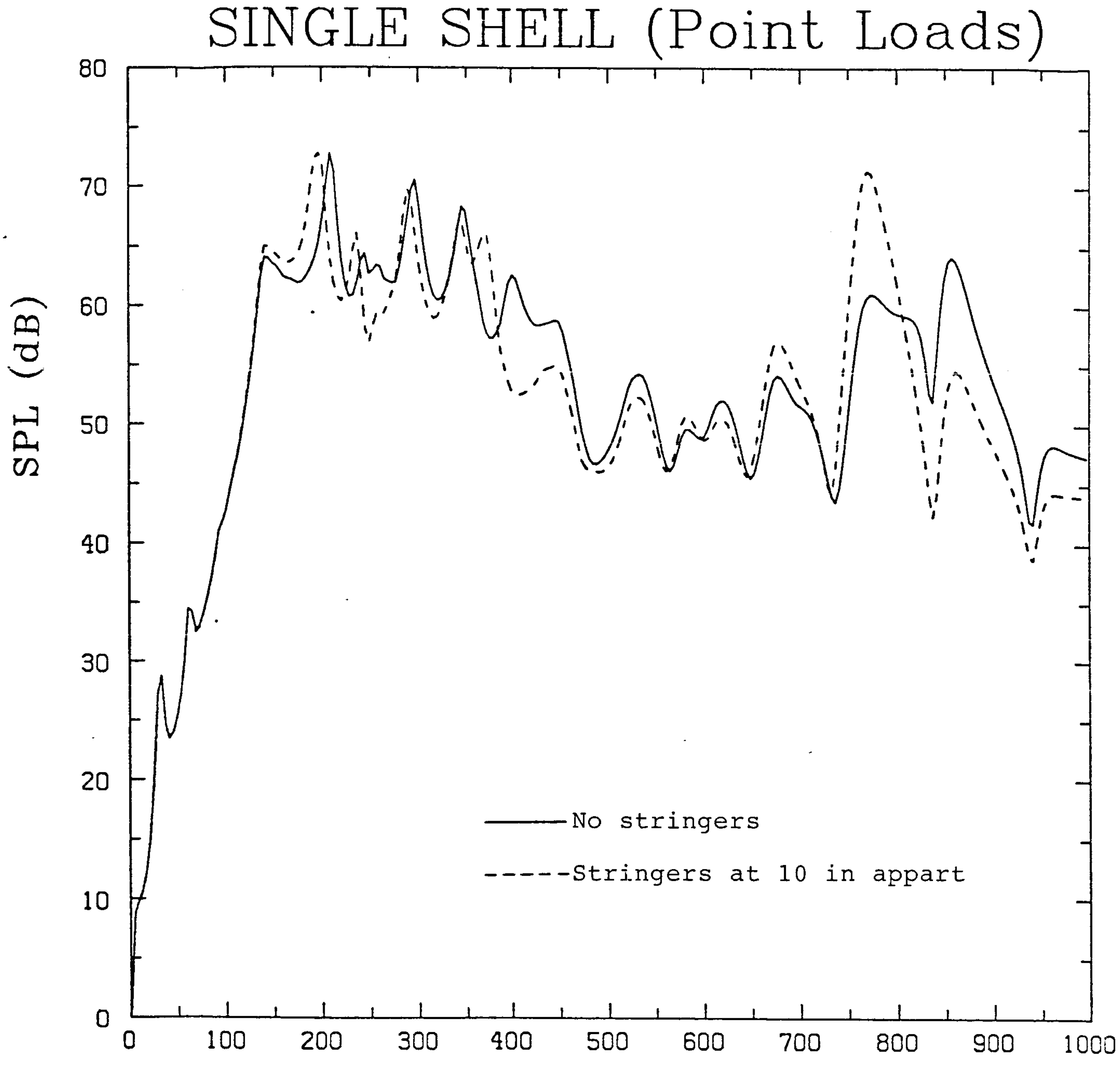

Fig. 29 Interior sound pressure levels for a shell with and without stringers

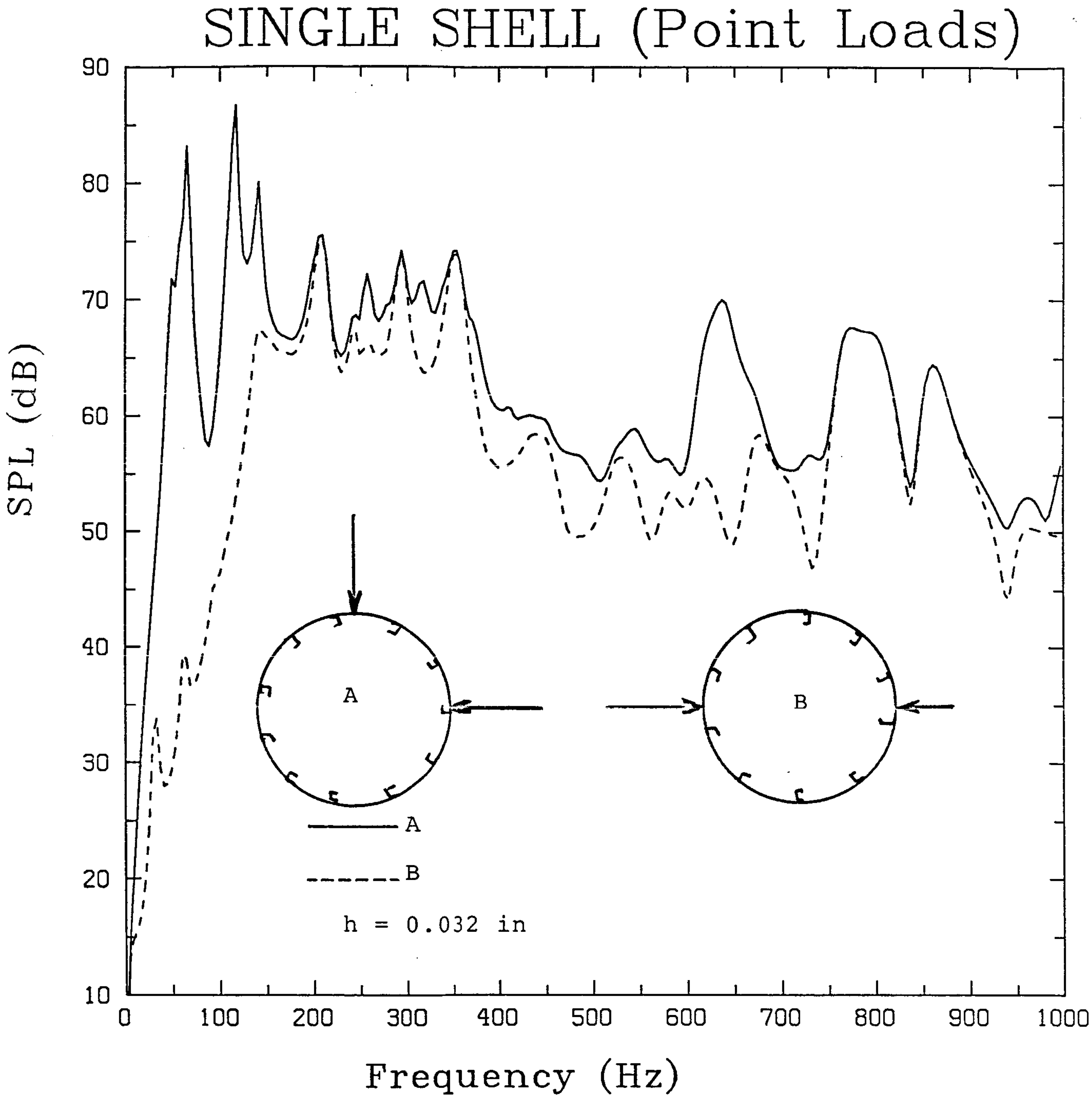

Fig. 30 Sound pressure levels for different locations of input forces

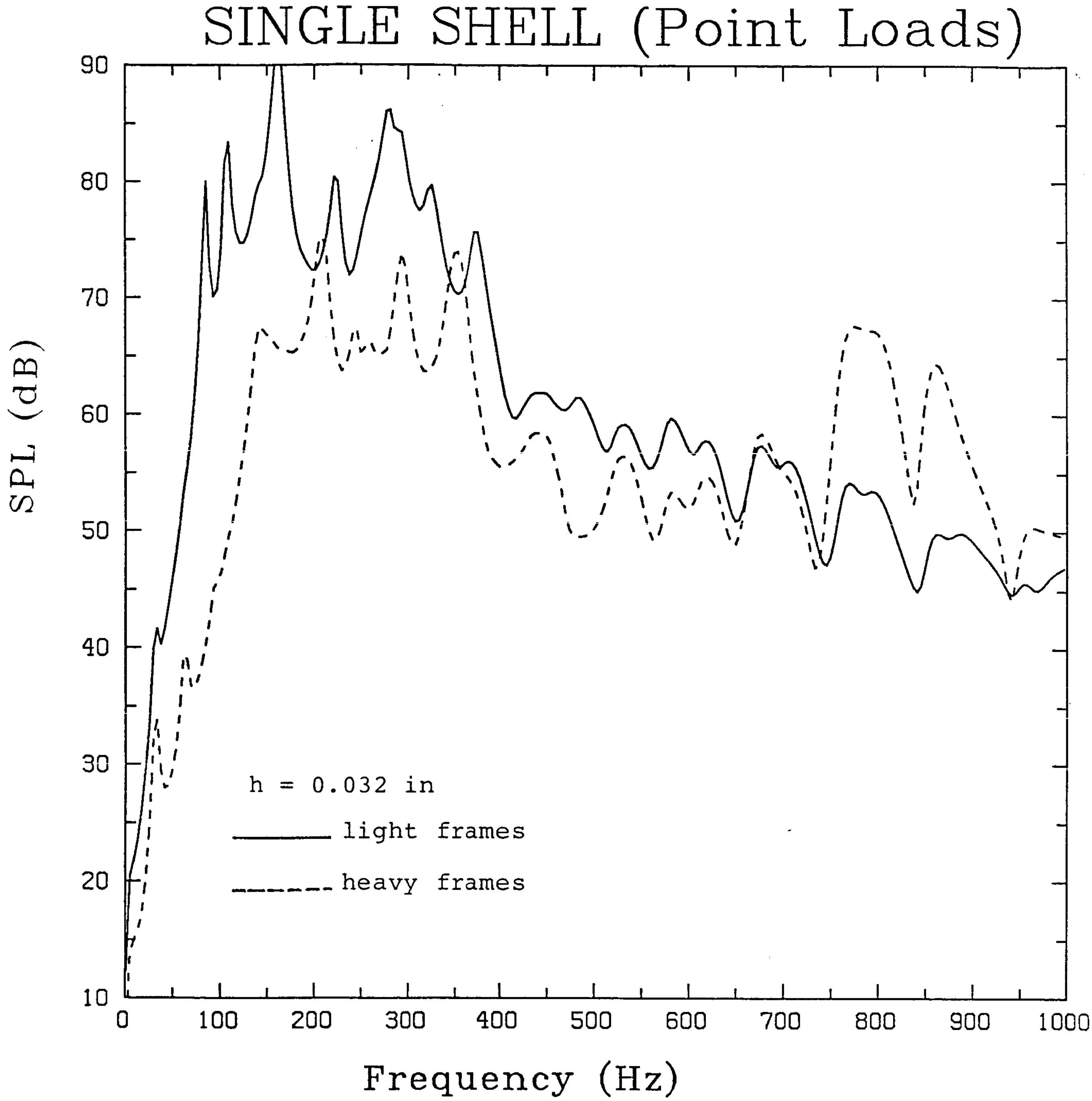

Fig. 31 Sound pressure levels for a cylinder stiffened with heavy and light frames (ten frames)

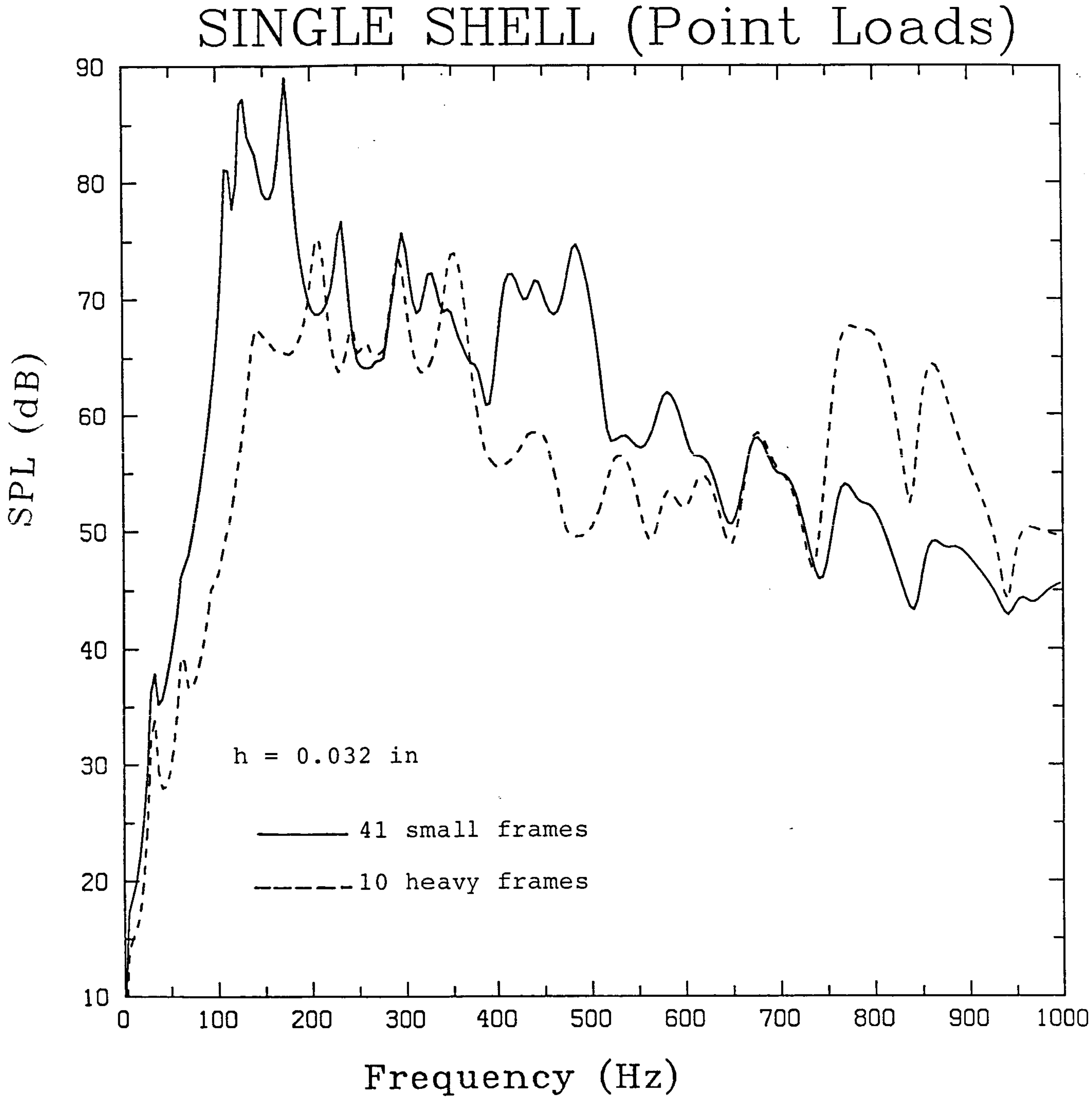

Fig. 32 Interior sound pressure levels for a shell stiffened either with 10 heavy frames or 41 small frames

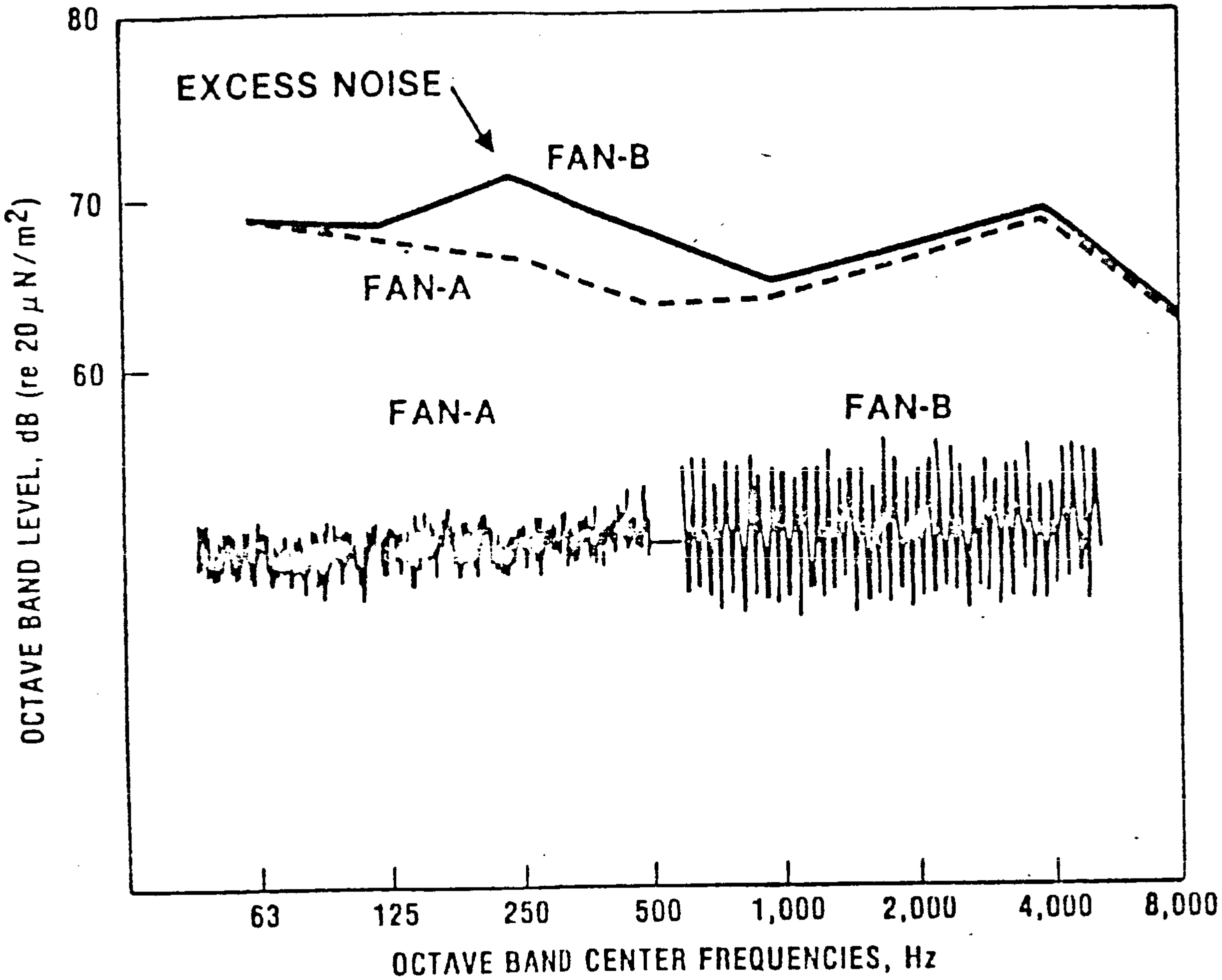

Fig. 33 Interior noise levels generated inside Skylab from operation of two different fans

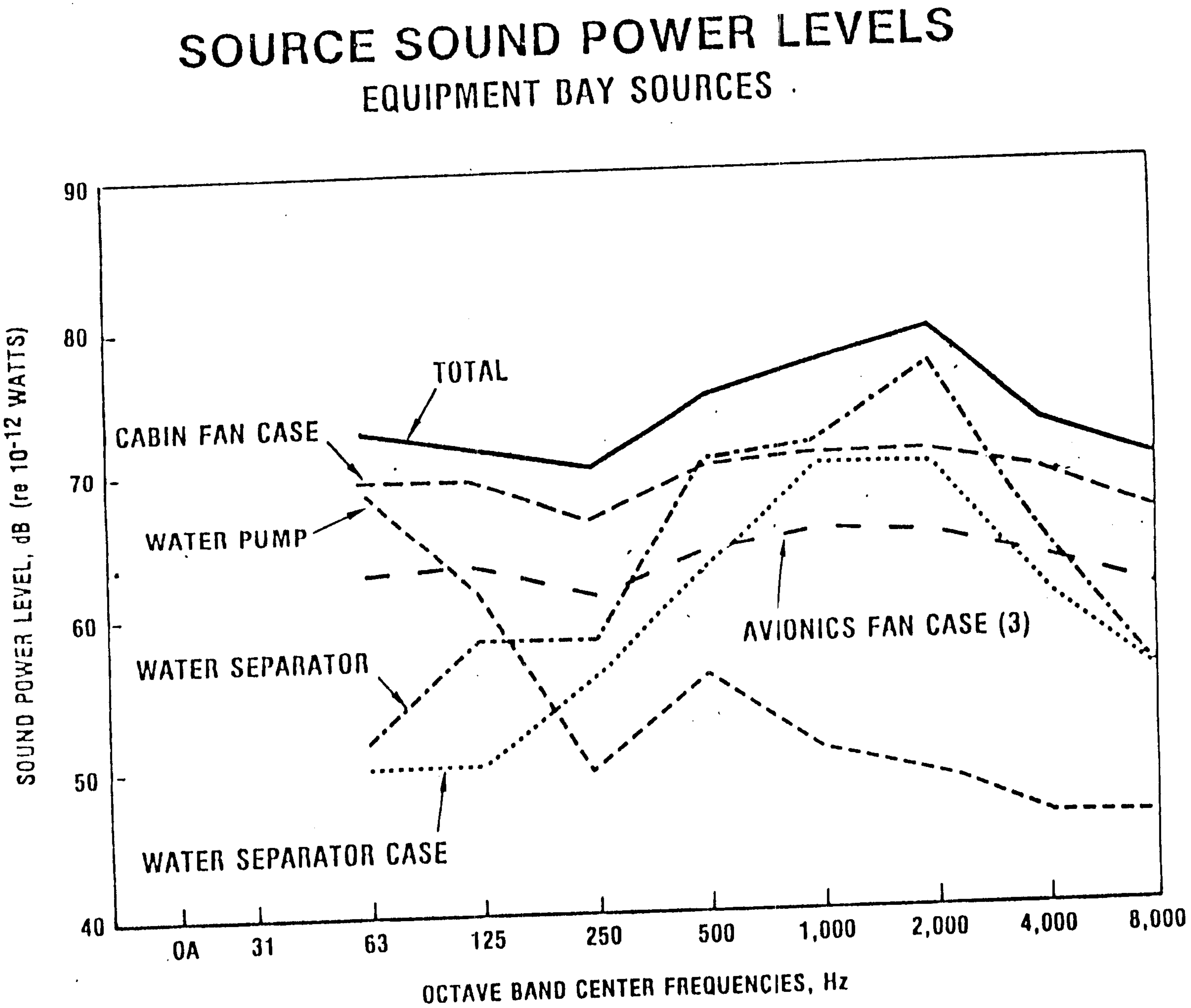

Fig. 34 Interior noise levels inside the Skylab from equipment bay sources

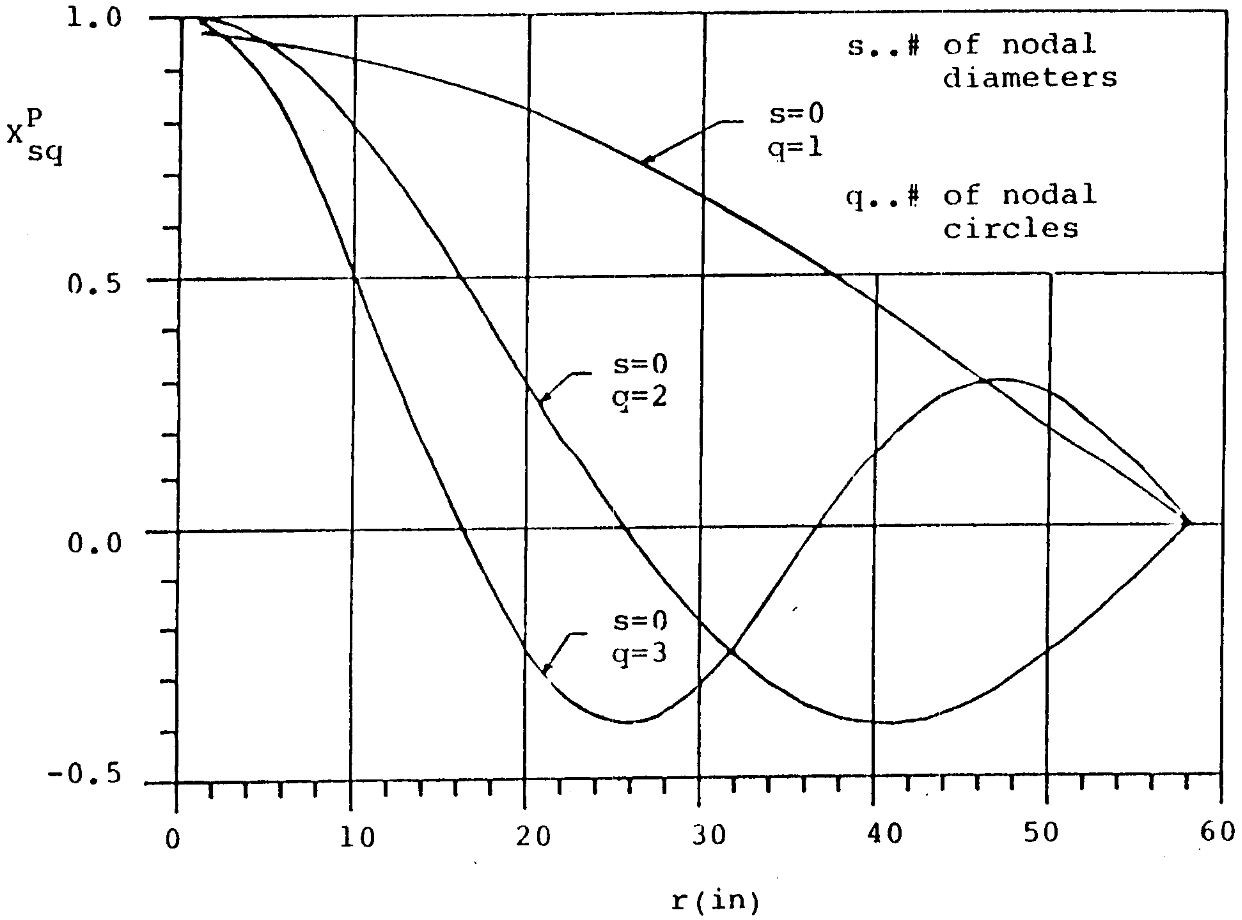

Fig. 35 Structural modes of end circular plates

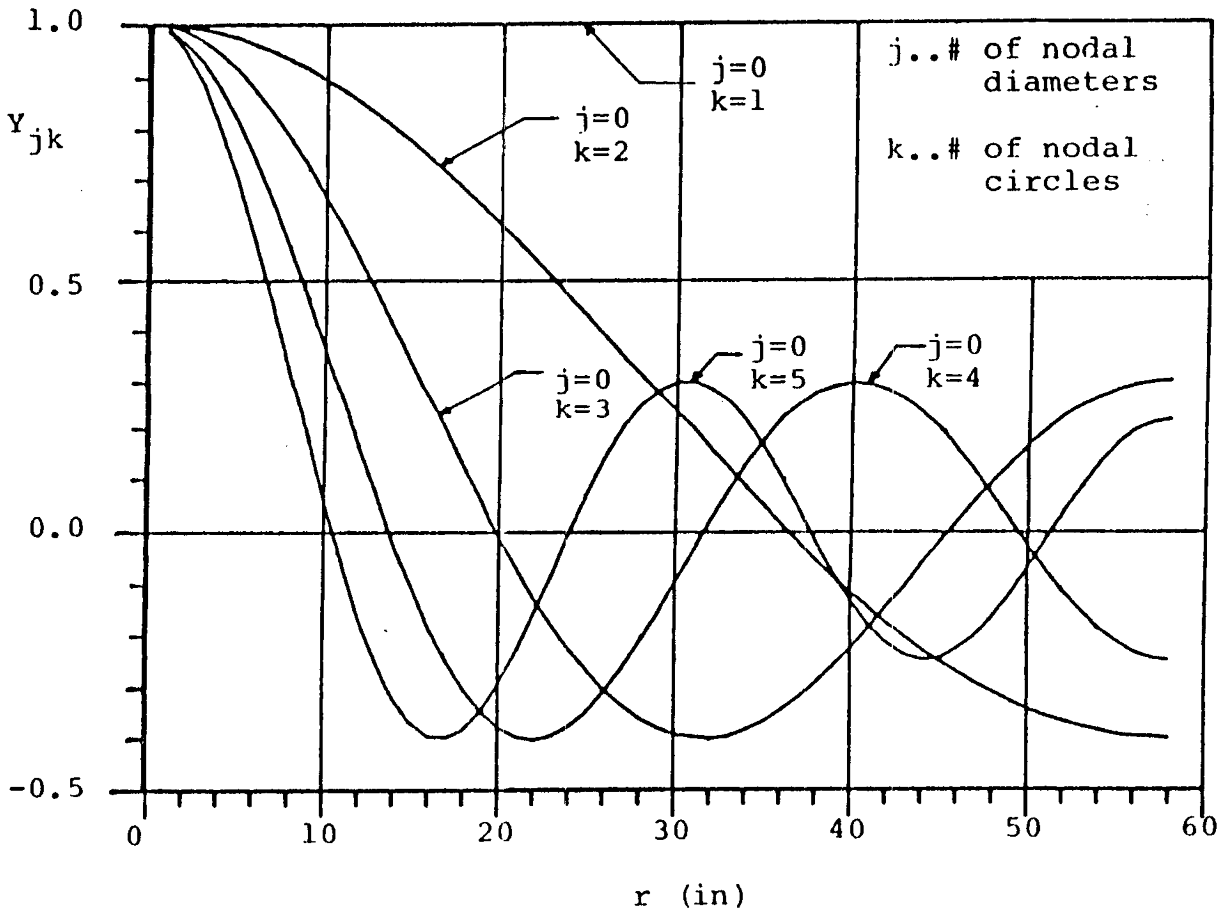

Fig. 36 Radial acoustic modes in a cylindrical enclosure

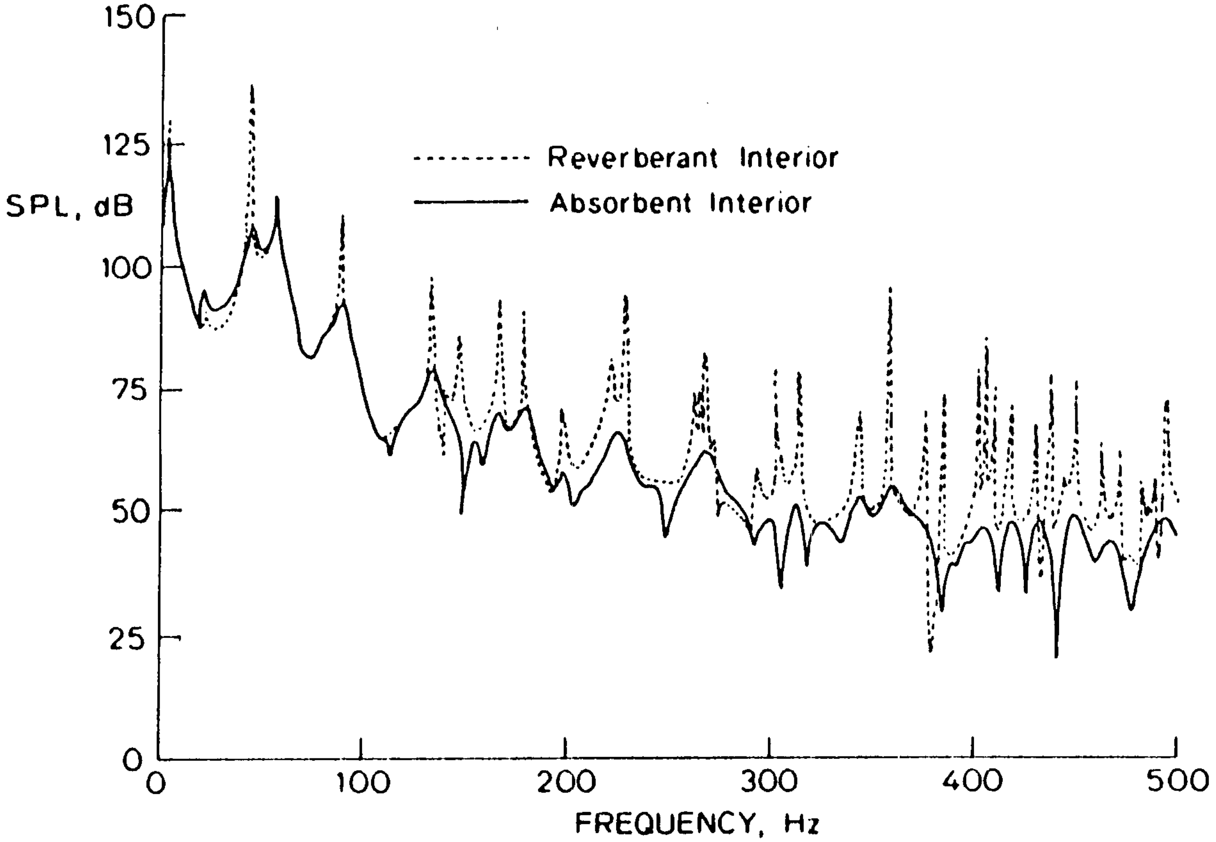

Fig. 37 Sound pressure levels due to end plate vibrations

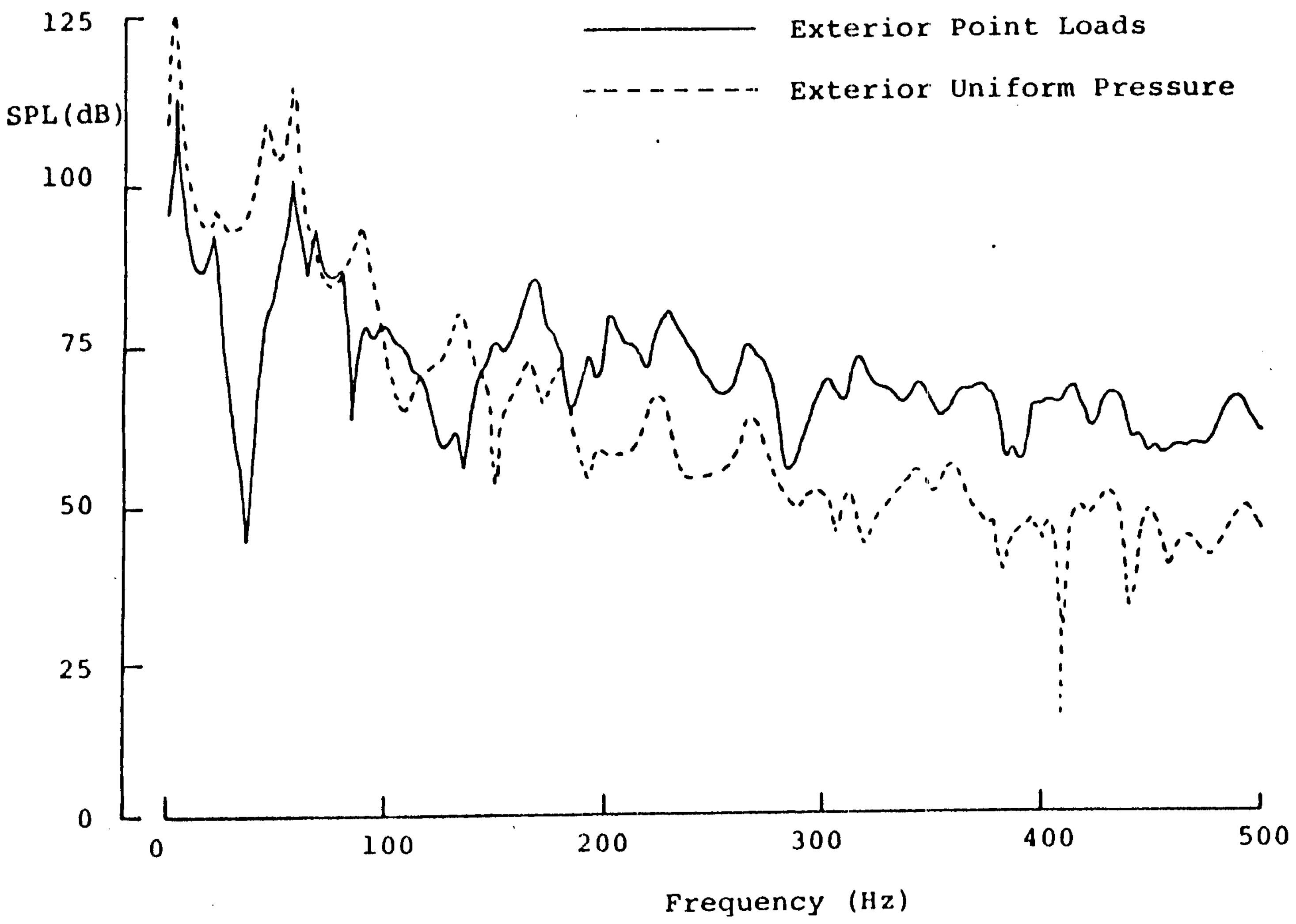

Fig. 38 Sound pressure levels due to end plate vibrations with different loading conditions

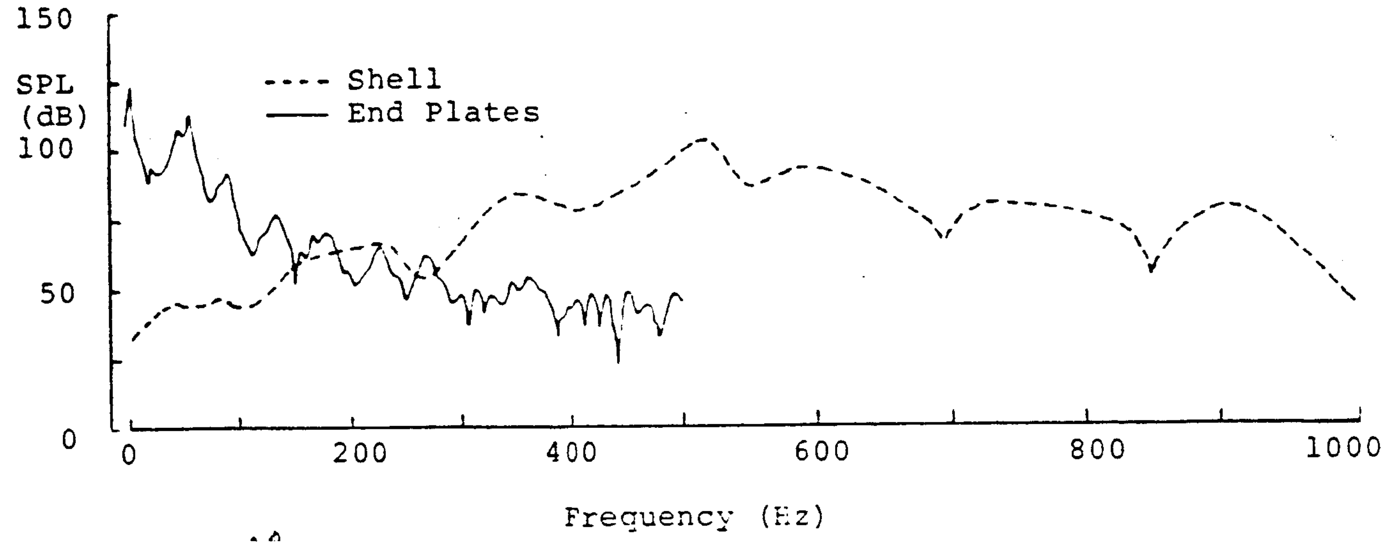

Fig. 39 Sound pressure levels due to vibrating shell and end plates (exterior 120 dB uniform pressure)

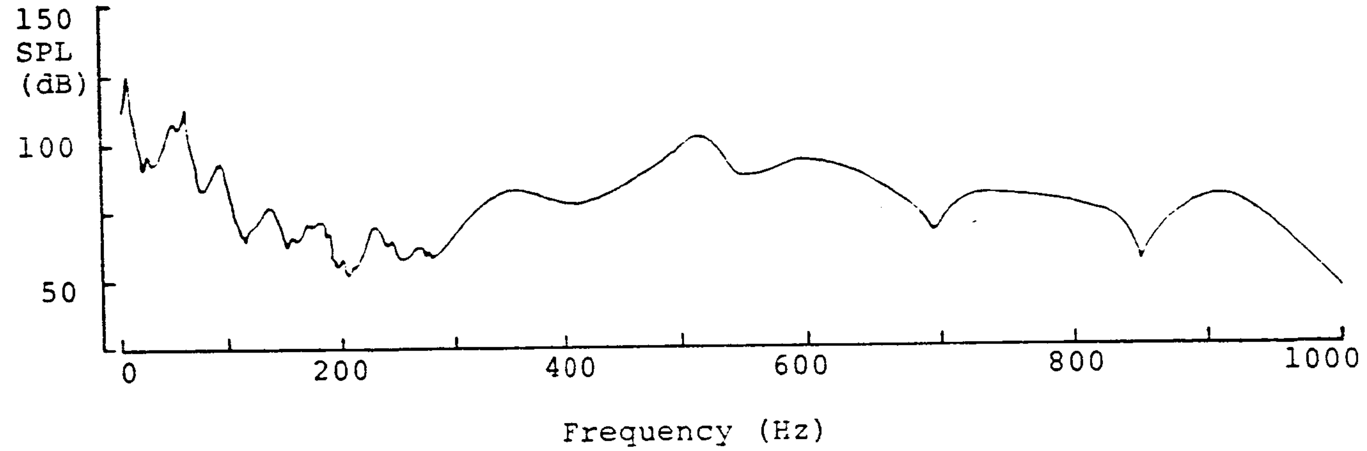

Fig. 40 Total interior noise due to 120 dB exterior pressure

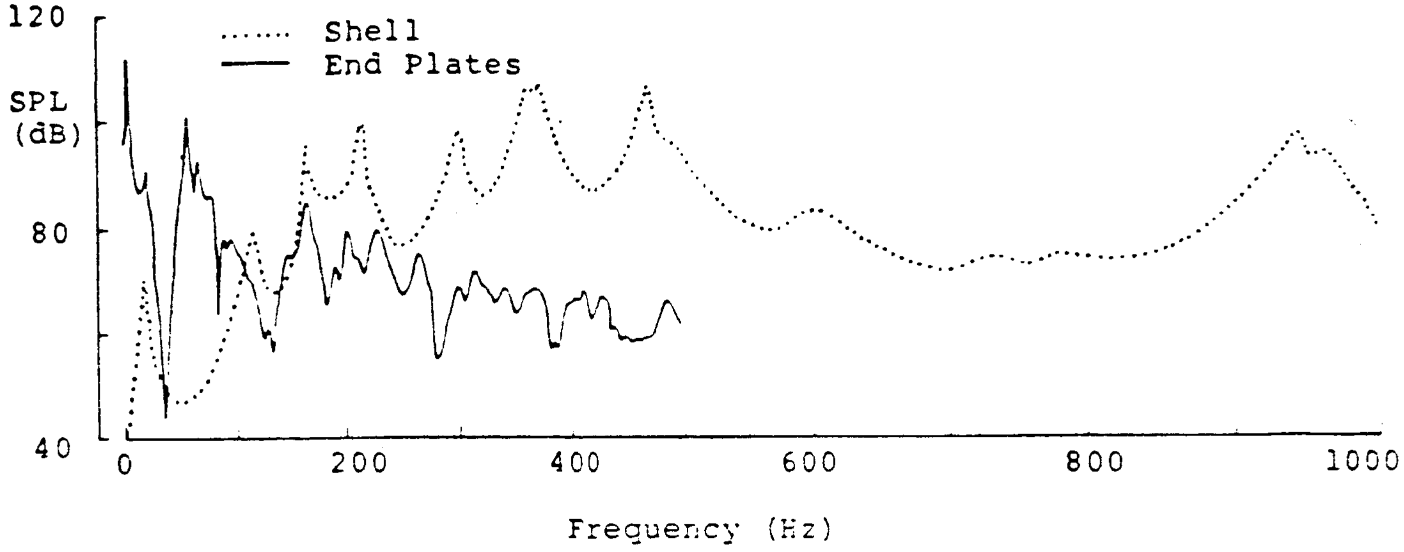

Fig. 41 Sound pressure levels due to point load inputs

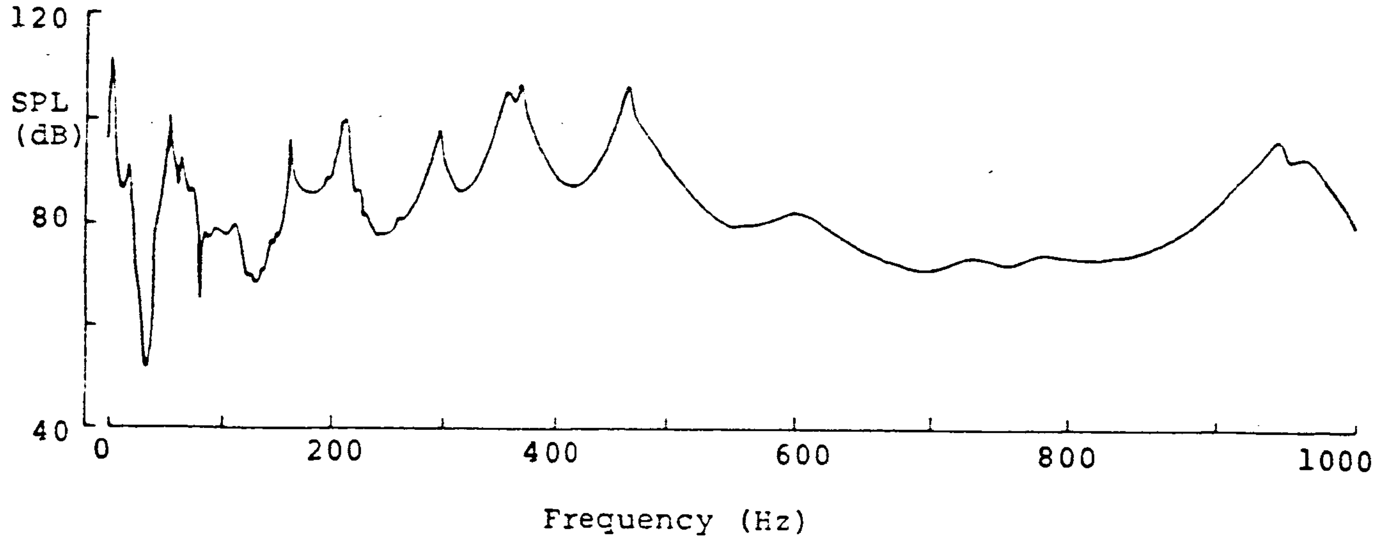

Fig. 42 Total interior noise due to point load inputs

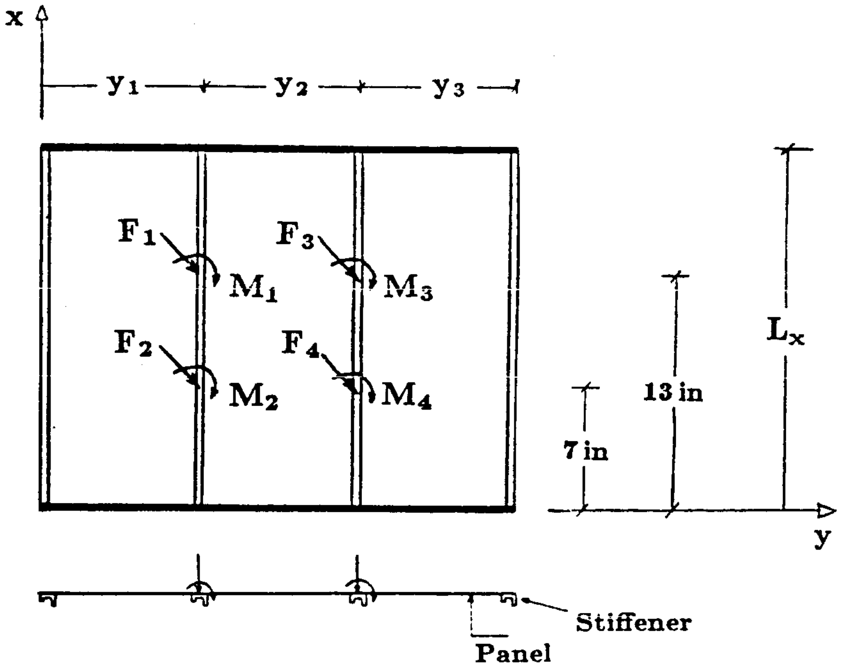

Fig. 43 *A three bay stiffened panel.*

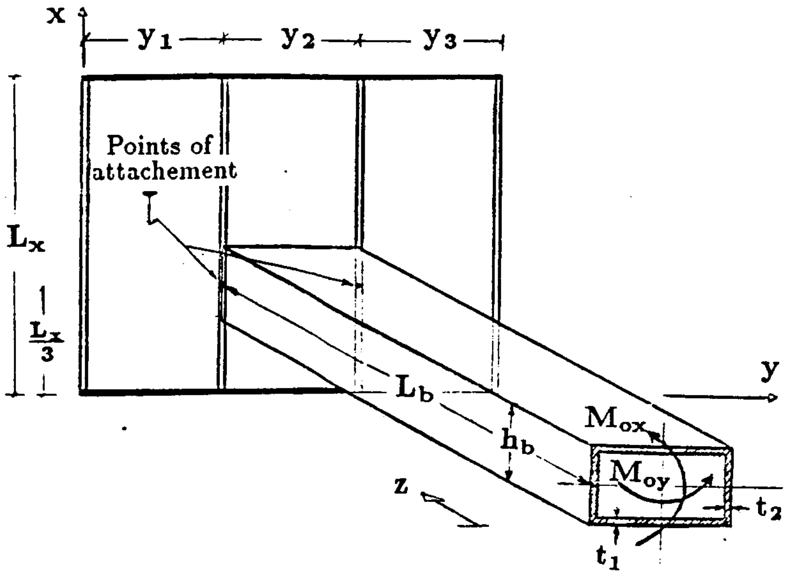

Fig.44 *Skin-stringer - box beam structure.*

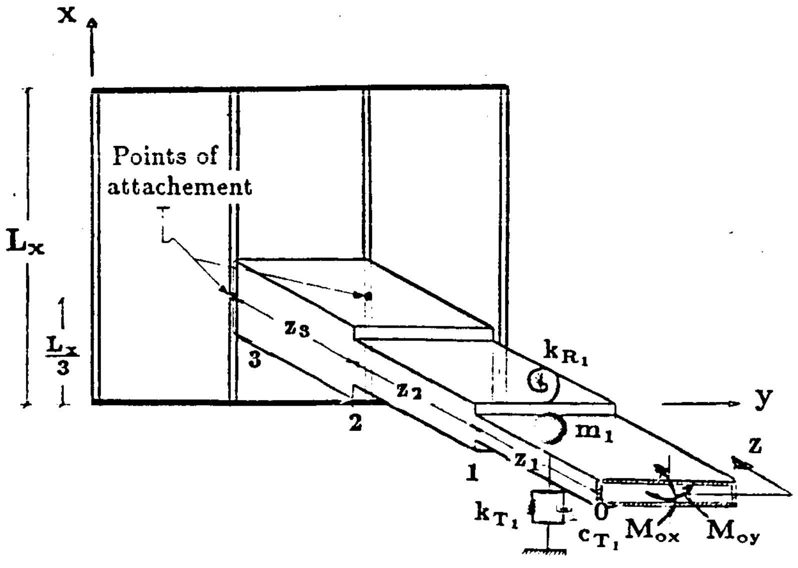

Fig.45 *Skin-stringer - stiffened box beam structure.*

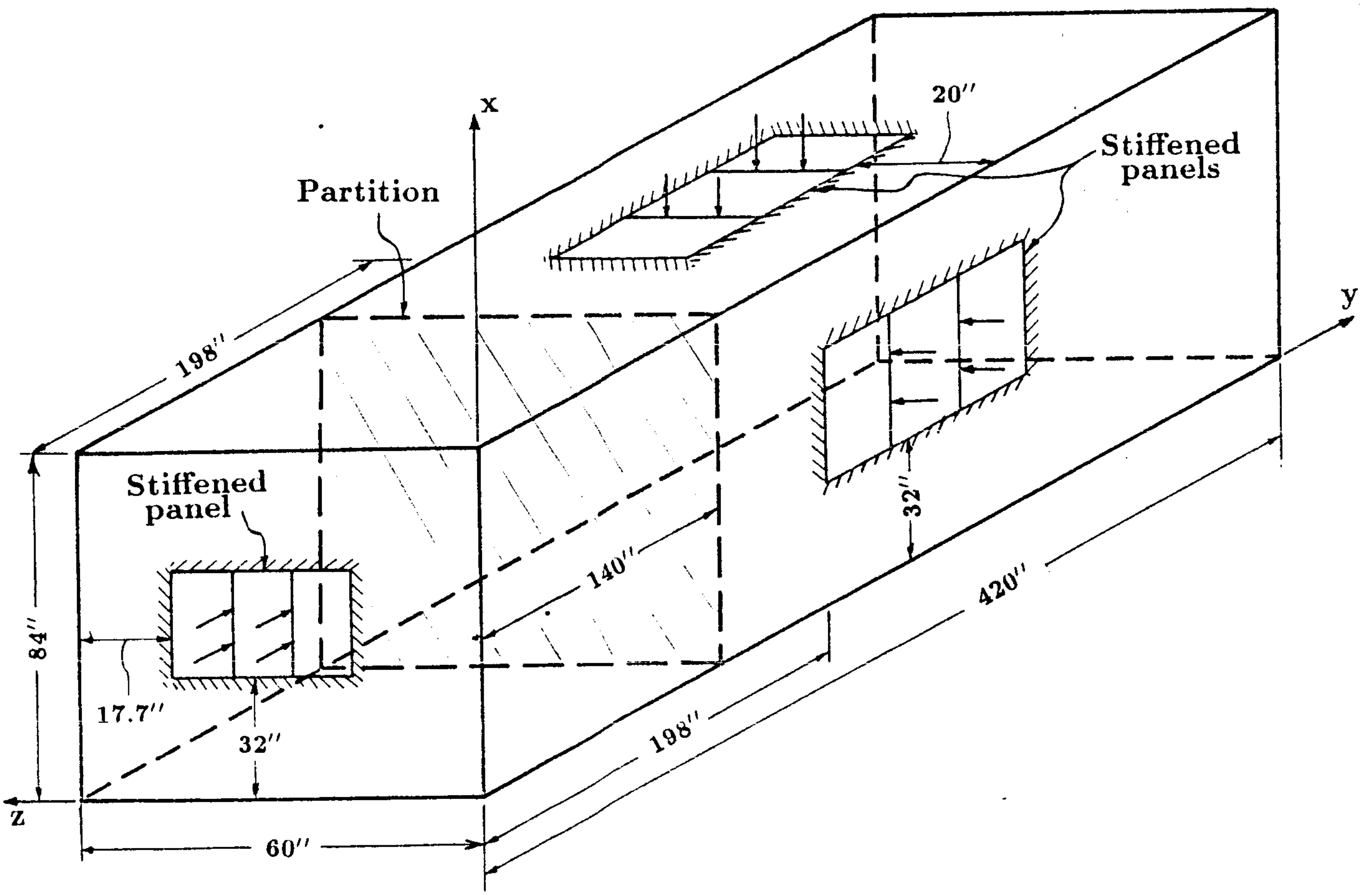

Fig. 46 Geometry of a rectangular enclosure

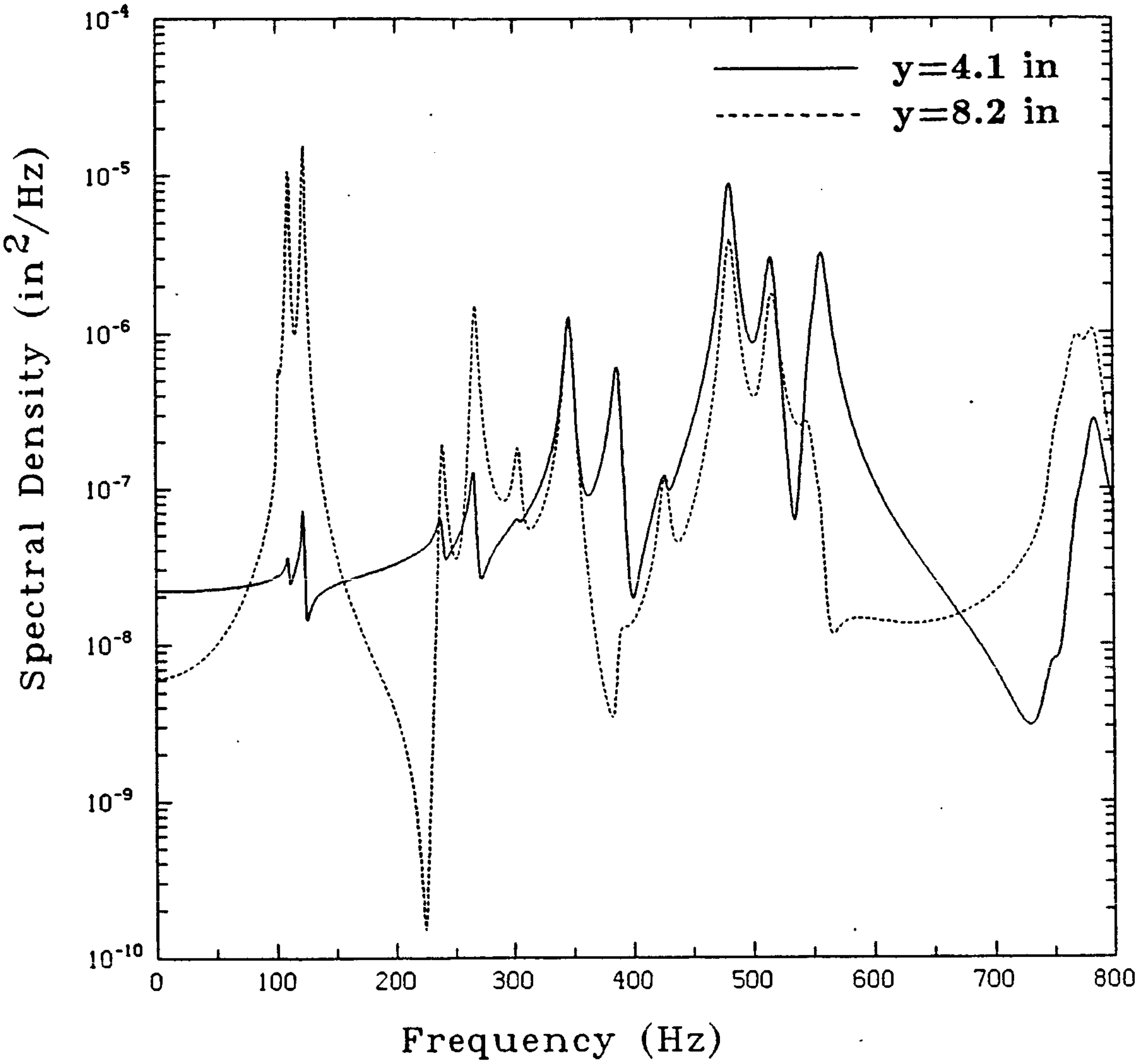

Fig. 47 *Deflection response spectral densities to point forces.*

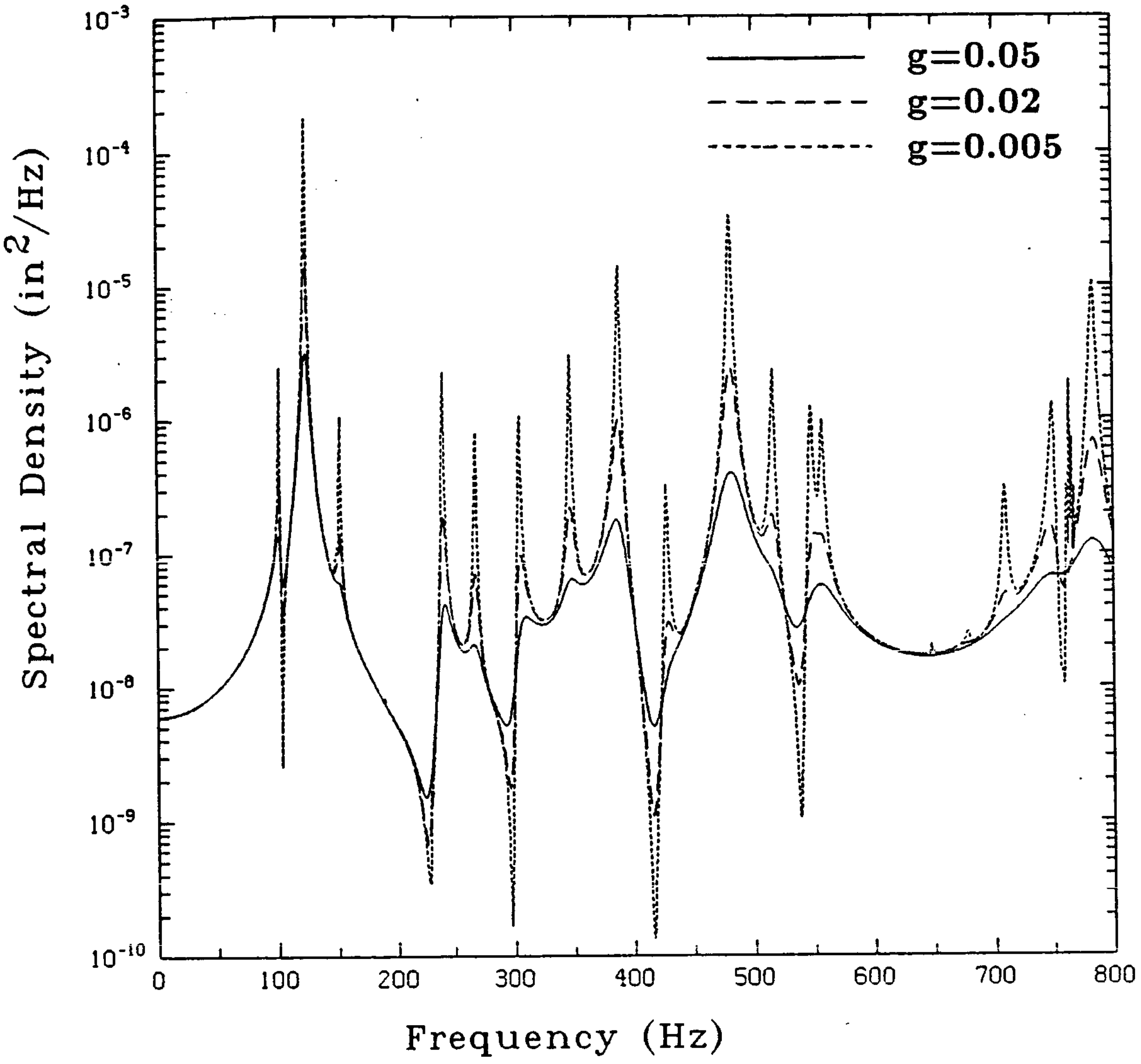

Fig. 48 *Deflection response spectral densities to point forces for different damping values.*

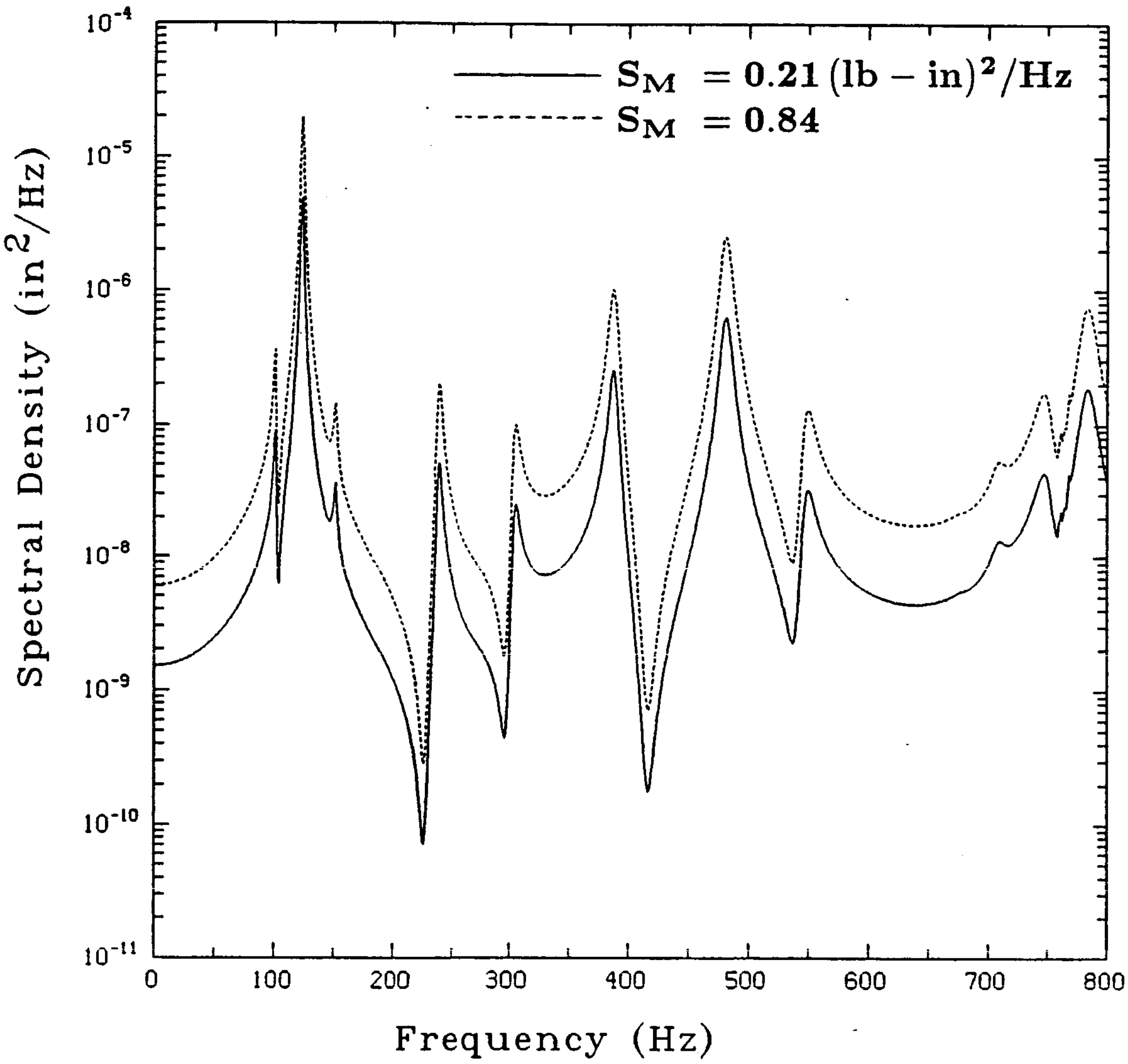

Fig. 49 *Deflection response spectral densities to point couples.*

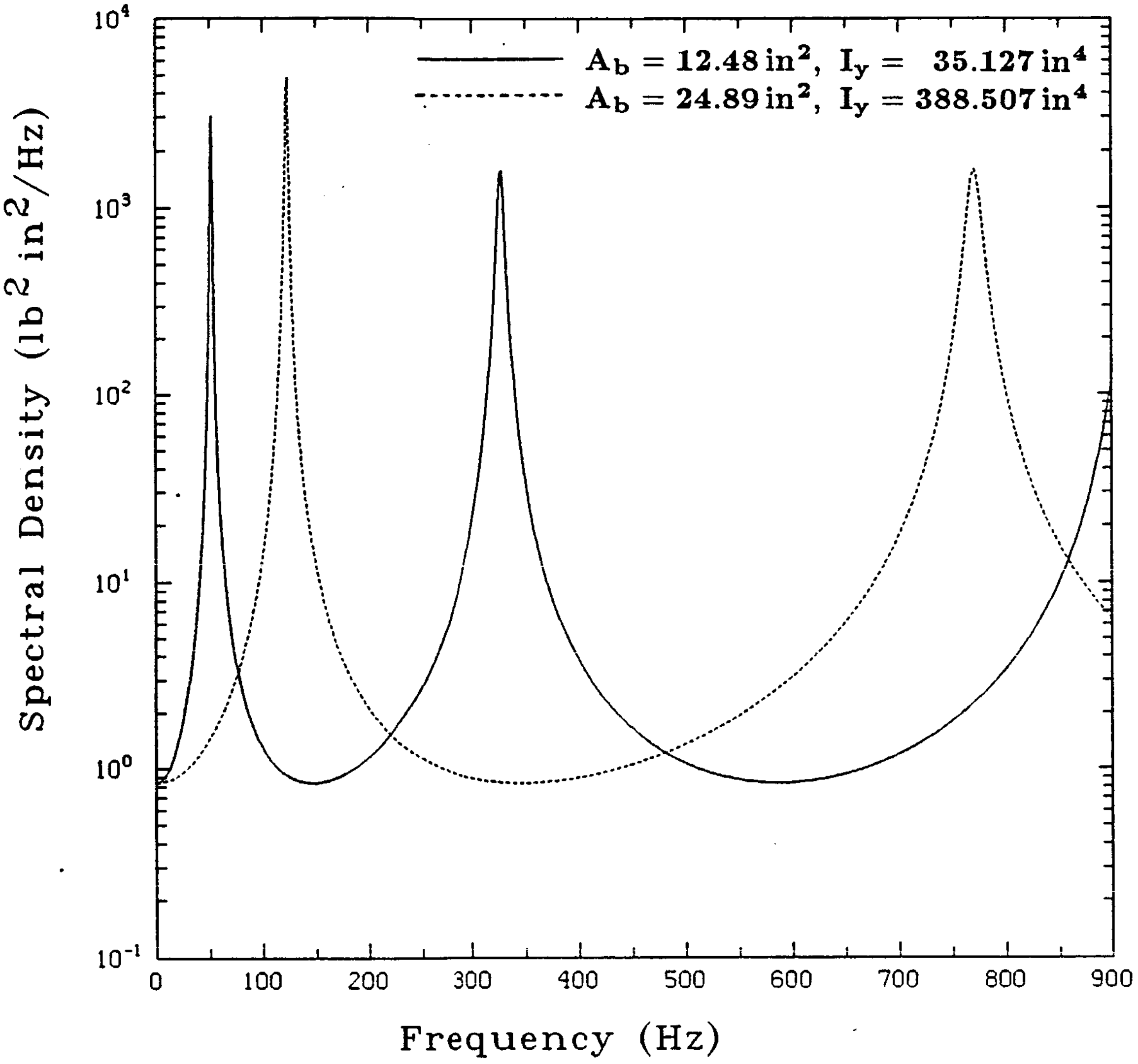

Fig. 50 *Bending moment spectral densities for a cantilever box beam.*

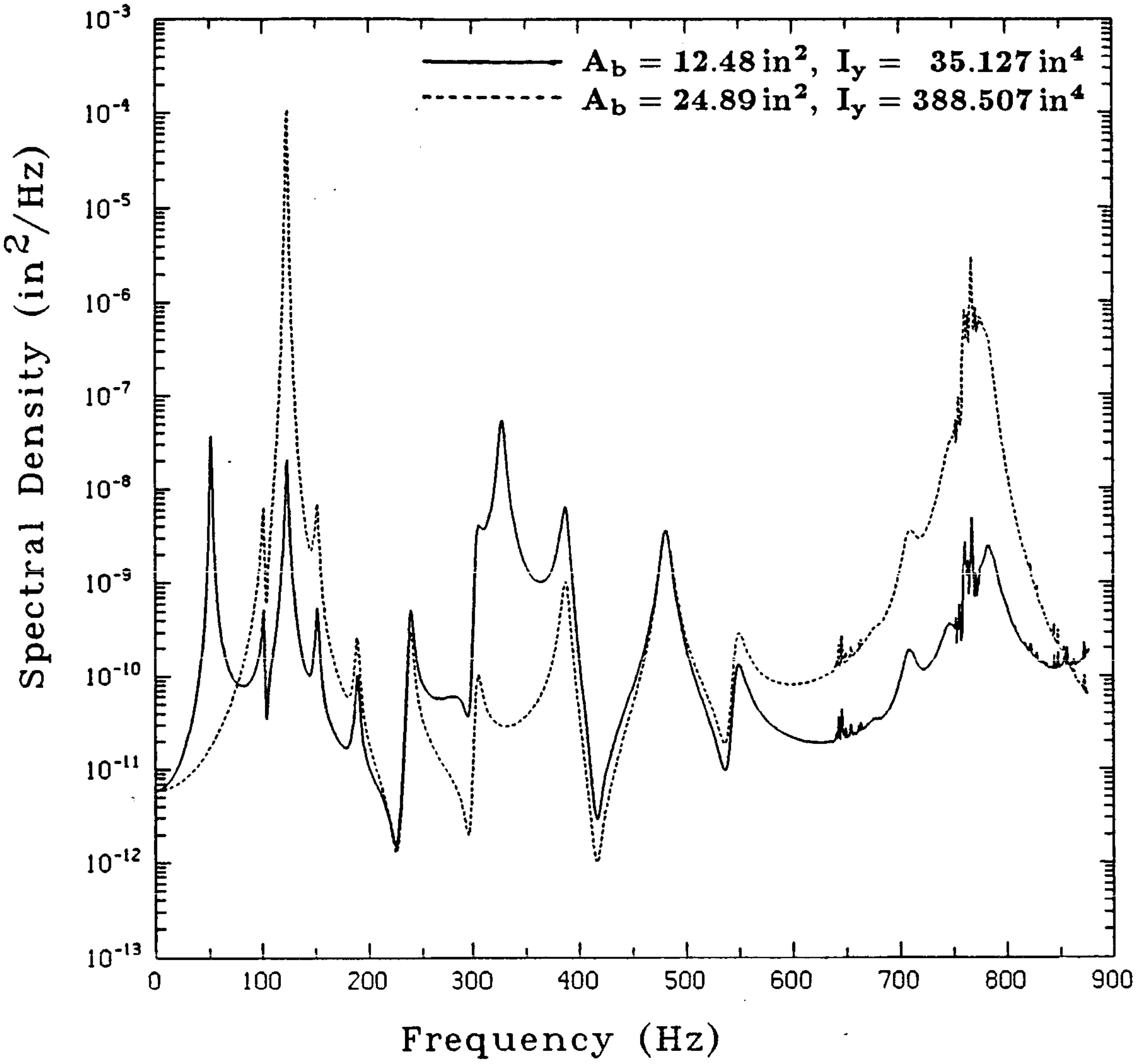

Fig. 51 *Deflection response spectral densities to calculated bending moment inputs.*

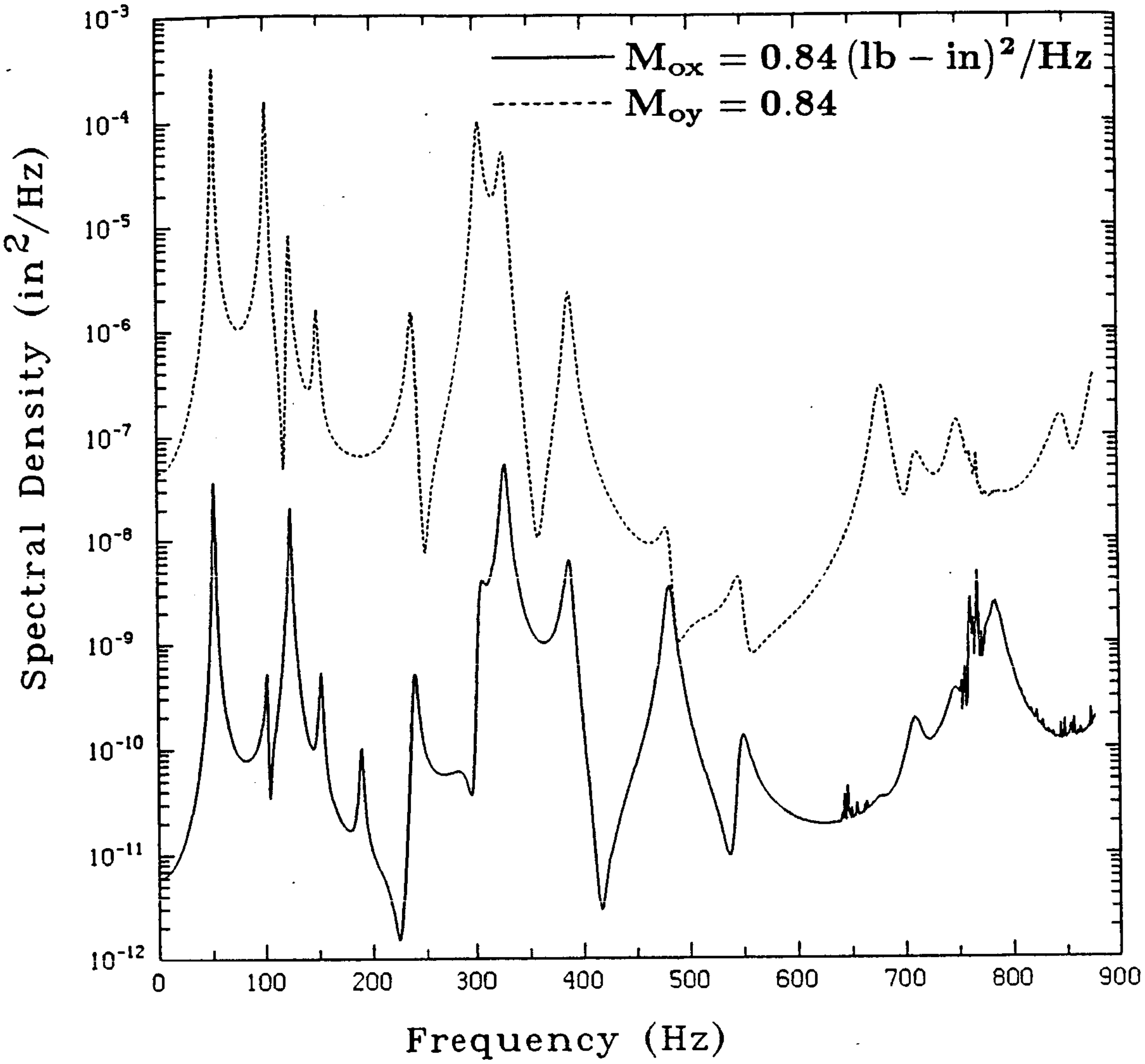

Fig. 52 *Deflection response spectral densities to different bending moment inputs.*

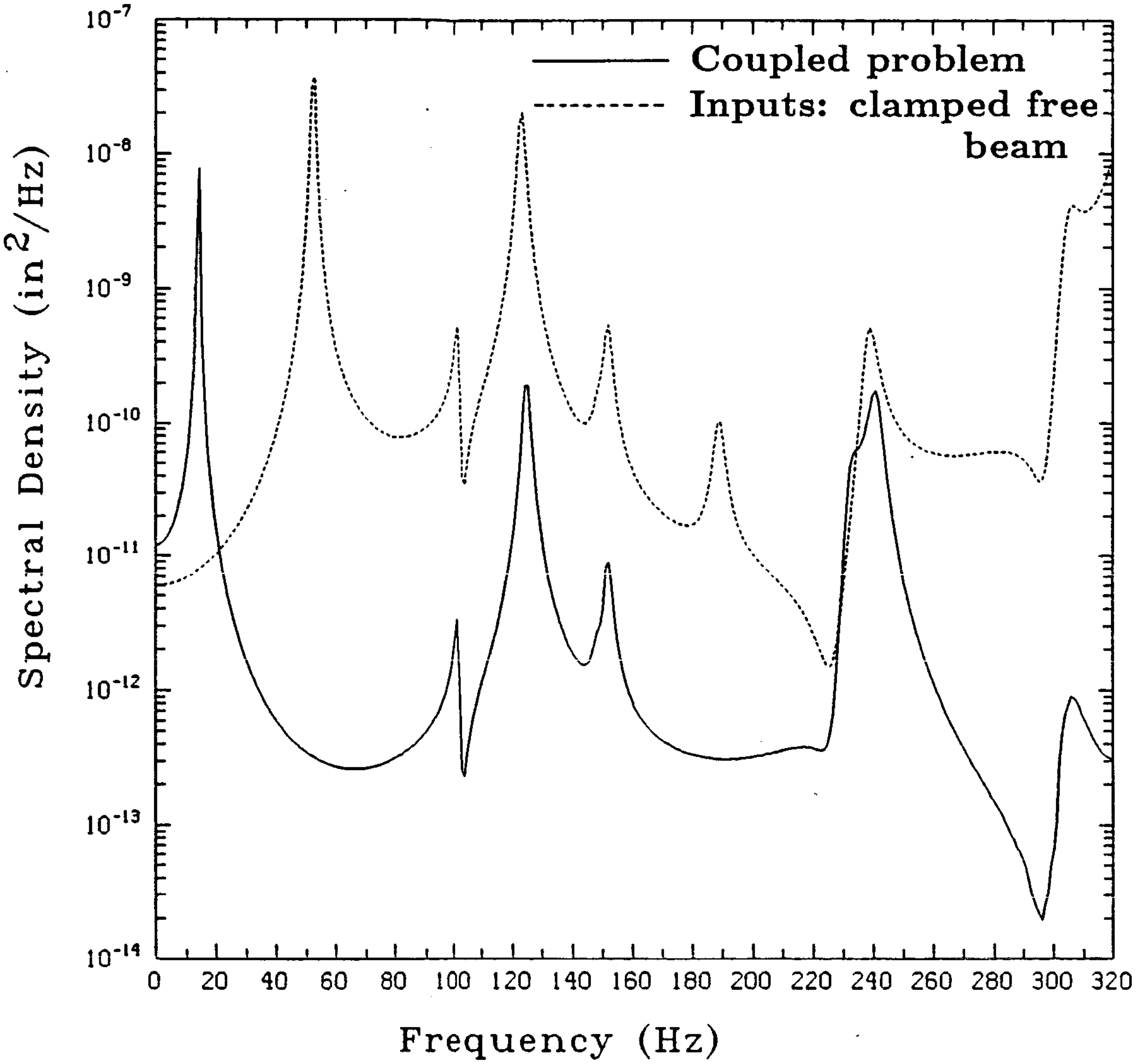

Fig. 53 *Deflection response spectral densities for a coupled skin-stringer - beam and for a calculated bending moment input.*

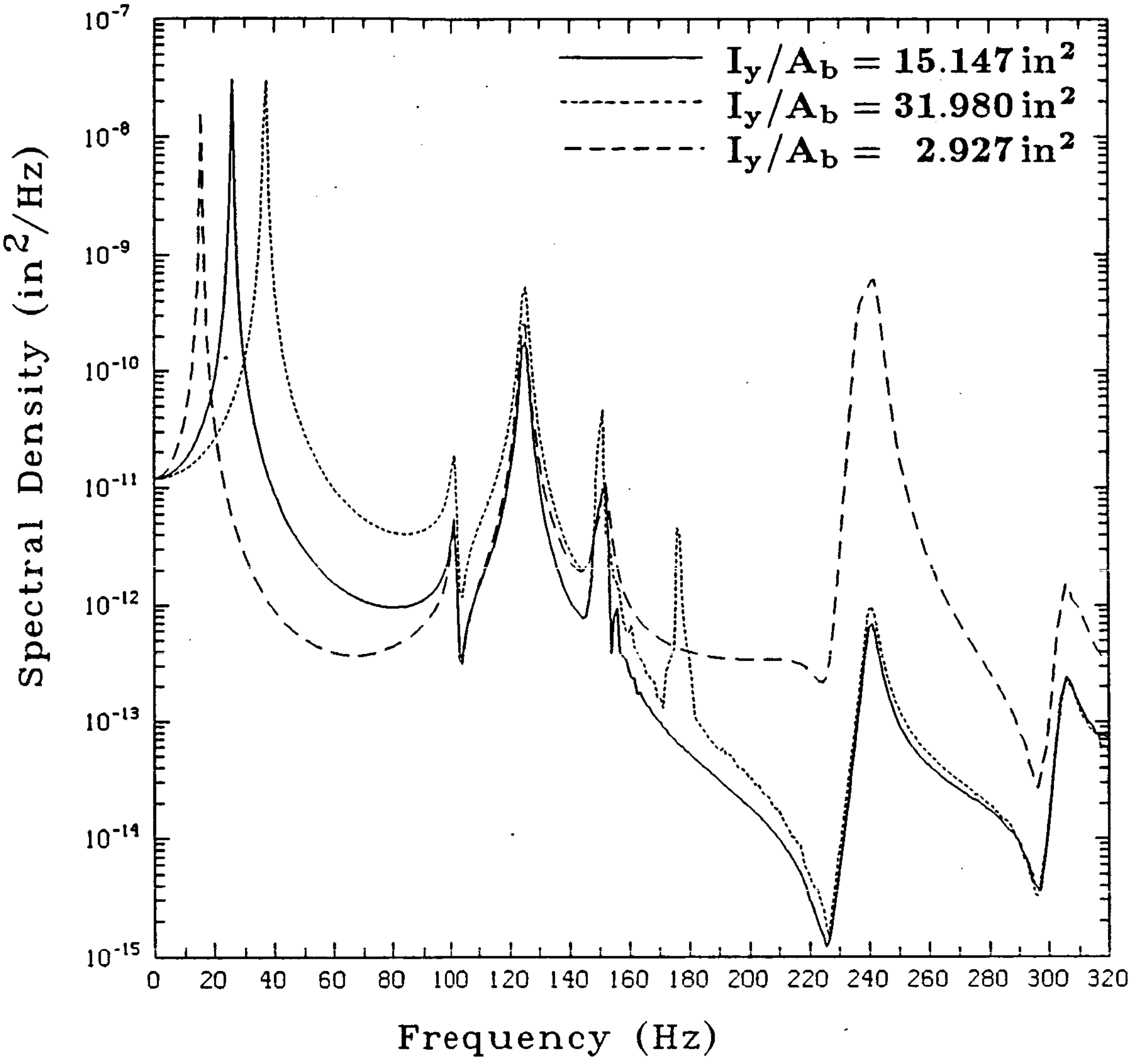

Fig. 54 *Deflection response spectral densities for different geometric characteristics of the cantilever box beam.*

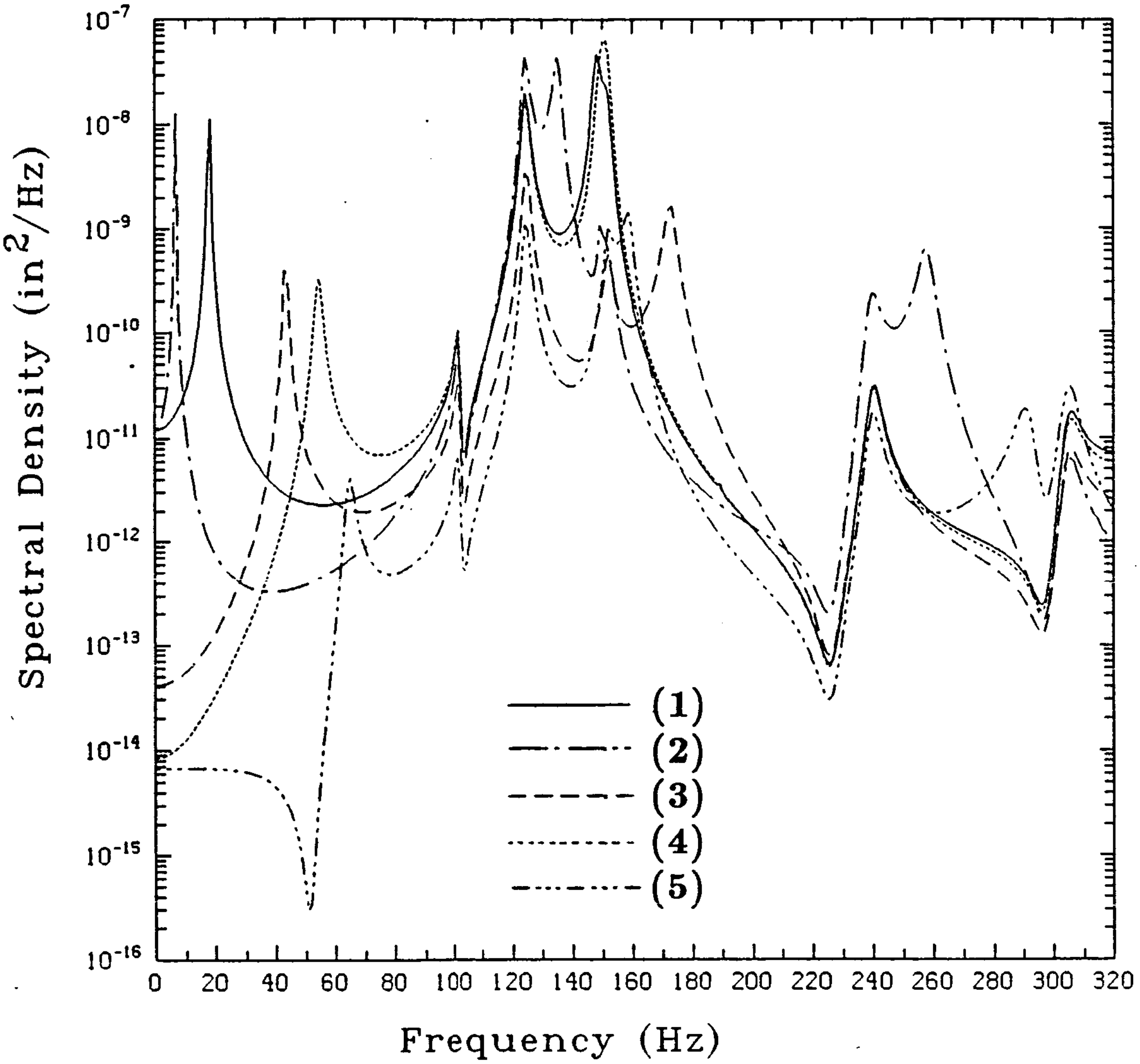

Fig. 55 *Deflection response spectral densities for the system shown in fig.* 8 *where*

- *(1)* $m_1 = k_{T1} = k_{R1} = 0$;
- *(2)* $m_1 \neq 0$, $k_{T1} = k_{R1} = 0$;
- *(3)* $k_{R1} \neq 0$, $m_1 = k_{T1} = 0$;
- *(4)* $k_{T1} \neq 0$, $m_1 = k_{R1} = 0$;
- *(5)* $m_1 \neq 0$, $k_{T1} \neq 0$, $k_{R1} \neq 0$.

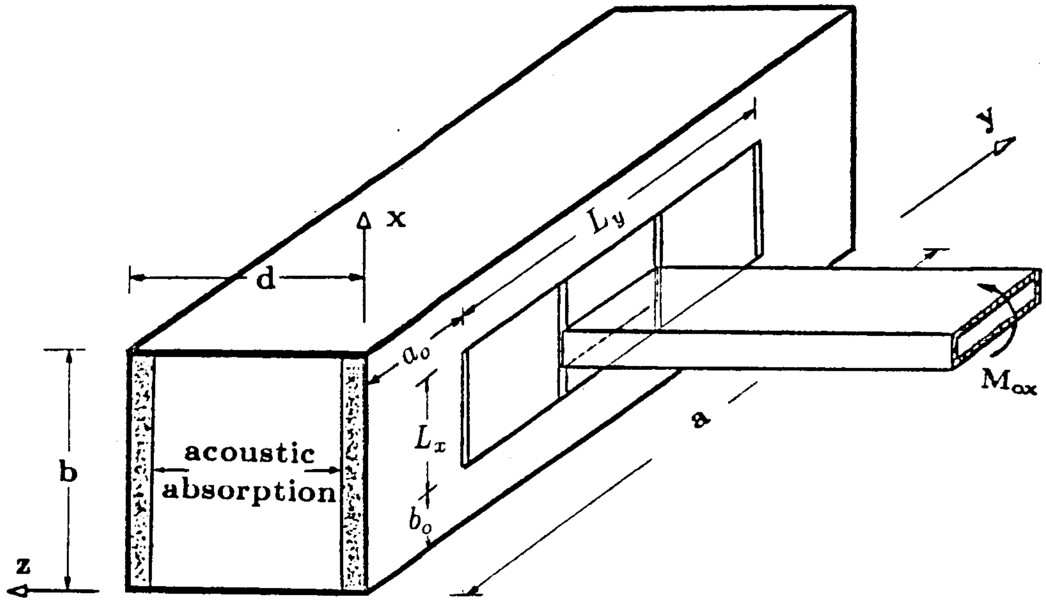

Fig. 56 *Geometry of an acoustic enclosure and a cantilever box beam.*

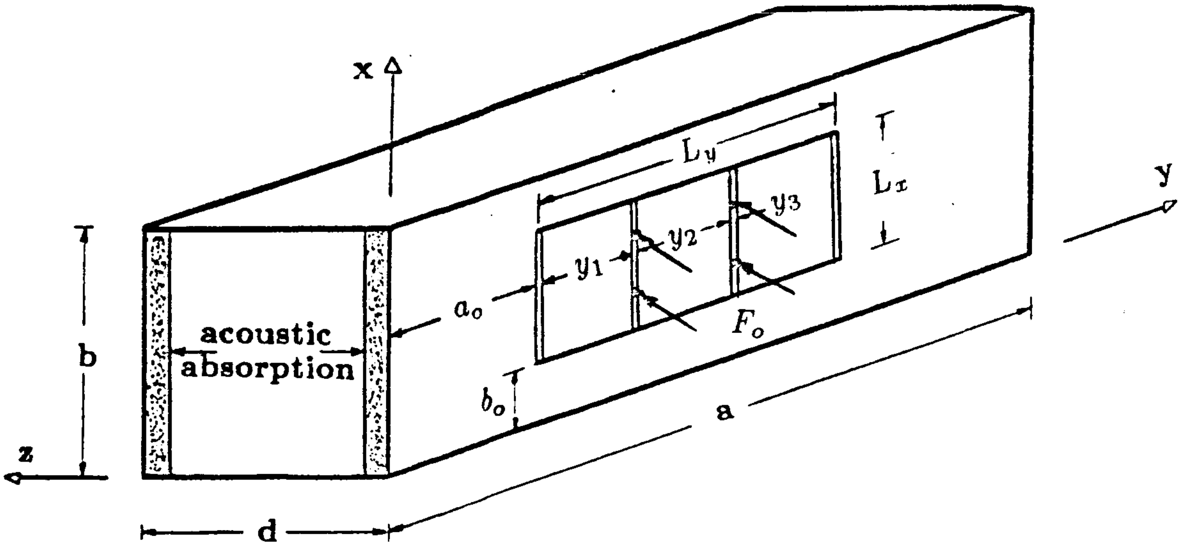

Fig. 57 *Geometry of an acoustic enclosure subject to random point loads.*

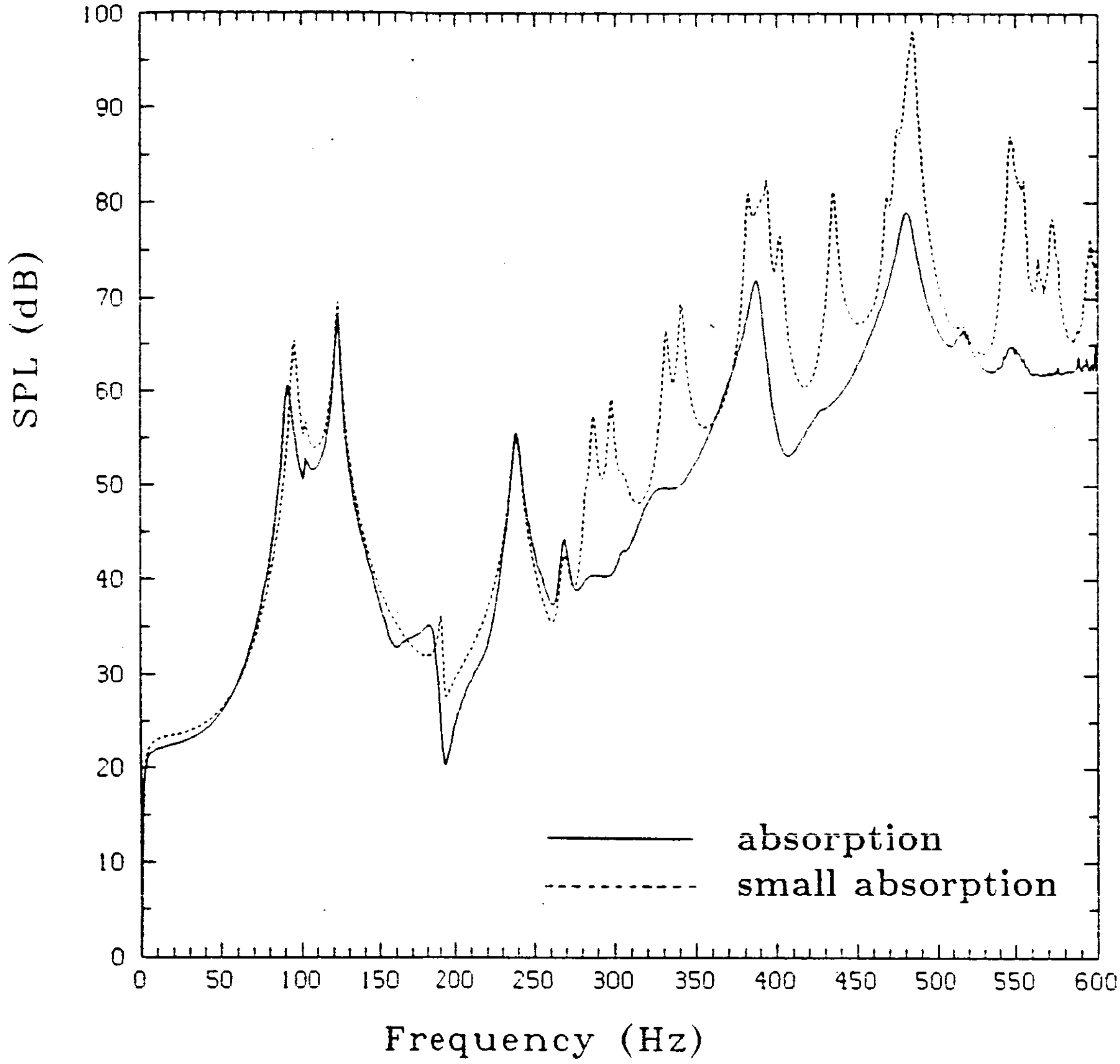

Fig. 58 *Sound pressure levels in the interior for different acoustic absorption characteristics.*

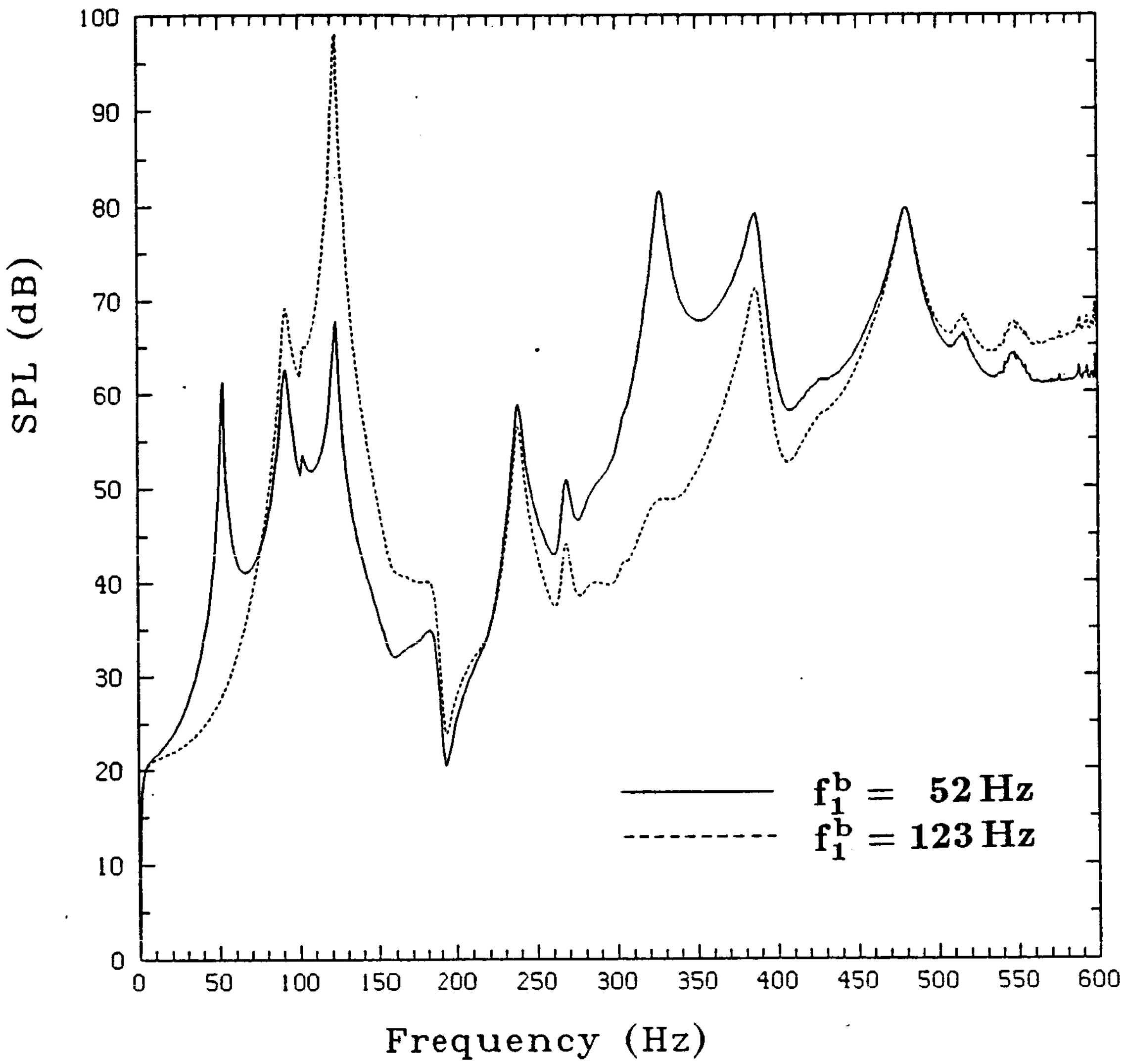

Fig. 59 *Sound pressure levels in the interior for different clamped-free beam dynamic characteristics.*

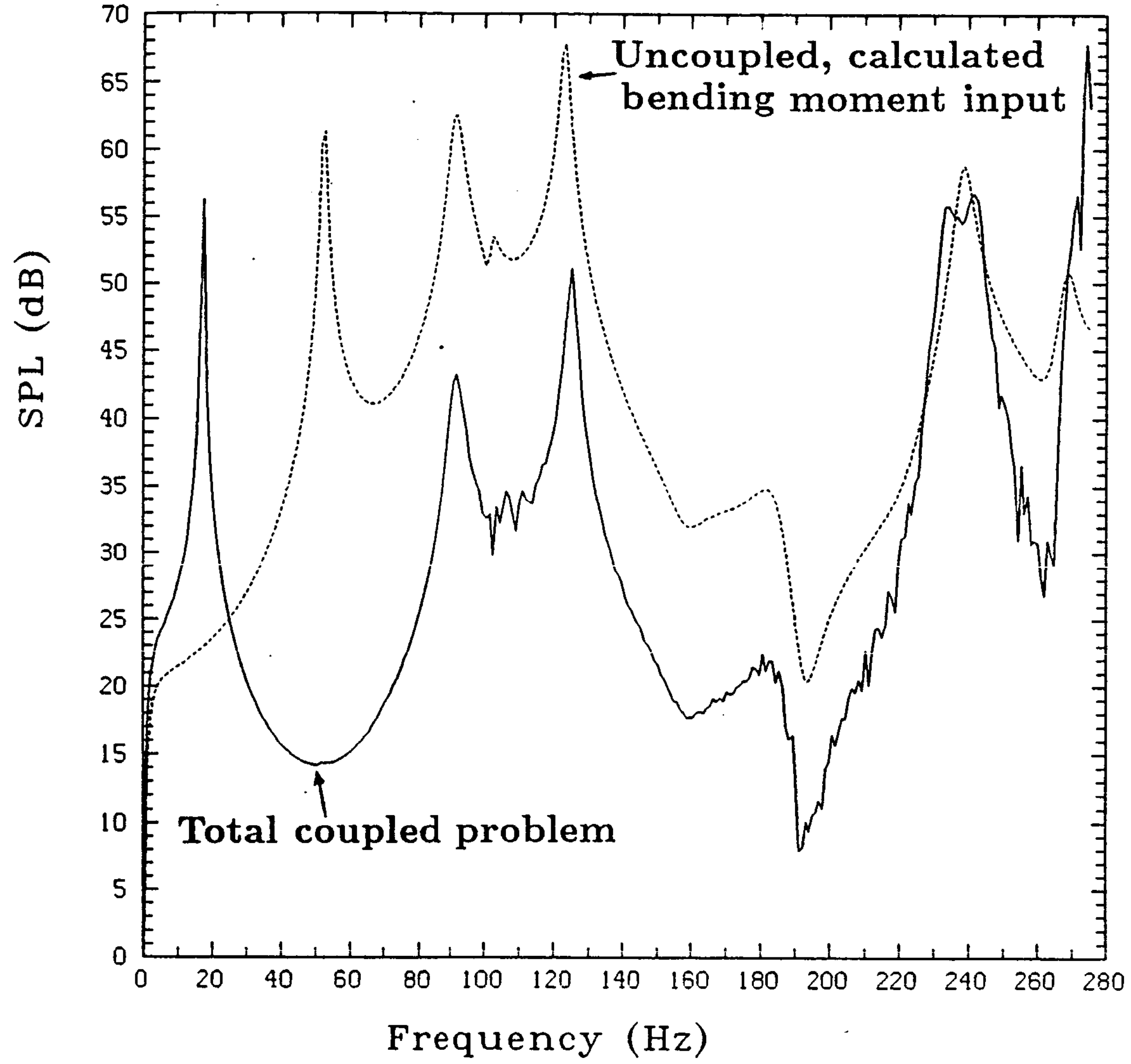

Fig. 60 *Sound pressure levels in the interior for coupled and uncoupled conditions between the substructure and the noise transmitting stiffened sidewall.*

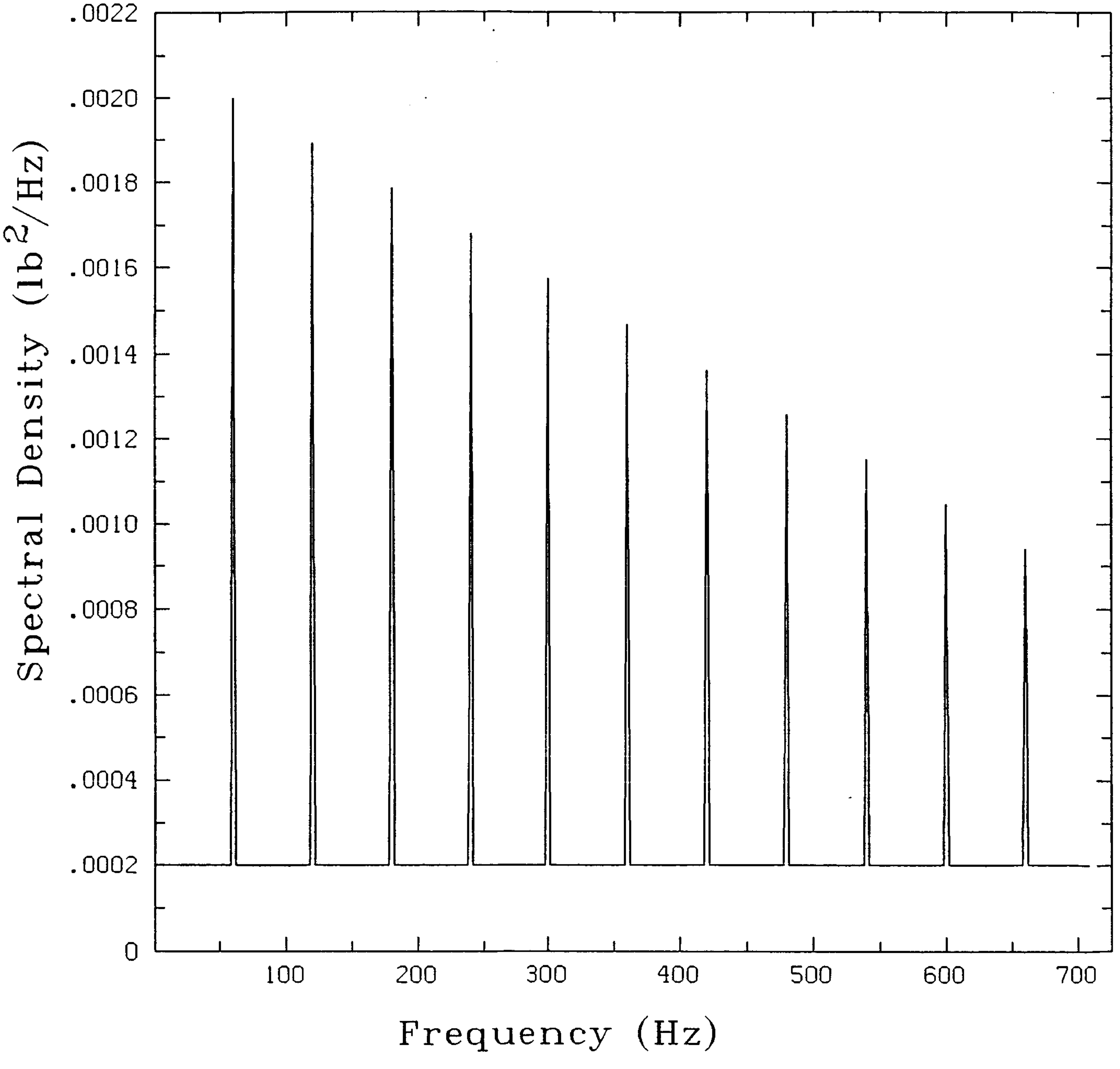

Fig. 61 Spectral density of input point forces

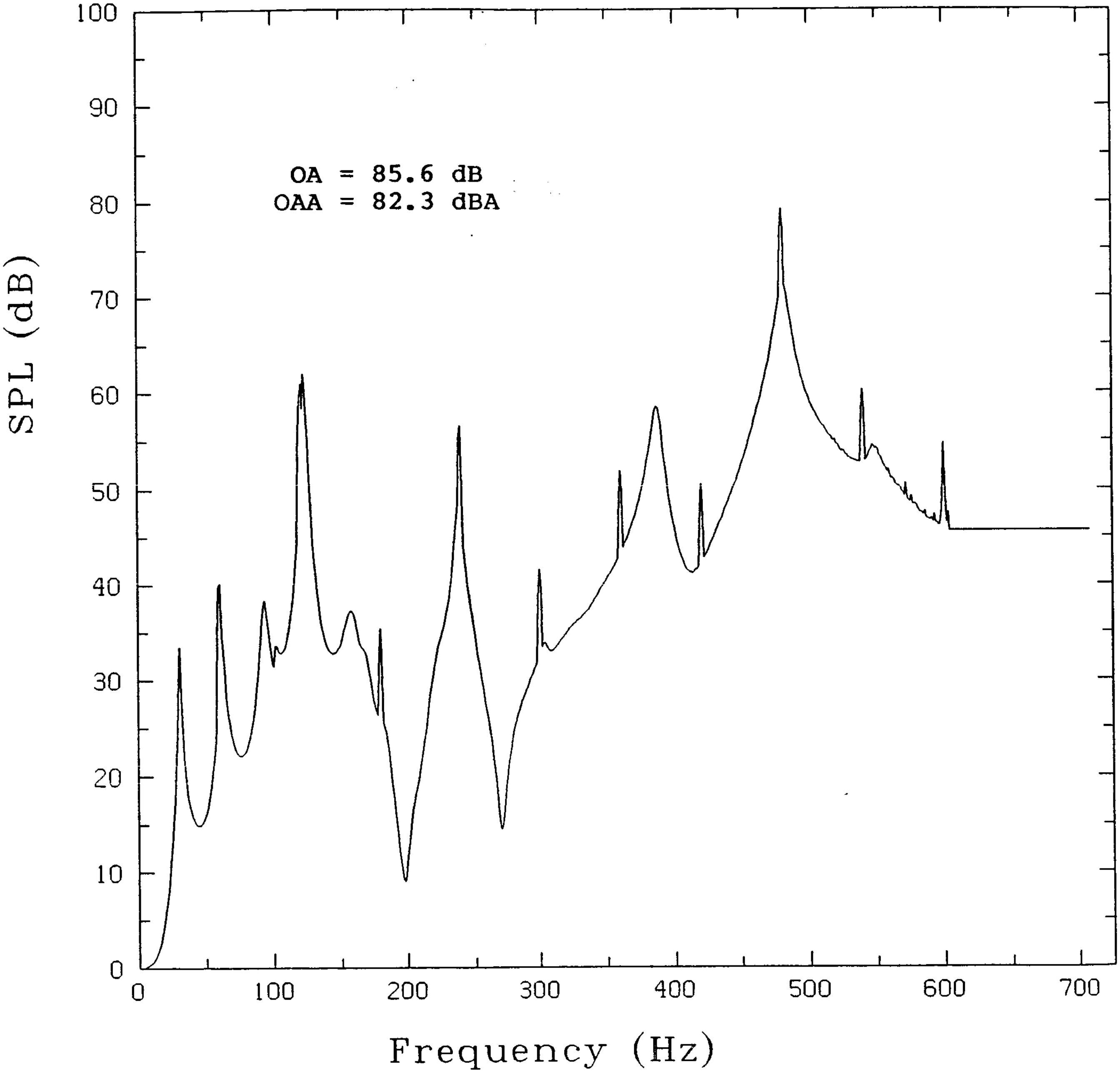

Fig. 62 Sound pressure levels for vibrating panel located at z = 0, x = 32 in., y = 198 in.

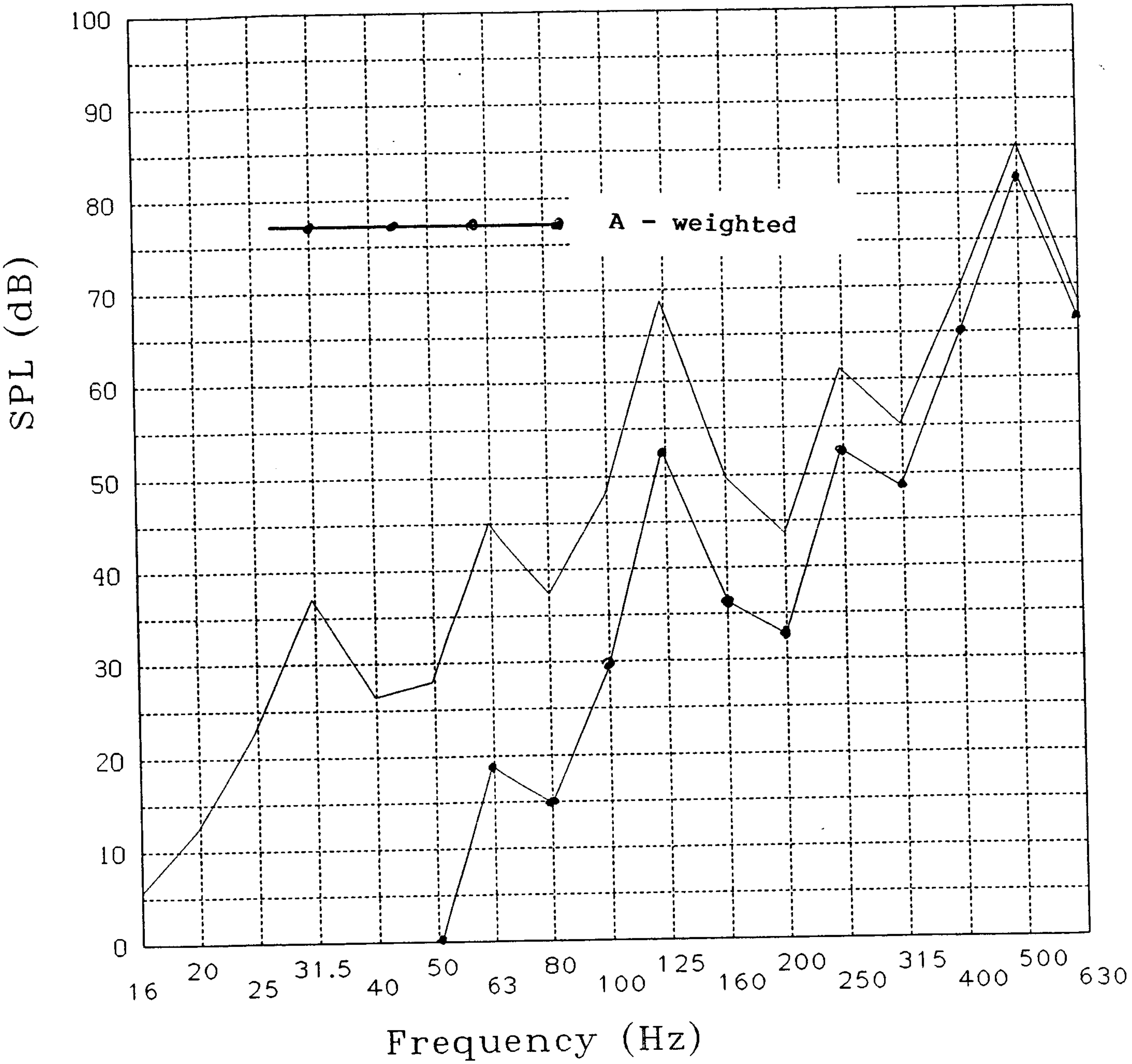

Fig. 63 One-third octave sound pressure levels for a panel located at z = 0, x = 32 in., y = 198 in.

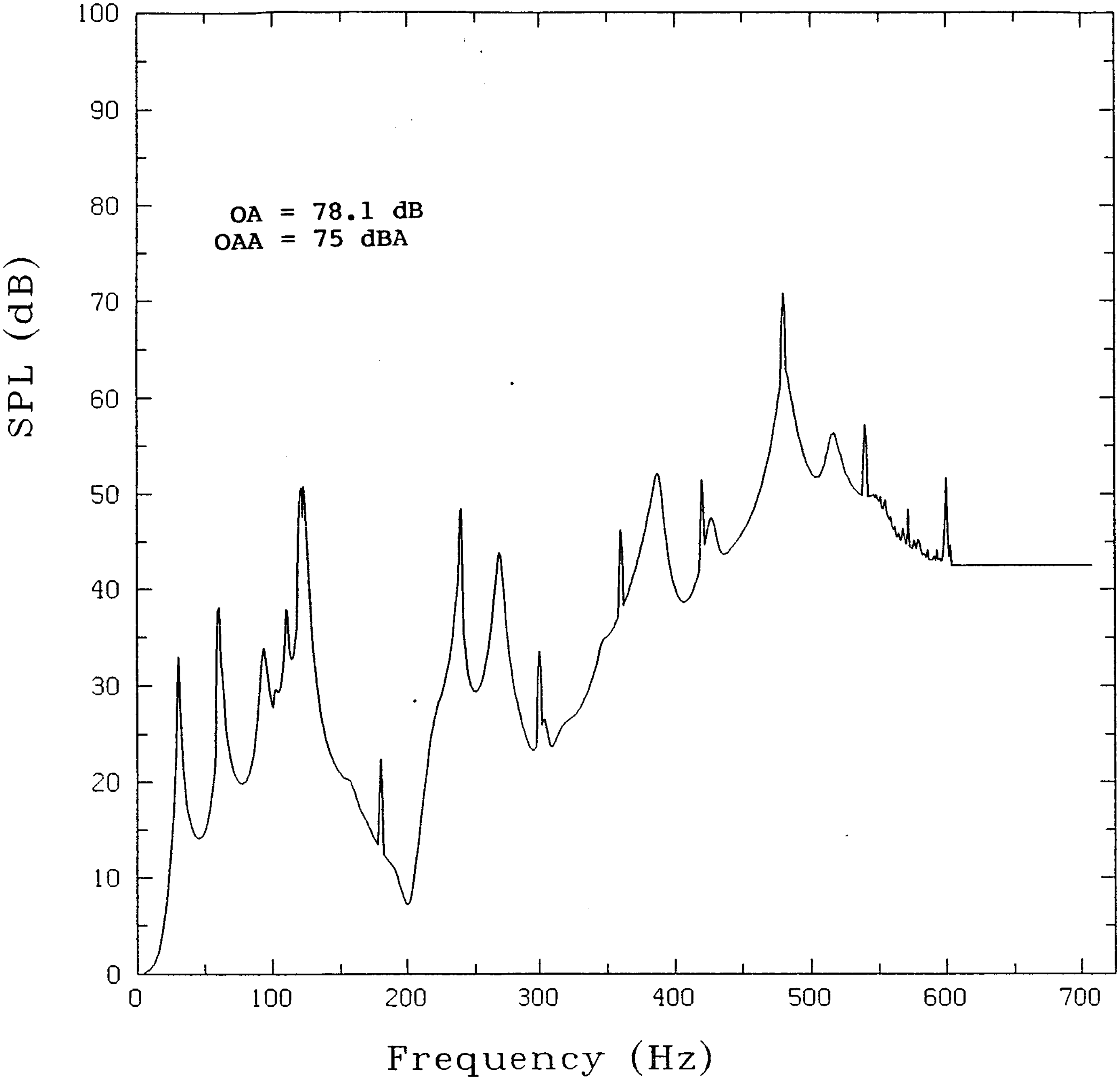

Fig. 64 Sound pressure levels for vibrating panel located at z = 0, x = 10 in., y = 10 in.

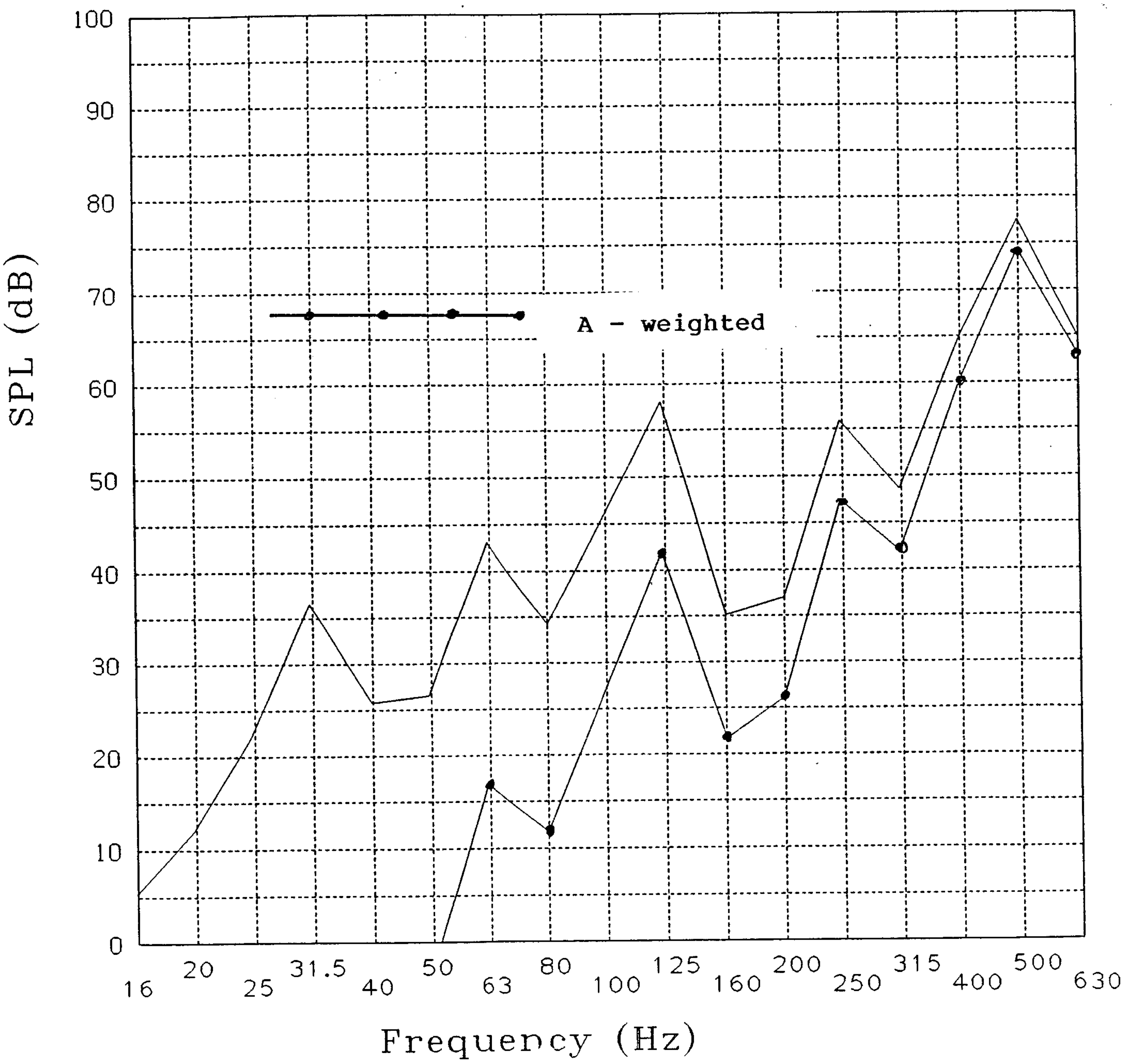

Fig. 65 One-third octave sound pressure levels for a panel located at z = 0, x = 10 in., y = 10 in.

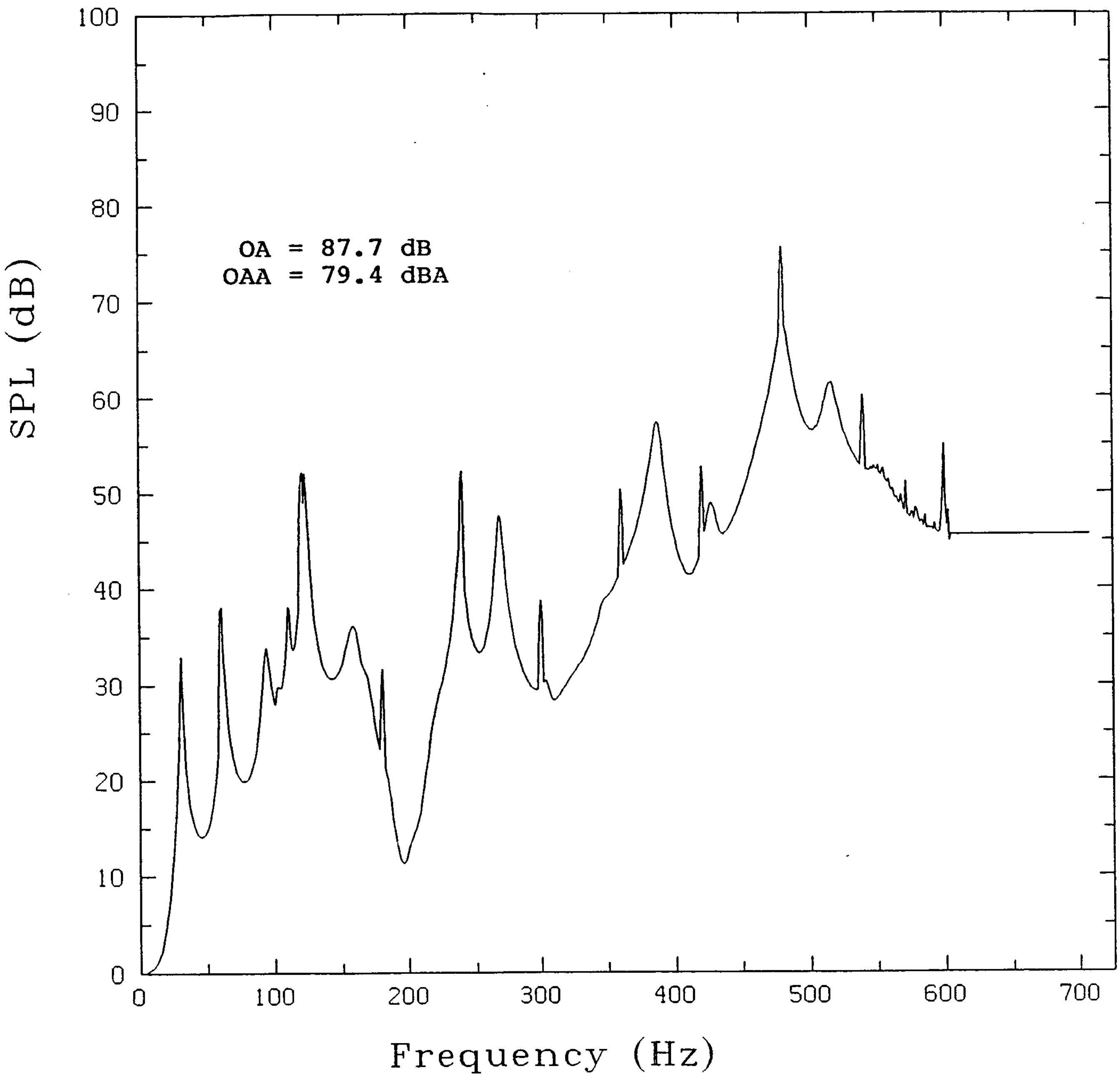

Fig. 66 Sound pressure levels for vibrating panel located at z = 0, x = 32 in., y = 10 in.

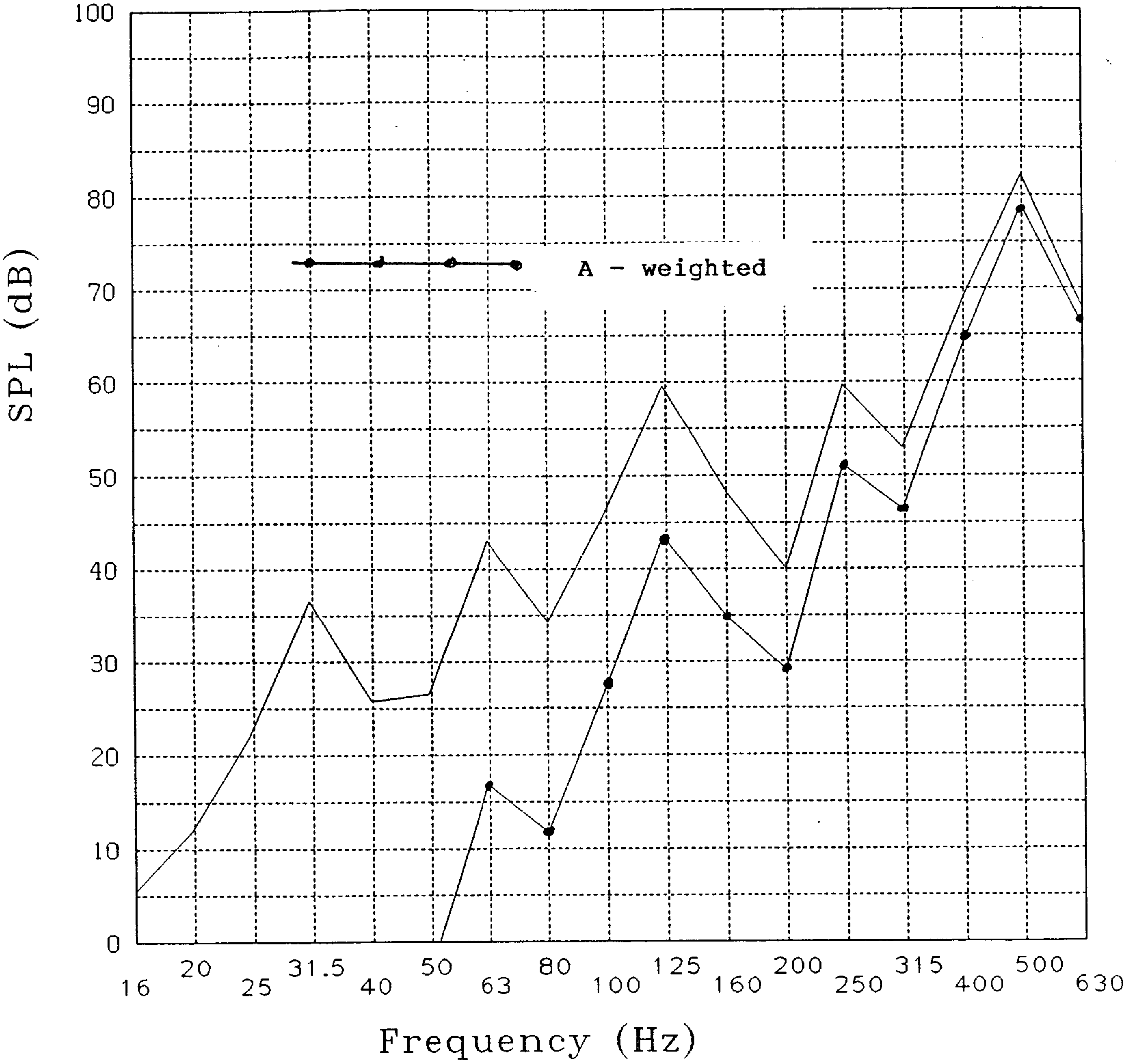

Fig. 67 One-third octave sound pressure levels for a panel located at z = 0, x = 32 in., y = 10 in.

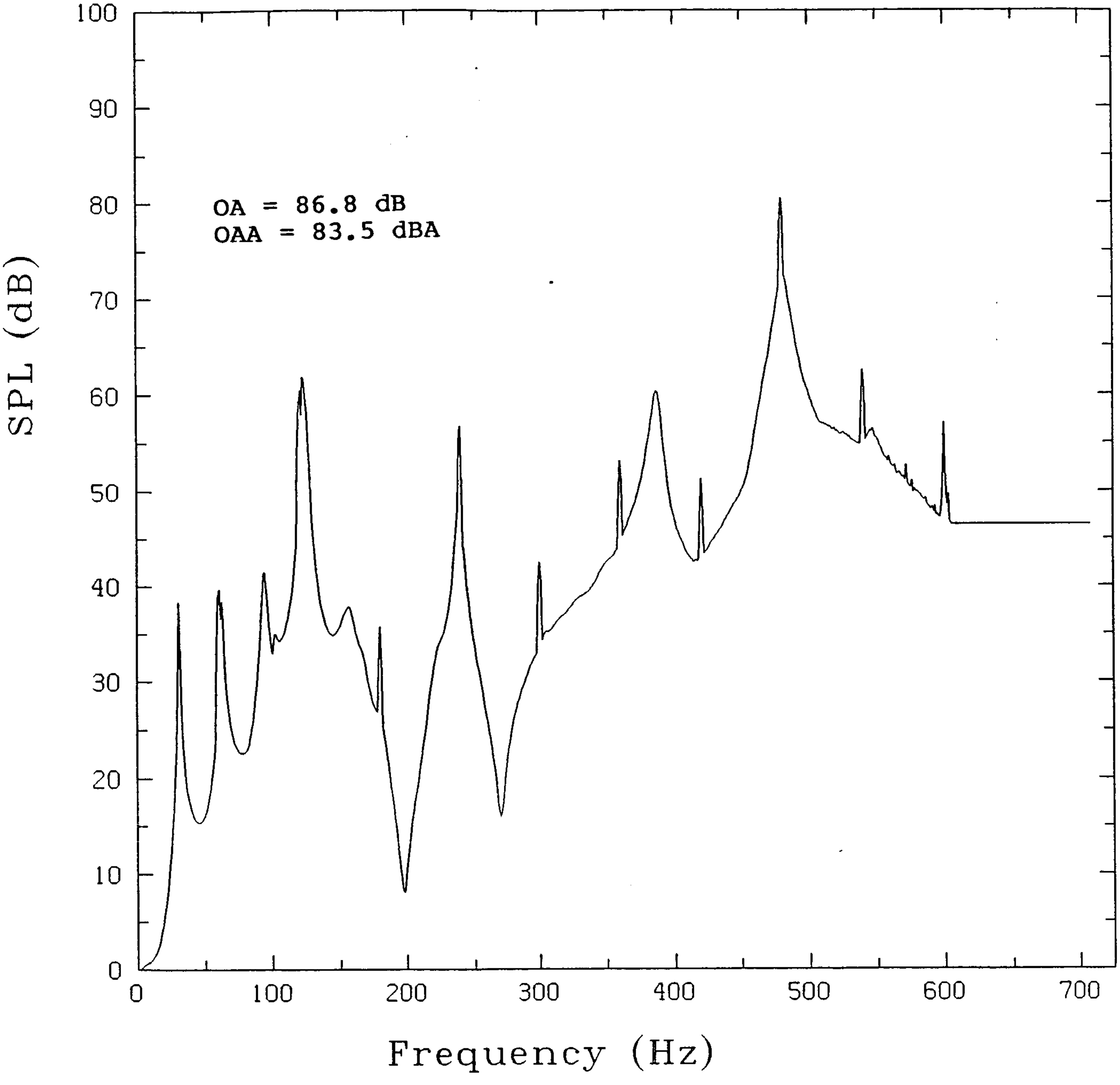

Fig. 68 Sound pressure levels for vibrating panel located at z = 20 in., x = 84 in., y = 198 in.

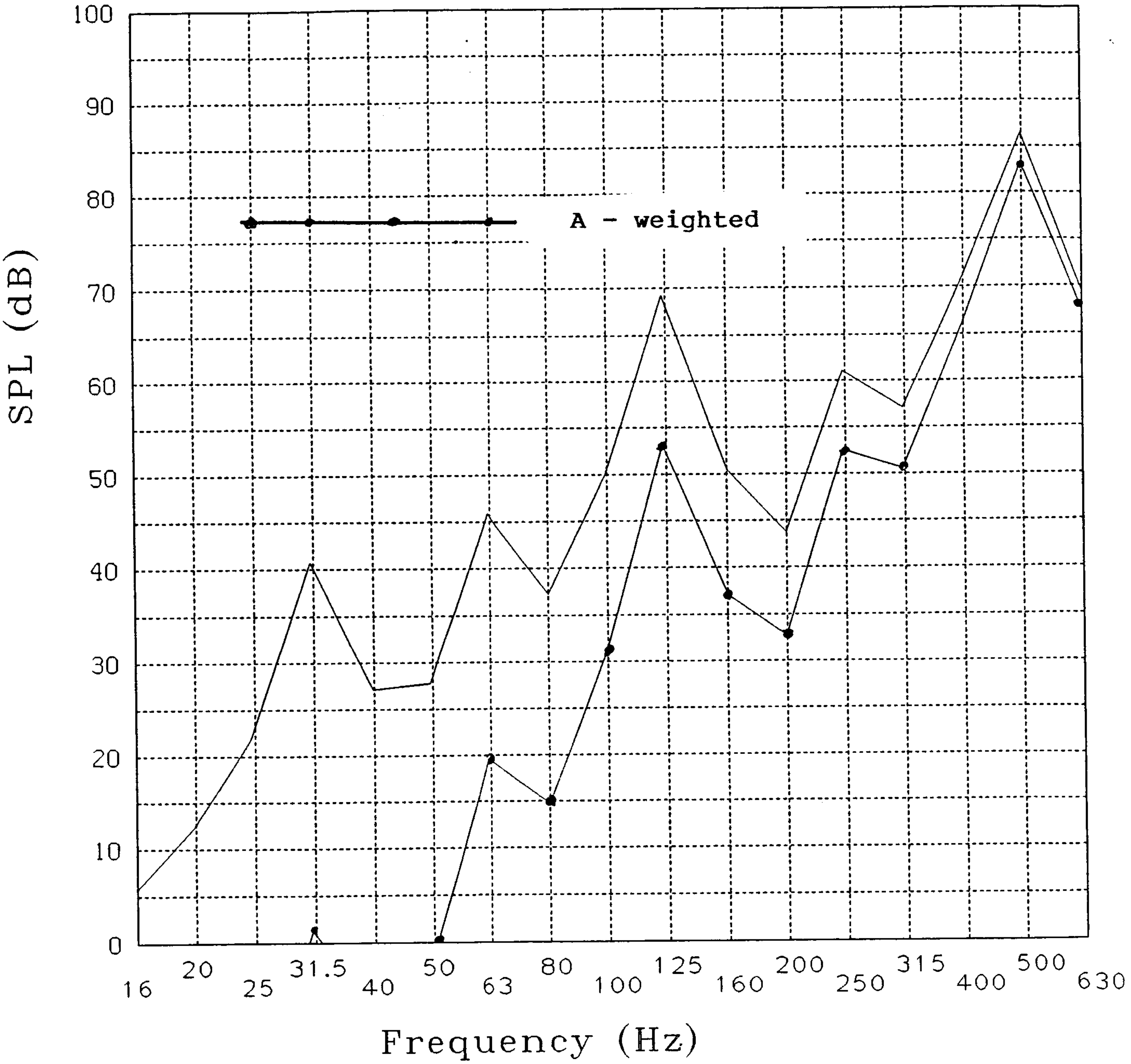

Fig. 69 One-third octave sound pressure levels for a panel located at z = 20 in., x = 84 in., y = 198 in.

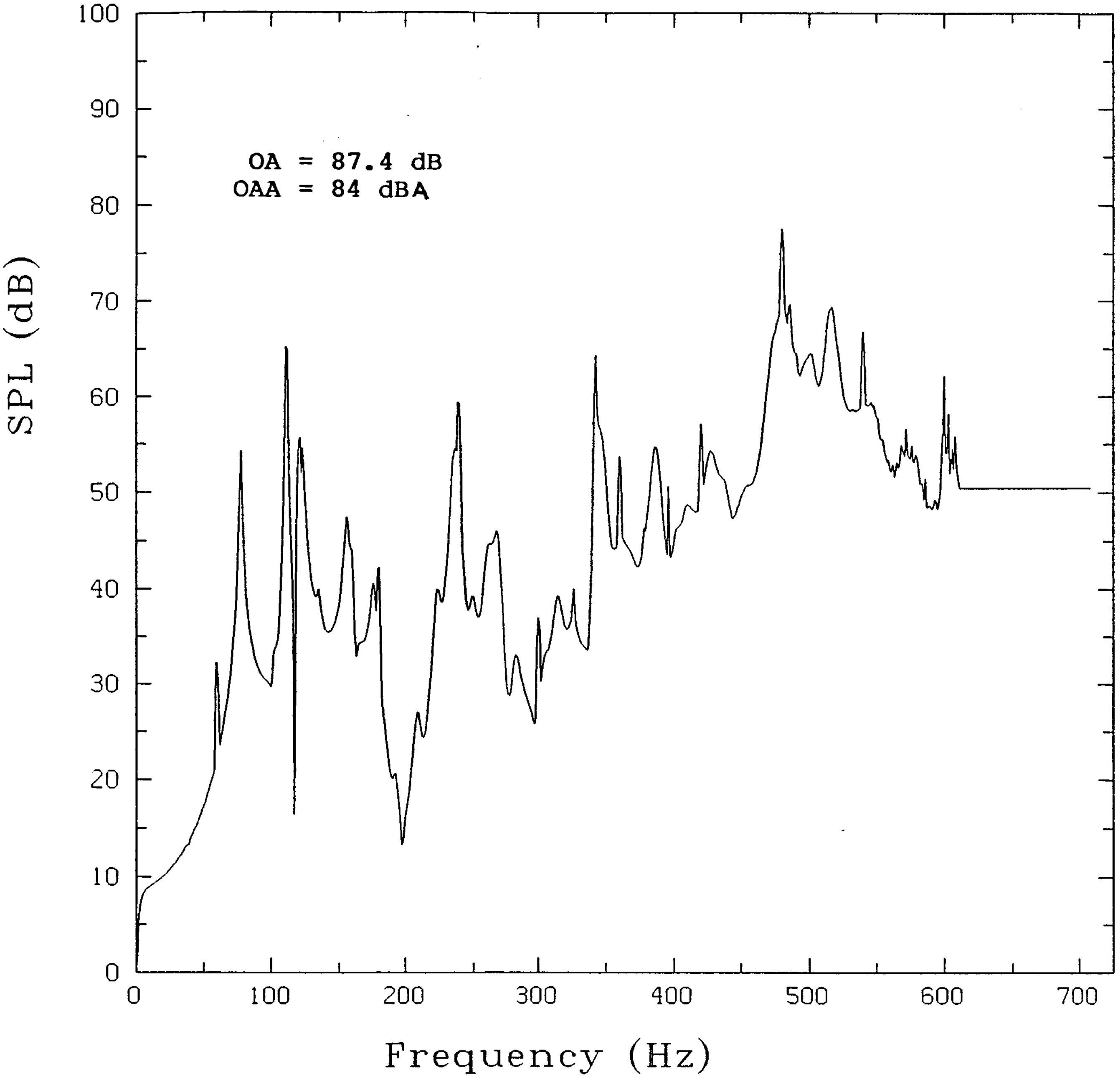

Fig. 70 Sound pressure levels for a vibrating panel located at z = 42.3 in., x = 32 in., y = 0.0.

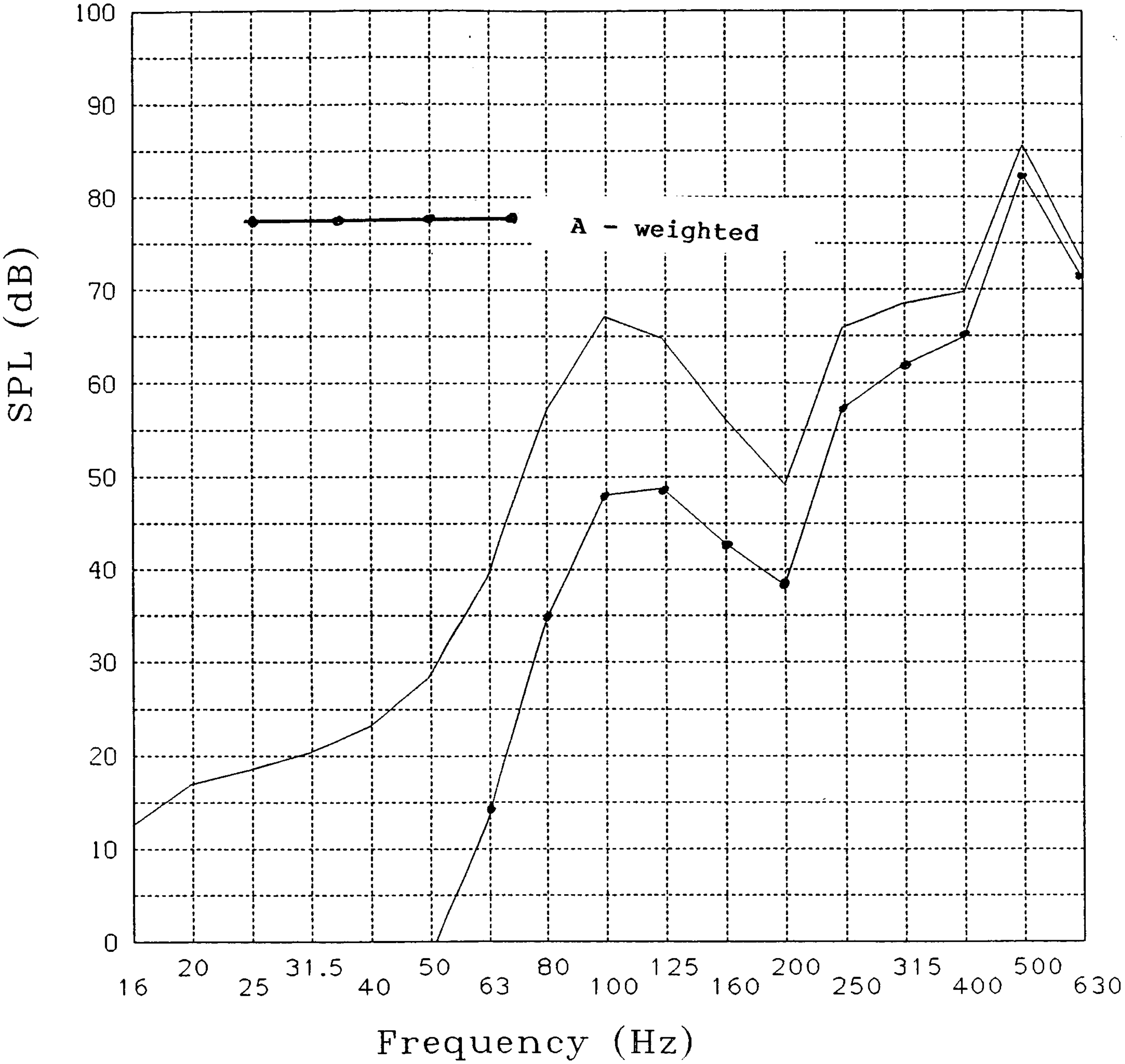

Fig. 71 One-third octave sound pressure levels for a panel located at z = 42.3 in., x = 32 in., y = 0.0 in.

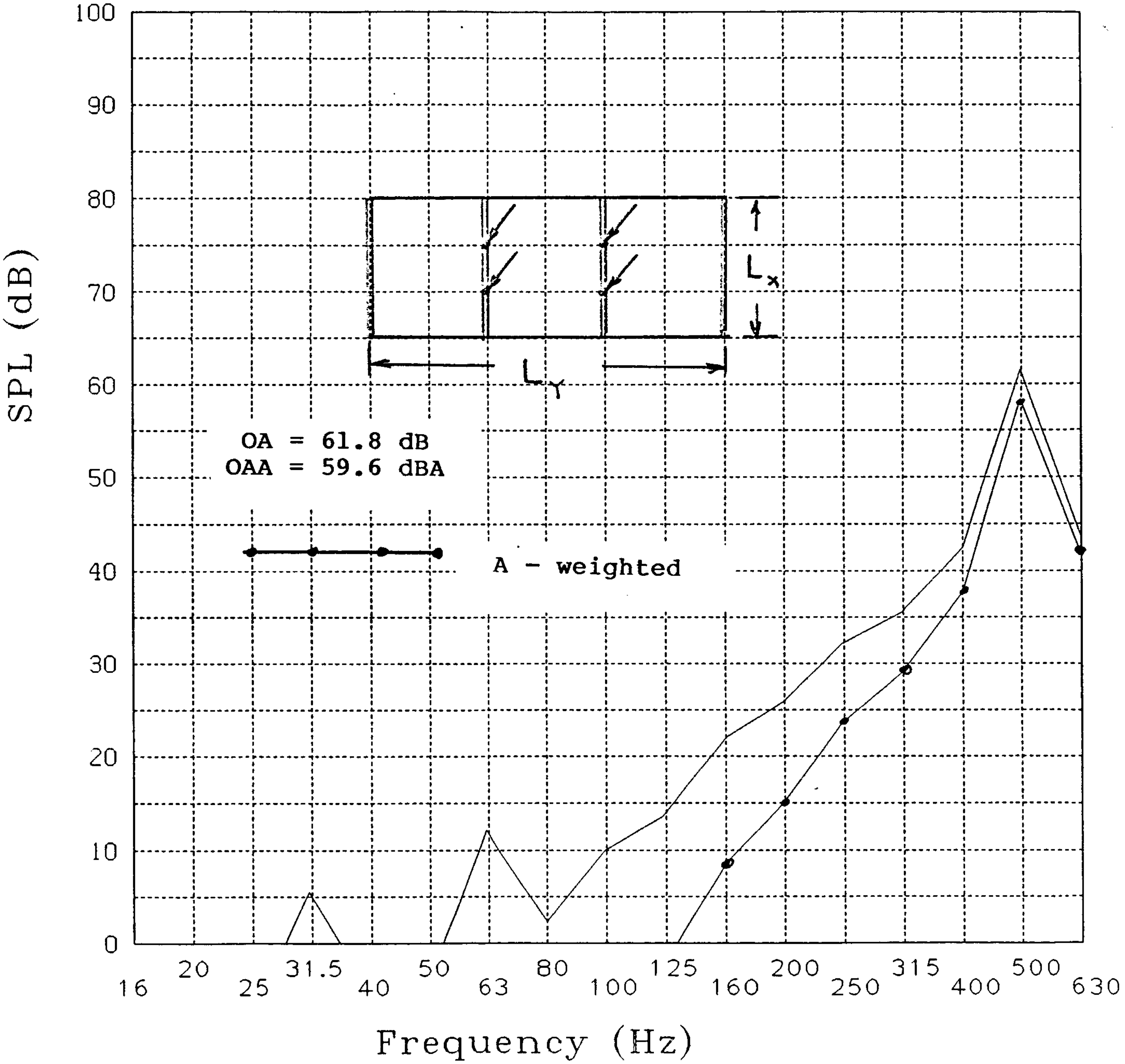

Fig. 72 One-third octave sound pressure levels for a panel with dimensions L_x = 10 in. and L_y = 12.3 in.

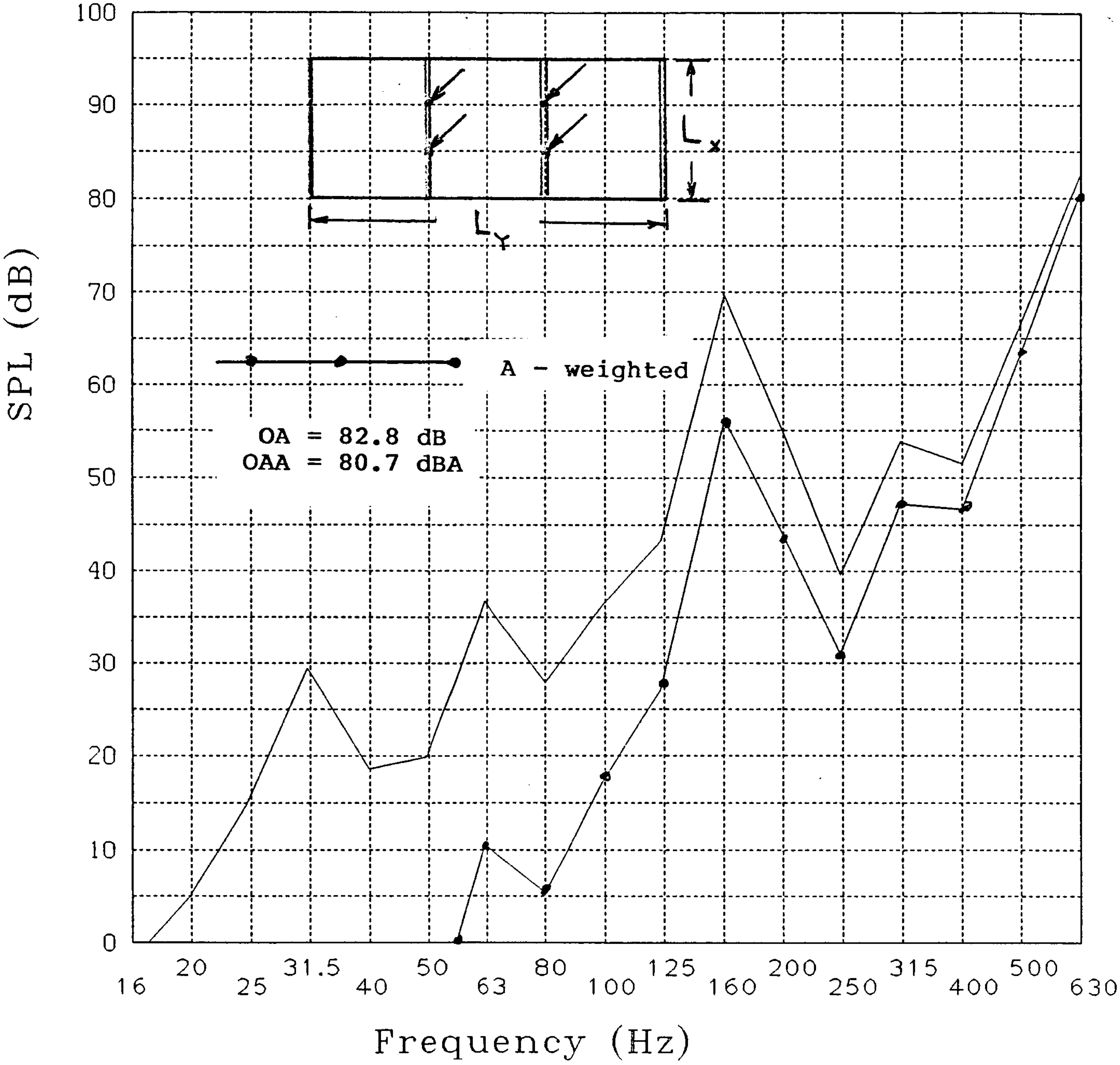

Fig. 73 One-third octave sound pressure levels for a panel with dimensions L_x = 17 in. and L_y = 21.6 in.

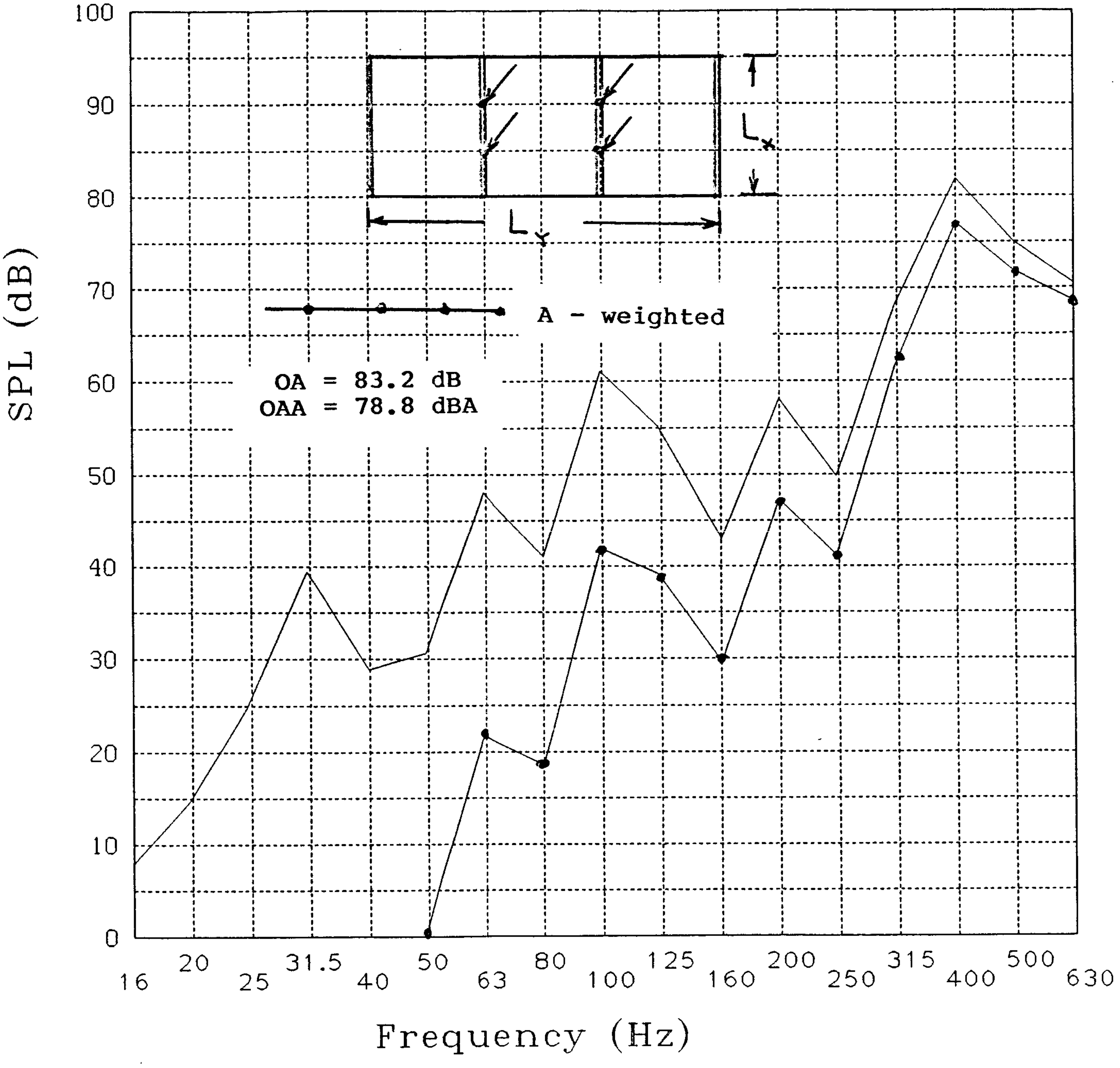

Fig. 74 One-third octave sound pressure levels for a panel with dimensions L_x = 21 in. and L_y = 26.1 in.

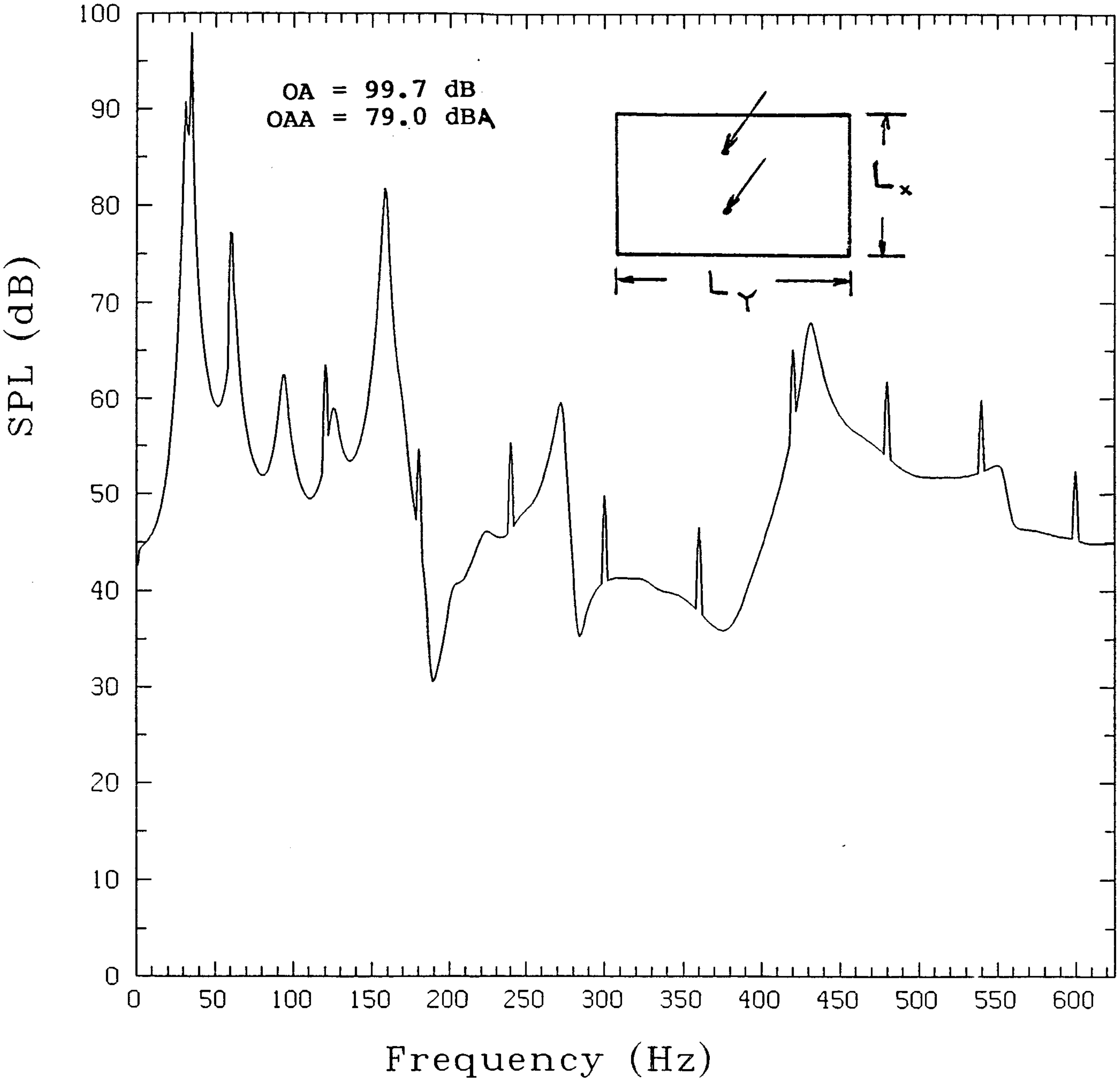

Fig. 75 Sound pressure levels for vibrating unstiffened panel with dimensions L_x = 20 in. and L_y = 16.4 in.

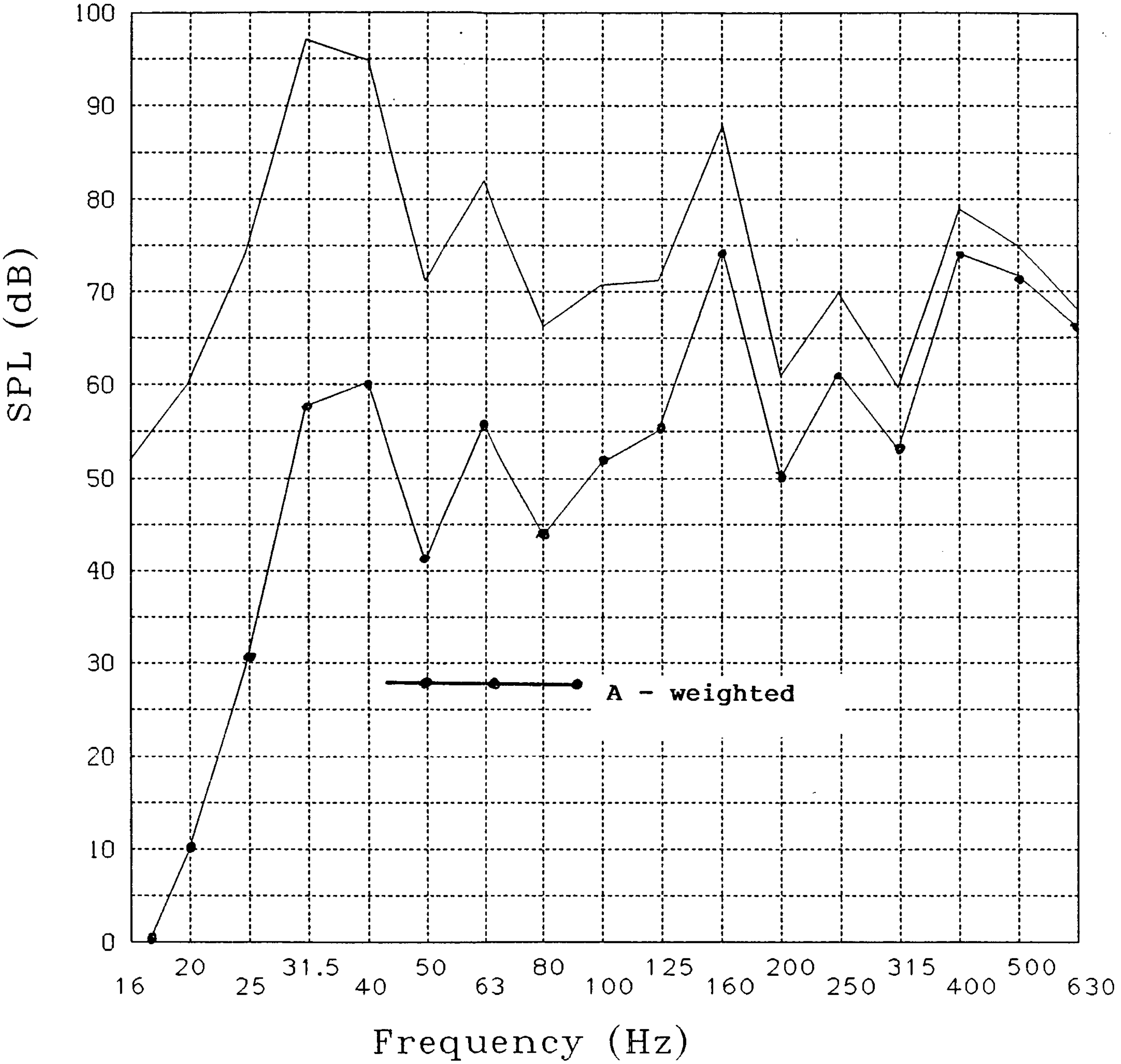

Fig. 76 One-third octave sound pressure levels for unstiffened panel

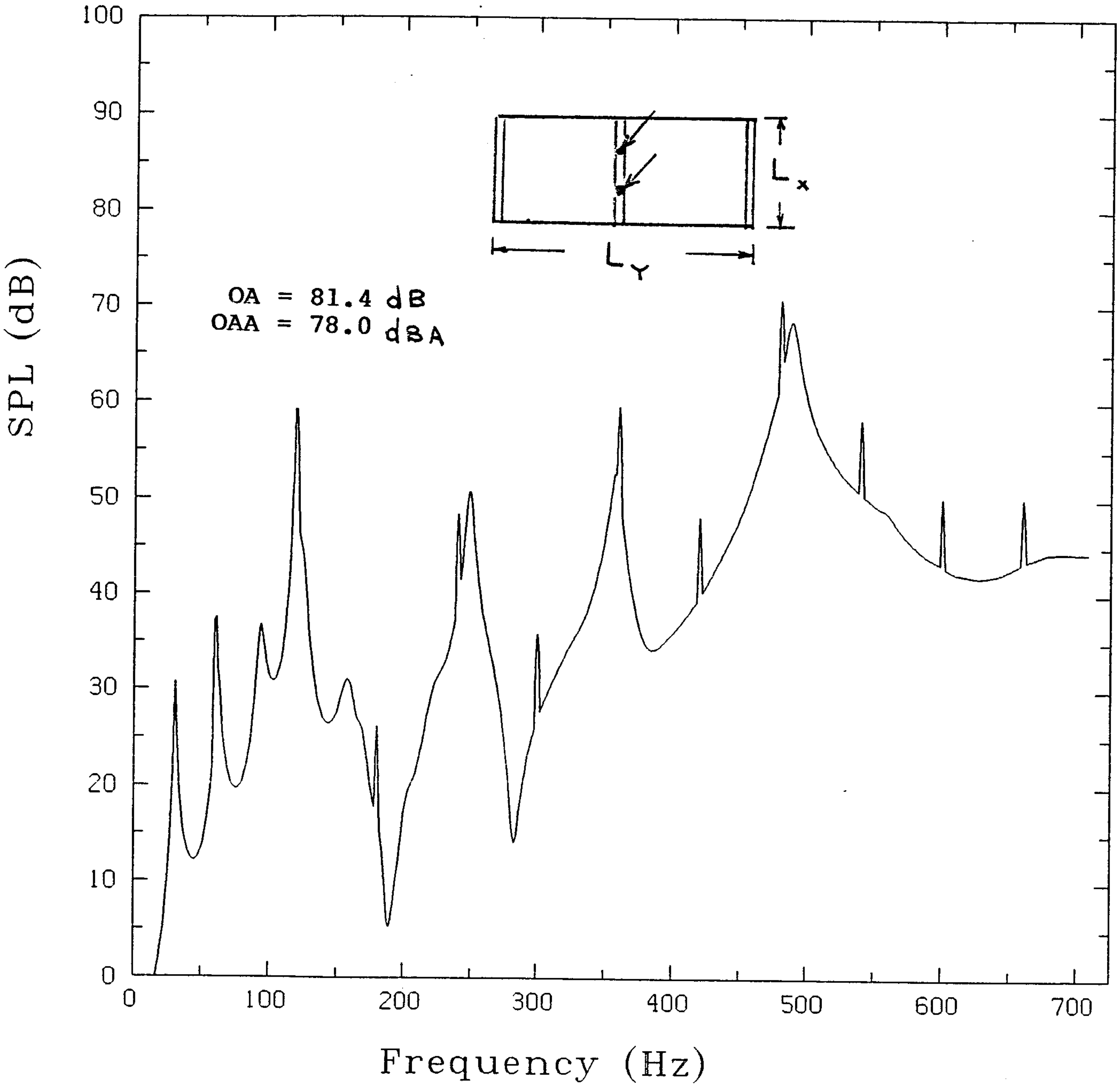

Fig. 77 Sound pressure levels for a stiffened panel with dimensions L_x = 20 in. and L_y = 16.4 in.

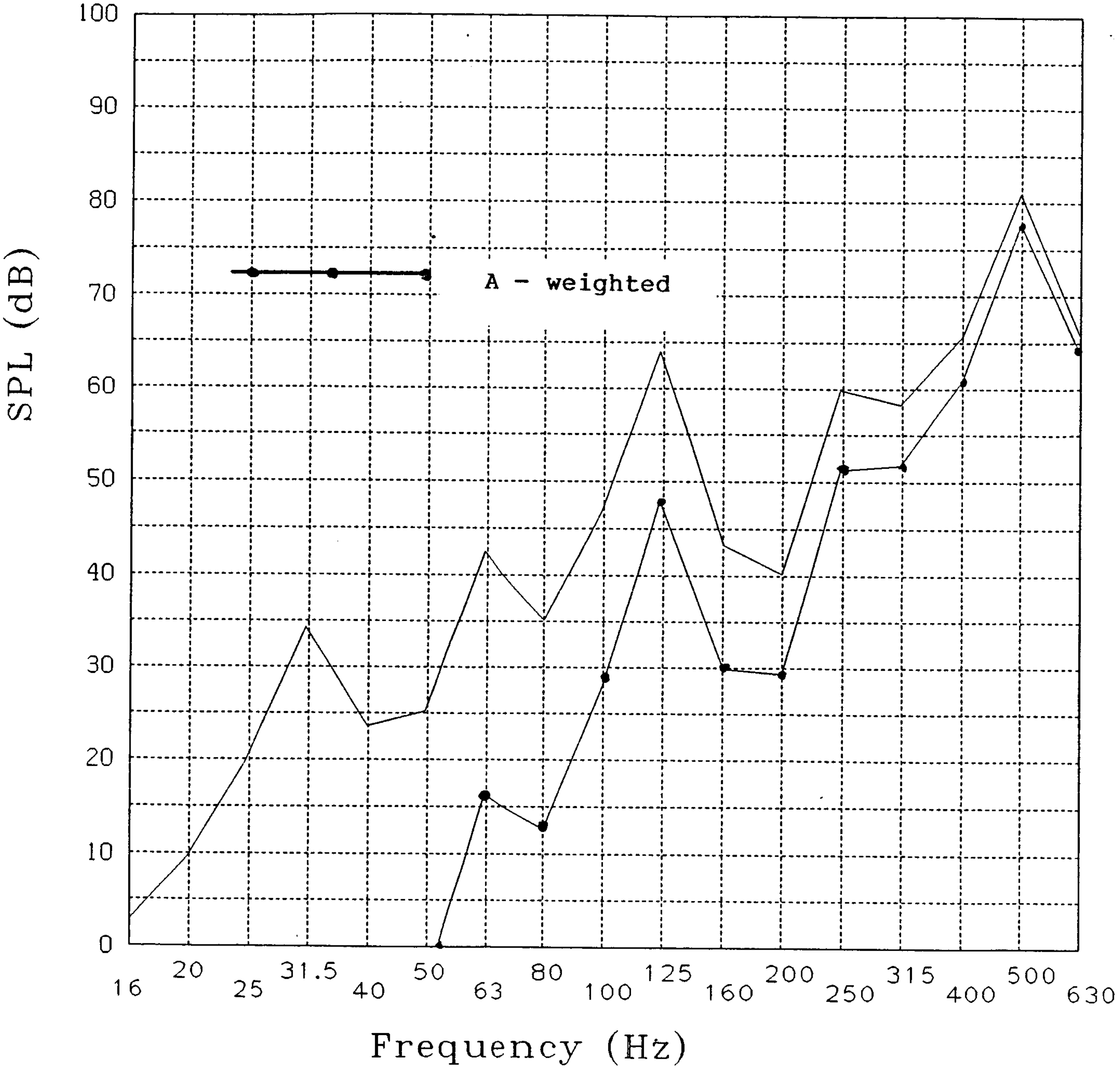

Fig. 78 One-third octave sound pressure levels for a stiffened panel